DYNAMIC BEHAVIOUR OF "HYBRID COMPOSITE SHAFT ROTOR-BEARING SYSTEM" OF AN AERO GAS TURBINE ENGINE

Thesis

Submitted in partial fulfillment of the requirements for the degree of

DOCTOR OF PHILOSOPHY

By

THIMOTHY HAROLD GONSALVES

DEPARTMENT OF MECHANICAL ENGINEERING

NATIONAL INSTITUTE OF TECHNOLOGY KARNATAKA

SURATHKAL, MANGALURU– 575025

December, 2020

Dedicated

to

My Family

DECLARATION

I hereby declare that the Research Thesis entitled **"DYNAMIC BEHAVIOUR OF "HYBRID COMPOSITE SHAFT ROTOR-BEARING SYSTEM" OF AN AERO GAS TURBINE ENGINE"** which is being submitted to the National Institute of Technology Karnataka, Surathkal in partial fulfilment of the requirements for the award of the Degree of Doctor of Philosophy in Mechanical Engineering is a bonafide report of the research work carried out by me. The material contained in this Research Thesis has not been submitted to any other Universities or Institutes for the award of any degree.

Register Number   : **145076ME14P04**

Name of the Research Scholar   : **THIMOTHY HAROLD GONSALVES**

Signature of the Research Scholar :

Department of Mechanical Engineering

Place: NITK-Surathkal

Date:

CERTIFICATE

This is to certify that the Research Thesis entitled **"DYNAMIC BEHAVIOUR OF "HYBRID COMPOSITE SHAFT ROTOR-BEARING SYSTEM" OF AN AERO GAS TURBINE ENGINE"** submitted by **Mr. THIMOTHY HAROLD GONSALVES (Register Number: 145076ME14P04)** as the record of the research work carried out by him, *is accepted as the Research Thesis submission* in partial fulfilment of the requirements for the award of the Degree of **Doctor of Philosophy.**

Research   Guide (s)

Dr. G.C. Mohan Kumar

Professor (HAG)

Department of Mechanical Engg.,

NITK, Surathkal

Dr. M.R. Ramesh

Associate Professor

Department of Mechanical Engg.,

NITK, Surathkal

Chairman-DRPC

Date:

ACKNOWLEDGEMENTS

ABSTRACT

In the present study, the hybrid composite shaft's dynamic behaviour is evaluated in detail with the primary intention of using it in the high-speed rotor-bearing system of an aero gas turbine engine. In this research work, the top-down research approach is adopted wherein the most appropriate rotor-bearing system for the composite shaft application was first assessed. A preliminary rotor dynamic study was carried out on the three prospective rotor-bearing systems to verify the possibility of using the composite shaft. The preliminary rotor dynamic study indicated that the power turbine rotor-bearing system of a front driving turboshaft engine powering the rotorcraft as the most suitable application of composite shaft. To avoid the gas turbine engine's high temperatures, the composite shaft was proposed to be within the compressor section while the existing steel alloy was retained in the hot section. The hybrid composite shaft made of composite material sandwiched between the steel tubes was envisaged to avoid the direct exposure of composite material to the gas turbine's harsh environment and for the easier interface with the subsequent metallic assembly. A parametric study was carried out to select the right combination of material, thickness, and stacking sequences of the composite laminate layers. The mechanical characterization was carried out to estimate the material strength using a universal testing machine. The damping estimation was carried out using the free vibration and dynamic mechanical analysis techniques. Based on the parametric study and characterization tests, the carbon-epoxy laminate of 10 layers with the stacking sequence of $[90, 45, -45, 0_6, 90]$ sandwiched by steel was found to be the best material configuration for the hybrid power turbine shaft. Finally, the rotor dynamic analysis of the power turbine shaft was carried out for a couple of variations in the thickness of steel tubes and length of the hybrid shaft to obtain the best configuration in comparison to the existing steel shaft. The results obtained in this work have successfully demonstrated the utility of the hybrid composite shaft in line with the objectives laid down for the thesis work.

Keywords: Campbell diagram; critical speed; hybrid composite shaft; internal damping; modal analysis.

TABLE OF CONTENTS

LIST OF TABLES

LIST OF FIGURES

NOMENCLATURE

ARALL®	Aramid Reinforced Aluminium Laminate
CARALL®	Carbon Reinforced Aluminium Laminate
GLARE®	Glass Reinforced Aluminium Laminate
AL	Aluminium
AMS	Aerospace Materials Specifications
ASTM	American Society for Testing and Materials
ADF	Anelastic Displacement Field
ATF	Augmenting Thermodynamic Field
B/E	Boron/Epoxy
BW	Backward Whirl
CFRP	Carbon Fiber Reinforced Plastic
CFRML	Carbon Fiber Reinforced Metal Laminate
C/E	Carbon/Epoxy
CBT	Classical Beam Theory
CS	Critical Speed
CUF	Carrera Unified Formulation
DMA	Dynamic Mechanical Analysis
DMTA	Dynamic Mechanical and Thermal Analysis
ED	External Damping
ECMBT	Equivalent Complex Modulus Beam Theory
EMBT	Equivalent Modulus Beam Theory
FEA	Finite Element Analysis
FEM	Finite Element Method

FDM	Functionally Graded Material
FPL	Forest Products Laboratories
FRF	Frequency Response Function
FW	Forward Whirl
FSDBT	First Order Shear Deformation Beam Theory
GDQ	Generalized Differential Quadrature
GGRBS	Gas Generator Rotor-Bearing System
GL/E	Glass/Epoxy
GR/E	Graphite/Epoxy
LBT	Layer wise Beam Theory
LD	Logarithmic Decrement
LF	Loss Factor
LM	Loss Modulus
LPRBS	Low Pressure Rotor-Bearing System
LVDT	Linear Variable Differential Transformer
MAC	Modal Assurance Factor
MEMBT	Modified Equivalent Modulus Beam Theory
NED	No External Damping
PTRBS	Power Turbine Rotor-Bearing System
RID	Rotating Internal Damping
SAC	Signature Assurance Criteria
SE	Strain Energy
SEM	Scanning Electron Microscope
SHBT	Simplified Homogenized Beam Theory

SM   Storage Modulus

ST   Steel

TBT   Timoshenko Beam Theory

TSDBT   Trigonometric Shear Deformation Beam Theory

TSDT   Third-order Shear Deformation Theory

SYMBOLS

E_i	Young's Modulus of composite material lamina along three orthogonal principal axes (i=1,2,3)	MPa
G_{ij}	Shear Modulus in direction 'j' and normal to direction 'i' on the shear plane of the composite material lamina (ij=12,23,31)	MPa
υ_{ij}	Poisson's ratio that corresponds to a contraction in direction 'j' when an extension is applied in direction 'i' (ij=12,23,31)	-
E_f	Young's Modulus of Fiber	MPa
E_m	Young's Modulus of Matrix	MPa
G_f	Shear Modulus of Fiber	MPa
G_m	Shear Modulus of Matrix	MPa
V_f	Volume Fraction of Fiber	%
V_m	Volume Fraction of Matrix	%
σ_i	Liner Stress along three principal axes of the lamina (i=1,2,3)	MPa
τ_{ij}	Shear stress in three orthogonal shear planes (ij=12,23,31)	MPa
ε_i	Linear along three principal axes of the lamina (i=1,2,3)	-
γ_{ij}	Shear strain in three orthogonal shear planes (i=1,2,3)	-
Q_{ij}	Stiffness tensor along 'i' due to force along 'j' (ij=11, 12, 22, 66)	MPa
S_{ij}	Compliance tensor (ij=11, 12, 22, 66)	MPa

E_x, E_y, E_z	Young's Modulus of the composite material lamina in three arbitrary orthogonal axes	MPa
G_{xy}, G_{yz}, G_{zx}	Shear Modulus of the composite material lamina in the three orthogonal arbitrary shear planes	MPa
$\sigma_x, \sigma_y, \sigma_z$	Liner Stress along three arbitrary axes of the lamina	MPa
$\varepsilon_x, \varepsilon_y, \varepsilon_z$	Linear strain along three arbitrary axes of the lamina	-
$\tau_{xy}, \tau_{yz}, \tau_{zx}$	Shear stress in three arbitrary shear planes	MPa
$\gamma_{xy}, \gamma_{yz}, \gamma_{zx}$	Shear strain in three arbitrary shear planes	-
$\overline{Q}_{ij}$	Transformed stiffness tensor (ij=11, 12, 22, 66)	MPa
U_i	Laminate invariants (i=1,2,3,4,5)	-
N_x, N_y	Normal force per unit length in arbitrary x and y directions	N/m
N_{xy}	Shear force per unit length in xy shear plane	N/m
M_x, M_y	Bending moment per unit length in x and y directions	Nm/m
M_{xy}	Twisting moment per unit length	Nm/m
$A_{ij}, D_{ij}, B_{ij},$	Extensional, Bending and Bending-Extensional coupling stiffness	N/m
$\varepsilon_x{}^0, \varepsilon_y{}^0$	Linear strain of the lamina	-
$\gamma_{xy}{}^0$	Shear strain in the shear plane	-
κ_x, κ_x	Laminate curvatures in x and y directions	mm^{-1}
κ_{xy}	Laminate curvature in the xy plane	mm^{-1}
h	Laminate thickness	mm
t_k	Fly thickness	mm

Ψ_i	Specific damping capacity along the normal direction (i=1,2,3)	-
Ψ_{ij}	Specific damping capacity in the shear plane (ij=12, 23, 31)	-
ΔU	Strain energy dissipated under deformation per cycle	Nm
U_{max}	Maximum strain energy	Nm
η_i	Loss factor (i=1,2,3)	-
η_{ij}	Loss factor (ij=12, 23, 31)	-
ξ	Damping ratio	-
Q	Quality factor	-
β	Stiffness proportional damping coefficient	s
f_n	Natural frequency of vibration	Hz
ω_n	Natural frequency of vibration	rad/sec
E^*	Complex modulus of viscoelastic material	MPa
E'	Storage modulus of viscoelastic material	MPa
E''	Loss modulus of viscoelastic material	MPa
δ	Loss angle of viscoelastic material	-
μ_i	Relaxation parameter of viscoelastic material	-
C_i	Internal damping	-

CHAPTER 1

1 INTRODUCTION

In this chapter, the general background of topics covered in the present work such as the gas turbine technology, advanced composite materials, rotor dynamics, rotating internal damping and manufacturing of composite materials and the outline of the thesis work are provided in brief.

1.1 General Background

Gas Turbine is an easily adaptable power source widely employed in diverse applications of aircraft propulsion, marine propulsion, and industrial power generation. Gas turbine engine technology has transformed the aircraft and oceanic transportation into more reliable and efficient compared to the earlier versions powered by piston engines. However, modern gas turbine applications demand continuous performance improvements with a higher degree of reliability and comfort. These improvements have to be achieved by further weight reduction of structural components with a higher level of stress due to the increase in operating temperatures and speeds without compromising in the safety standards. The aeronautical industry's complexity and ever-changing requirements demand extensive research associated with the development of aero gas turbine engines. After decades of investing the vast resources in material science and its allied technological research by the aeronautical industry, all-metal aircraft was transformed into an all-composite aircraft. The composite material blends two or more materials of different material properties to achieve a combination of lightweight, high strength, and outstanding structural flexibilities.

Advanced composite materials have become the standard for a range of products, including the complex-shaped static parts and long fan blades in many aero gas turbine engines. Importantly in the last two to three decades, the composite material has been deliberated as a potential candidate for replacing the conventional metallic rotors and rotating shafts in aero-engine applications. Because of a higher modulus by density value of composite materials than metals, the rotor-bearing system of the longer bearing span is possible without lowering the first flexural critical speed. Fiber metal composite

material made up of alternate layers of metal and composite material brings in composite and metals' combined strengths. Commercially available GLARE®, ARALL®, and CARALL® have been widely used in aircraft structures. The metallic surfaces of metal fiber composite material can easily interface into their respective metallic assemblies. Although fiber metal composites are becoming popular in the recent years, it was a result of decades of research work of various institutions who found the aluminum sheets bonded to the skin of composite material can drastically reduce the fatigue crack growth. In the year 1978, the Delft University of Technology collaborated with Fokker for the development of ARALL and GLARE which entered commercial operation with Airbus A380. In these fiber metal composites, thin aluminium sheets of 0.2 mm thickness are alternatively bonded to the fiber composites to have the combined strengths of aluminium and fiber composites.

Rotor dynamics is an important operational aspect of all the rotating machines based on which each element of the rotor-bearing system is selected and designed to have the least amount of vibrations over its entire operating range. The overall vibration of the rotating machine depends on the critical speeds within the operating range and the response of the rotor-bearing system to the excitation sources. For any rotating machine to be operationally efficient, the vibration of the rotating machine is expected to be within the acceptable limits. The excessive vibration levels encountered by the rotating machine induces operational discomfort which results in eventually reducing the operating life span of the vehicle it is powering. Advancing the critical speeds above the operating range of a rotor-bearing system reduces the vibration of the rotating system to a great extent. Hence composite material shaft is an ideal option in a supercritical high-speed rotor-bearing system having a flexural mode close to its operating speed if it can push the critical speed beyond its operating speed range. However, the use of composite material is quite challenging as it is more expensive and complicated to design as well as to manufacture compared to the metallic shaft.

Composite material brings in material damping into the rotor-bearing system. Rotating internal damping (RID) from the rotors induces instability in the rotor-bearing system in contrast to the stabilizing effect provided by the external damping from the supports. When the amount of RID in the rotor-bearing system is beyond the threshold limit, it

induces the rotor dynamic instability which can be catastrophic if not detected and rectified in time. RID was detected in the industrial turbines in the early years of the 20th century. Initially, the cause of instability was attributed to the internal friction in the rotor joints and subsequently to the material of rotating parts. Most of the research studies carried out over the years to understand and model the internal damping mechanisms in rotor-bearing systems are based on frictional joints with a very few on the material damping. The presence of viscoelastic composite material increases the internal damping content of the rotating shaft which otherwise is negligible in a metallic shaft. The material damping in composite materials is primarily due to the presence of the matrix which is the binding element. Hence the volume fraction of the matrix shall be kept at an optimal level to minimize or maximize the damping based on the requirement of the applications. To eliminate the rotor dynamic instability within the operating speed of the rotor-bearing system, material damping of composite materials along with the frictional damping of joints in the rotating system requires special attention in the design of high-speed rotor-bearing systems. Hence the right combination of composite material with the least amount of damping to avoid or appropriately place the resonances of the rotor-bearing system can drastically reduce the vibrating stresses to improve the overall fatigue life of the rotating machinery.

The analytical and numerical studies with subsequent field trials of the composite helicopter tail rotor and automotive drive shafts have complemented the design and application of composite material in rotating shaft applications bringing in many advantages to the end-users. All these studies have been on low to medium speed applications where the complexities are far lesser compared to the high-speed gas turbine of aero application. Some of the issues involved in the development of an all-composite aero gas turbine engine were addressed to reduce the total engine weight and increase the thrust-weight ratio beyond 20:1 (Gupta 1998).

Manufacturing of composites is complex compared to the metallic parts in high-speed machinery. Hence the use of composite material shaft in a high-speed rotor-bearing system demands extraordinary advantage to replace the conventional metal shaft. Therefore, extensive evaluation of the performance of the composite material shaft in the actual working conditions of high-speed applications is essential which would

eventually decide the prospect of the application and prepare a ground for the application. In this thesis work, the dynamic behavior of the hybrid composite shaft in a high-speed rotor-bearing system is evaluated to verify the suitability and the advantages over the existing shaft material. The research was carried out by studying the available research work already carried out in the rotating shaft domain. The research work was executed by extensively carrying out numerical analysis and experimental characterization.

1.2 Outline of the Thesis

The present thesis on "Dynamic Behaviour of "Hybrid Composite Shaft Rotor-Bearing System" of an Aero Gas Turbine Engine is presented in the following chapters:

Chapter 1: Basics of a gas turbine engine, rotor dynamics, rotating internal damping, and composite material for an aero gas turbine engine.

Chapter 2: Various research works carried out by the experts in the rotating composite shaft, the research gaps, and the objectives of the present work.

Chapter 3: Mathematical formulations of mechanics and dynamics of the composite laminate, material damping, rotating internal damping, and rotor dynamic analysis.

Chapter 4: Preliminary rotor dynamic analysis and parametric study of three high-speed rotor-bearing systems for the composite material shaft, rotor dynamic evaluation of hybrid composite material shaft, experimental characterization of hybrid composite material beam samples for the tensile, flexural strength and material damping using the modal testing and dynamic mechanical analysis, material damping of tube samples.

Chapter 5: Results and discussions of the rotor dynamic analysis of composite/hybrid composite shaft rotor-bearing system and experimental characterization of test samples.

Chapter 6: Rotor dynamic analysis of the remodeled hybrid composite shaft power turbine rotor-bearing system based on the numerical analysis and experimental characterization results.

Chapter 7: Conclusions of the thesis and the future works required to be carried out.

CHAPTER 2

2 LITERATURE SURVEY

The detailed literature survey carried out in this thesis work was aimed at understanding the progress of composite material technology in rotating shafts and its relevance to high-speed rotor-bearing systems. From the present thesis point of view, based on the top-down research model, literature survey was carried out with the following aspects.

- Past research works on the state-of-the-art composite material rotating shaft technologies
- Analytical and numerical composite shaft modeling techniques using the beam and shell formulations
- Internal damping formulations in the rotor dynamic analysis
- Various hybrid forms of composite materials research
- Investigations in the theoretical and experimental damping estimation techniques
- Model updating techniques used in updating the damping values in various structural problems.

2.1 Composite Material Shaft Studies

The research and investigation of the composite material shaft is being progressed along with the advancements in numerical computation. The classical beam and shell theories of homogenous materials have been effectively extended to formulate composite material shafts and rotors considering the variations of composite material compositions, layers stacking orientations, bonding between the elements, etc., The initial theoretical formulations of composite material shaft were based on the one-dimensional equivalent modulus beam formulations. Thin-walled circular tube boron-epoxy composite material helicopter tail rotor driveshaft popularly known as Zinberg and Symonds composite material shaft was one of the first documented work on composite material shaft (Zinberg and Symonds 1970). The theoretical and experimental results of Zinberg and Symonds had affirmed the advantages of the composite shaft over aluminum alloy shaft. The critical speed of the simply supported

boron-epoxy tubular shaft of 10 layers of varying layer sequences was calculated using the classical equivalent modulus beam theory (EMBT). The critical speed of the boron-epoxy tubular shaft for the layer orientation of [90, 45, -45, 0_6, 90] was estimated at 5840 rpm. The experimental unbalance response test was used to predict the first critical speed at 6000 rpm by extrapolating the response obtained at the sub-critical speed region. The EMBT used in the investigation does not account the shear deformation, coupling of bending and stretching. Rotor dynamic experiments were carried out on the composite shaft made up of graphite-epoxy with and without the lumped mass disks (Zorzi and Giordano 1985). Experiments were conducted on two filament wound graphite-epoxy shafts of different layup orientations and compared with the aluminum shaft. The results from the investigation reflected the advantages offered by the composite shaft.

The Timoshenko beam theory which takes into account the shear deformation and rotation bending effects was used to determine the stiffness, strength, and dynamic stresses under a known unbalance value for the optimized design of graphite-epoxy composite shaft (Bauchau 1983). The numerical and experimental investigations carried out included the determination of shaft stiffness, strength characteristics and dynamic stresses under the rotating unbalance conditions. The composite shaft of both uniform and variable wall thickness operating in the sub-critical region was considered for the analysis. The design optimization was carried out at a constant volume constraint which included the different configurations of variations in the number of plies and orientation angles. In the optimal configuration arrived, the natural frequency was increased by about 21 to 44% and the bending stress was decreased by about 48 to 59%.

Timoshenko beam theory with the additional shear-normal and bending-stretching effects was used in the graphite-epoxy thin composite material shaft (Gubran et al. 2000). The variable wall thickness segmented composite shaft was modeled as a simply supported segmented beam with varying wall thickness. It was found that by varying the wall thickness in segments without increasing the shaft mass, the natural frequency of the rotating shaft was increased by 12-17%. It was also found that the maximum stresses in the axial direction due to the unbalance and torque transmitted were lesser for the variable thickness shaft compared to uniform thickness shaft. Timoshenko beam

6

theory (TBT) was used for the comparison of the rotor dynamic behavior of steel, composite shaft, and a functionally graded composite rotor shaft was carried out (Koteswara et al. 2013). The rotating shaft was mounted on two flexible bearings at its ends. The theoretical study was established for the estimation of kinetic energy and the strain energy of the shaft. The equation of motion of shaft was formulated by using the finite element method. The numerically illustrated study presented the results of the frequencies, mode shapes, Campbell diagram and transient response due to the unbalance mass of disks of the rotor-bearing system.

Donnell's thin shell theory was incorporated in the Timoshenko beam theory to carry out the rotor dynamic analysis of composite tubes (Henrique et al. 1987). Donnell's shell theory uses the simplifying shallow-shell hypothesis for the circular cylindrical shells. Approximate finite element procedure based on the Ruhl and Booker approach was used to derive the stiffness matrix of the rotating composite shaft. Donnell's shell theory is found to be more suitable for the shallow shells of smaller length by radius ratio. Sander's shell theory is found to be consistent and accurate for medium length shells. Love's first approximation shell theory is appropriate for shells with a larger length by radius ratio. The various forms of thick and thin shell theories were used to evaluate the critical speeds of an arbitrarily laminated composite hollow shaft (Kim and Bert 1993). The effects of the various shell theories, the thickness-shear flexibility, and the bending-twisting coupling on the critical speed were investigated. The Sanders first-order approximation shell theory was used to derive the governing equations of rotating composite shaft. The formulation used for the composite hollow shaft also included the Love's first approximation theory, Donnell's shell theory, and other shell theories for the combined effects of torsion and rotation. As an example of the application of the theory, a closed-form solution was presented for a simply supported drive shaft.

An investigation of the free vibration characteristics in flexural modes of composite cylindrical tubes using both the beam and shell theories was carried out for the potential use of composite shaft (Singh and Gupta 1994). The comparison of the first circumferential mode value obtained from the beam and shell formulations was carried out. It was found that the equivalent modulus beam theory cannot predict changes in the flexural frequency values caused by a change in the stacking sequence. The

viscoelastic damping values were assumed, and the system loss factor values were determined for the various modes by using the complex modulus approach in the beam and shell theories. The layer-wise beam theory (LBT) derived from the layer-wise shell theory was used for the flexural vibration analysis of a composite material cylindrical tube shaft supported on the general eight coefficients bearings (Singh and Gupta 1996). The results obtained from the LBT were compared with that of the EMBT results. For the symmetrical stacking sequences, the difference between the results obtained from the two theories was found to be negligible. For the unsymmetrical stacking sequences, the EMBT was found to be resulting in inaccurate predictions of the rotor dynamic behavior of the composite shaft. From the investigation, it was also found that the LBT formulation gives a more realistic representation of actual deformation and stress distributions in different layers.

The effect of the stacking sequence and the coupling mechanisms of the composite material laminates on the natural frequencies of rotating composite shafts was investigated using the modified beam theory and layer-wise beam theory (Gubran 2005a). The modified equivalent modulus beam theory (MEMBT) was formulated based on the Bresse-Timoshenko beam theory included with the transverse shear deformation, rotary inertia, and gyroscopic effects. The MEMBT was also included with the bending-twisting, shear-normal, and the bending-stretching coupling effects. The longitudinal and in-plane shear moduli were taken into considerations in the MEMBT at the ply level. The Zinberg composite shaft was analyzed using both MEMBT and LBT. The critical speed values obtained from the MEMBT and LBT were at 5332 rpm and 5620 rpm respectively.

A simple spinning laminated composite shaft model was analyzed using the continuum-based Timoshenko first-order shear deformation beam theory (Chang et al. 2004b). The strain energy of the shaft was estimated by adopting a three-dimensional constitutive relation of material with the help of multiple transformations of coordinate systems. The extended Hamilton's principle was employed to derive the governing equations. The model included the transverse shear deformation, rotary inertia, and the gyroscopic effects along with the coupling effect due to the lamination of composite layers. The numerical finite element method was used to approximate the governing equations by

8

a system of ordinary differential equations. The critical speed of the Zinberg composite shaft calculated using this model was found to be at 5762 rpm.

A simplified homogenized beam theory (SHBT) was used to develop a finite element beam model to evaluate the natural frequencies and instability thresholds of a rotating composite shaft (Sino et al. 2008). The homogenized beam parameters such as flexural and shear stiffness were evaluated using an energy formulation that simultaneously considered the internal damping in the form of specific damping capacity along with the other parameters such as stacking sequences, fiber orientation, transverse shear effects. The influence of laminate parameters, the stacking sequences, fiber orientation, the transverse shear effect on natural frequencies, and stability threshold were studied. The Zinberg composite shaft critical speed calculated using the SHBT model without the shear effect was found to be at 5767 rpm.

The Euler-Bernoulli beam theory without the rotary inertia and shear deformation was used for the vibration analysis of a cross-ply laminated composite drive shaft with its intermediate joint modeled as a frictionless hinge (Qatu and Iqbal 2010; Iqbal and Qatu 2010; Iqbal et al. 2008). The Zinberg composite shaft was analyzed using the Euler - Bernoulli beam formulation and the critical speed was found to be 102.47 Hz. The study focused on obtaining an exact solution for a two-segmented shaft with different shaft properties for each segment. The hinge mass was modeled as two equal concentrated masses on each side of the joint. The cylindrical shaft with a uniform wall thickness and the cross-ply shaft with no bending twisting coupling was considered for the analysis. In the analysis, it was assumed that the amplitude of the free vibrations was sufficiently small, and the in-plane motion was de-coupled from the transverse motion. The study highlighted the importance of treating the whole system rather than selecting independent shaft segments and adding the mass of the hinge joint in the analysis. The added mass on the hinge reduced the natural frequency by more than 10%.

A beam model was developed using the first-order shear deformation beam theory (FSDBT) for the static and vibration analysis of the composite thick beams and shafts (Hajianmaleki and Qatu 2012). Both classical beam model (CBT) and FSDBT beam models were evaluated, and the analysis indicated CBT results were not accurate for slenderness ratio of 20. The FSDBT model was modified for the static and dynamic

analysis of composite beams and shafts by including the various laminate coupling, shear deformation and rotary inertia. The results obtained from FSDBT was compared with a three-dimensional finite element model and verified with the experimental results. Besides, the model was applied to the tubular cross-section beams and compared with the experimental data. The results obtained from the FSDBT were found to be close to 3D FEM and experimental results. The critical speed of the Zinberg shaft calculated using the FSDBT beam model was found to be 90.36 Hz.

A parametric study was carried out using ANSYS shell element to evaluate the effect of stacking sequences and materials on the eigenfrequencies of composite tube-shafts (Alwan et al. 2009). The results from the parametric study were found to be encouraging for designing the composite shafts for different requirements. The dynamic study carried out included the effect of different materials, stacking sequences on the eigenvalues of composite materials. The study was aimed at the comprehensive view of the numerical and experimental investigation of rotating composite shafts for the estimation of eigenvalues, material damping, and unbalance response. Eigenfrequencies of the composite tubular shafts and solid shafts were estimated through modal testing and compared with the FEM results. ANSYS shell element used for the modeling of the composite material shaft was based on the Mindlin-Reissner shell theory. The Mindlin-Reissner shell theory is an extension of the Kirchhoff-Love shell theory. Mindlin-Reissner shell theory which takes into account the shear deformation through the thickness is analogous to the Timoshenko beam theory and the Kirchhoff-Love shell theory which does not account for the shear deformation is analogous to the Euler-Bernoulli beam theory.

The advanced beam and shell formulations based on higher order theories are being used in the modal and rotor dynamics analysis of multi-layered composite structures to enhance the solution accuracy and effectiveness of lamination properties. The advanced finite shell/plate elements with variable kinematics formulated based on the higher order Carrera Unified Formulation (CUF) was used for the analysis of laminated shell structures (Carrera et al. 2018; Filippi et al. 2018). The node-dependent kinematics one-dimensional beam elements developed within the Carrera unified formulation was used in the rotor dynamic analysis of the slender shaft (Filippi et al. 2019). The dynamic

stiffness method was employed in the vibration analysis of laminated shallow curved beam using the trigonometric shear deformation beam theory (TSDBT) which eliminates the requirement of shear correction factor in the formulation (Jun et al. 2014). The generalized differential quadrature (GDQ) method combined with the third-order shear deformation theory (TSDT) was used to perform the parametric static and free vibration analysis of functionally graded conical shells reinforced by carbon nanotubes (Nejati et al. 2017). Critical speed analysis of arbitrarily oriented rotating doubly-curved shells made of functionally graded materials was carried out using the generalized differential quadrature (GDQ) method combined with the higher order shear deformation theories to minimize the errors along with the additional provision to apply the rotating speed about a general axis of the global reference system (Tornabene 2019).

Vibration analysis of rotating composite shafts containing randomly oriented reinforcements was carried out using the finite element method (Chang et al. 2004a). The Mori-Tanaka mean-field theory was used to account for the interaction at the finite concentrations of reinforcements in the composite material. The effective elastic moduli of the composite material were expressed as a function of the phase properties, volume fraction, and orientation angles of its constituents. The glass-epoxy rotating shaft of layer orientation [90, 45, -45, 0_6, 90] with fibers distributed in four different orientations was analyzed for the variation in volume fraction and aspect ratio of fiber inclusions. The investigation revealed that the contents and orientation of reinforcements influenced the dynamic characteristics of the composite shaft. It was also found by the analysis that the increase in aspect ratio and volume fraction of fiber reinforcements increased the critical speed of the composite shaft.

The analysis of the vibratory behavior of rotating composite shafts containing isotropic rigid disks and supported on the bearings modeled as springs and viscous dampers was carried out using a hp- version of the Finite Element Method (Boukhalfa and Houdini 2010). A hierarchical finite element model of a beam with six degrees of freedom per node was developed. The assembly was made by the standard version of the finite element method for several elements along with the establishment of the kinetic energy and the strain energy of the system in the equations of motion. In this study, the

transverse shear deformation, rotary inertia, and gyroscopic effects, as well as the coupling effect due to the lamination of composite layers were incorporated. A program was elaborated for the calculation of the eigenfrequencies and critical speeds of the system. The critical speed calculation of the Zinberg composite shaft was carried out and the result was found to be at 5760 rpm close to the value of the original work.

The rotor dynamics of the composite shaft using the hybrid combination of glass, high strength graphite, and high modulus graphite fibers in the epoxy matrix had shown a substantial payoff in terms of critical speed that could be achieved. The effect of anisotropy of the material was analyzed in advanced anisotropic applications of composite and hybrid materials (Reissner and Tsai, 1974). In this theoretical work which is one of the pioneering works leading into orthotropic and hybrid materials, the stresses and deformations in elastic thin walled, prismatical beams subject to axial forces, bending forces and twisting moments were investigated. The various properties of composites of orthotropic fibers with isotropic and transversely isotropic fibers were analyzed (Tamara and Carl 1991). The research work was focused on the morphology of the fiber that can have a significant effect on composite properties and stress distributions in a composite cylinder. The classical form of analytical expressions was presented for four of the five effective elastic constants of a transversely isotropic composite material containing orthotropic fibers. The properties of composites with orthotropic fibers were compared to those of isotropic and transversely isotropic fibers. It was shown that the morphology of the fiber can have a significant effect on composite properties. It was also shown that fiber morphology has a significant effect on the stress distributions in a composite cylinder.

An optimization study of hybrid high modulus high strength carbon fiber reinforced plastic composite drive shafts was carried out (Montagnier and Hochard 2013). The study yielded some general rules for designing optimum composite shaft such as layers sequencing using ±45°, 90°, 0° layers for increasing the torque resistance, torsional buckling and axial stiffness without any use of optimization algorithms. The effect of hybrid reinforcement on the performance of filament wound hollow shaft composed of hybrid filaments including a combination of carbon, glass, and aramid fibers were analyzed (Mateen et al. 2018). The FEA model using ABAQUS was developed and

verified by the experimental model manufactured using filament winding technique employing the suitable matrix and reinforcement systems. The shafts were tested for the torsional characteristics, hardness, density, and chemical reactivity. The results showed that carbon fiber reinforcement shows the best results in terms of torsional characteristics. In terms of chemical reactivity, the carbon-glass hybrid reinforcement exhibited minimum degradation. Furthermore, it was also found that hybrid reinforcements containing carbon-aramid fibers showed better results in terms of density and surface hardness. The natural frequency results of hybrid carbon and glass fiber reinforced composite tube shafts with carbon nanotubes inserted were estimated (Udatha et al. 2019) using the MEMBT by including the coupling effects. The numerical results obtained were found to have a good match with experimental results.

2.2 Rotating Internal Damping Studies

Various investigators investigated modeling and solving of RID after General Electric encountered destructive vibrations in the compressors of their blast furnaces. Based on the analytical work (Kimball 1926) and the experiments (Newkirk 1924) carried out at General electric, it was concluded that the rotor internal damping due to the frictional joints of rotors caused the unstable vibrations while operating above the first critical speed. The viscous damping model (Rayleigh 1945) was based on the dissipation of energy by the fluid when in contact with the structure now popularly known as proportional viscous damping. Both the viscous and hysteretic forms of internal damping in the rotor-bearing systems were studied with the viscous damping factor directly incorporated in the Eigen analysis using the Rayleigh proportional damping (Dimentberg 1961; Gunter 1966; Vance and Lee 1974). As the numerical methods became popular in the modeling of rotor-bearing systems in the coming years, investigators attempted to incorporate the internal viscous and hysteretic material damping factors in the finite element models of the rotor-bearing system.

A finite element formulation of the rotor-bearing system including the rotating internal damping was developed where both the viscous and hysteretic damping forms were incorporated into the finite element model (Zorzi and Nelson 1977). The analysis results indicated that both forms of internal damping destabilize the rotor system and induce

non-synchronous forward precession. According to the study, the viscous damping does not induce instability until the first critical speed is reached, whereas the hysteretic form destabilizes the forward processional modes at all speeds. The study also stated that the stabilizing effects of anisotropic bearing stiffness and external damping increase the threshold speed of instability. It was concluded that the finite element simulation of rotor-bearing systems can be improved by modeling internal friction effects in studying turbomachinery stability and can assist the engineer in the proper selection of bearing characteristics to ensure the safe high-speed operation. Subsequently, the rotating internal damping was included along with the shear deformation in the finite element formulation used to perform the unbalance response analysis of the rotor-bearing system (Ozguven and Ozkan 1984). Both the theoretical and experimental studies carried out (Wettergren 1997) had shown that the hysteretic damping factors can be replaced with an equivalent viscous damping. Studies were carried out to derive an accurate formulation of hysteretic damping in the form of equivalent proportional damping, non-viscous damping, etc., for the modeling of the material damping in rotor dynamics (Laszlo 2000). The modeling of hysteretic damping of the shaft material in the rotor dynamics of rotor-bearing systems was investigated (Genta and Amati 2010). Simplified equivalent viscous damping and non-viscous damping formulations were considered in the rotor dynamic analysis of viscoelastic material shaft.

The effect of viscous and hysteresis damping on the rotor dynamic instability of supercritical composite material shaft supported on the dissipative supports was investigated (Montagnier and Hochard 2007). The composite shaft was modeled using the Euler-Bernoulli beam theory which includes the translational inertia, rotary inertia and gyroscopic moments without the transverse shear effects. The internal viscous or hysteretic damping was included in the element formulation using the equivalent viscous damping coefficient. In the case of infinitely rigid bearings with viscoelastic suspensions, it was established that viscoelastic supports increase the stability of long shafts, thus compensating the loss of efficiency of classical bearings. The instability criteria had shown that the coupling of rigid modes due to the external damping and shaft modes was more important than the damping factor. It was found that the comparisons between viscous and hysteretic damping conditions lead to the conclusion

that an appropriate material damping model is essential to be able to assess these instabilities. In the case of elastic dissipative bearings, results obtained were compared with the results of Zorzi and Nelson finite element model. The dynamic investigation of bidirectional functionally graded rotating shaft was carried out by incorporating the viscous and hysteretic damping based on the internal damping models of Zorzi and Nelson (Koteswara et al. 2020). It was found by the study that the internal viscous damping gives more stability to the rotor-bearing system than that of the hysteric damping.

Augmenting thermodynamic field (ATF), a thermomechanical coupled method was used (Roy et al. 2008) to model the internal material damping in the viscoelastic rotor-shaft of the rotor-bearing system. Stability limit speed and unbalance response of the rotor-bearing system was predicted using the ATF technique. The composite shaft made of the aluminum matrix reinforced with carbon fibers was found to have postponed the critical speeds. Dynamic behavior of a composite beam formed by the concentric layers of steel and aluminum was also studied in time domain using ATF and anelastic displacement field (ADF) techniques with the viscoelastic parameters extracted from the storage modulus and loss factor reported in the handbooks using the genetic algorithm (Roy et al. 2009). It was found that the ADF approach is more convenient to apply than the ATF approach and by proper placement of the composite layers and proper selection of thickness ratios, the first natural frequency may be sufficiently postponed leading to reductions in vibration response.

A simply supported carbon/epoxy composite tube mounted on viscoelastic supports was studied using an approximation of the Rayleigh-Timoshenko equation (Montagnier and Hochard 2014). The composite material behavior was described in terms of modulus and loss factor using the beam formulation based on the equivalent complex modulus beam theory (ECMBT). The damping process was assumed to be hysteretic; the hysteretic damping was expressed in terms of the equivalent viscous model. The coupling mechanisms on the unsymmetrical composite laminate and the end fittings investigated using ABAQUS finite element model were found to have a negligible influence on the critical speed. The transverse shear and the supports stiffness were found to have the greatest effect. The threshold speed was obtained in the form of an

analytical criterion. The composite drive shafts consisting of $\pm45°$ or $\pm30°$ plies were found to be not suitable for use in the supercritical regime due to their very high loss factors amounted up to 2.0% and 1.2%, respectively. The composite shaft configurations including 0° plies tested were found to be less dissipative and to be stable up to the third flexural critical speed.

2.3 Hybrid Fiber/Metal Shaft Studies

The dynamic study of hybrid shafts made of carbon/glass fiber reinforced composite tubular laminates sandwiched between metal tubes of steel/aluminum inside and outside (Gubran 2005b) found improvements in dynamics and reduction in deformations of hybrid tubes. The layered finite degenerated shell element with transverse shear deformation was employed for the analysis. The dynamic analysis indicated the advantage of hybrid shafts over metallic and composite shafts in terms of reduction in cross-sectional deformation and improved dynamic performance. The hybrid composite shaft was found to be useful in placing the natural frequencies away from the operating range by variations in the laminate parameters. Experiments were carried out to study the static torsion capability of a hybrid aluminum/composite drive shaft fabricated using the wet filament winding method (Mutasher et al 2005). The hybrid shaft was fabricated by winding glass and carbon fibers onto the aluminum tube with different winding angles, numbers of layers, and stacking sequence. The torque-angle-of-twist response was obtained, and the failure modes of the hybrid shaft were studied. The results indicated that the static torque capacity for a winding angle of 45^0 was larger than that of the 90^0 for both the glass and carbon fibers. For the [+45/-45]$_{3s}$ laminates, the maximum static torsion of carbon fibers was found to be approximately 36% higher than the glass fibers. The finite element method was also used to analyze the hybrid shaft under static torsion (Mutasher 2009). ANSYS finite element software was used to perform the numerical analysis of the hybrid shaft. The analysis results indicated that the static torque capacity was significantly affected by changing the winding angle, stacking sequences, and the number of layers. The maximum static torsion capacity of aluminum tube wound outside by six layers of carbon fiber/epoxy

composite at a winding angle of 45^0 was 295 Nm. Good agreement was obtained between the finite element predictions and experimental results.

The various considerations to be followed in selecting the fiber/metal composite technology for the future aircraft were deliberated and it was found that the fiber/metal technology can lead to significant weight reduction in future structural applications (Alderliesten and Benedictus 2008). These findings can be extended as the guidelines for general hybrid metal fiber composite material applications. A review of three types of fiber metal laminates of ARALL, GLARE, and CARALL for their properties, bonding, and various testing methods was carried out (Tamer et al. 2011). The bonding and the various types of surface treatments used in metal fiber composite materials were discussed. The effects of surface treatments which improved the metallic surface morphology for better bonding with composite laminates were investigated. Surface treatment methods, such as mechanical, chemical, electrochemical, coupling agents, and dry surface treatments were introduced and showed comparable performance to improve the fiber metal laminates. R&D engineers of Daimler AG and Mercedes AMG jointly developed hybrid composite strut bars replacing conventional steel underbody chassis struts resulting in several benefits (CompositesWorld 2018). Though initially carbon/epoxy composite was selected to replace steel struts, eventually the hybrid fiber-steel combination was opted considering the various structural advantages. The use of metal fiber composites made up of composite material laminates sandwiched between metallic sheets firmly bonded with high-quality adhesives can become an effective replacement of conventional metallic components in high-speed machinery such as gas turbines.

2.4 Experimental Characterization Studies

Characterization of mechanical properties using mechanical testing is widely emphasized to obtain the properties such as the measure of strength, elasticity, viscoelasticity along with the quality of the material under investigation. The macro-level tests using the universal testing machines though are sometimes expensive and time consuming due to the requirement of multiple specimens, they generally provide a reliable set of data that are useful in the material evaluation. The combinations of

ASTM testing standards to be used in the characterization of composite materials were brought out (Adams 1998). The various ASTM test standards widely used by the researchers and engineers for the industrial applications spell out the steps and processes to be followed while carrying out the mechanical characterization tests. The ASTM tensile test method for high strength composites (ASTM D3039/D3039M–17, 2017). ASTM tensile test method for metallic materials (ASTM E8/E8M–16a, 2016), ASTM flexural test method of adhesive bonded laminated Assemblies (ASTM D1184–98, 2012), ASTM flexural test method for composite material (ASTM D790–17, 2017) and ASTM flexural test method for in-plane shear of Hoop wound composite cylinders (ASTM D5448/5448M–16, 2017) explain the specimen requirements, instrumentation and testing procedure to be followed while carrying out the test. The static tensile test of fiber metal laminates was carried out to evaluate the stress-strain behavior along with other dynamic and impact tests (Guida et al. 2012). The static tensile test results obtained as per ASTM D 3039 test standard indicated that the elastic moduli of fiber metal laminates intended for very critical structural applications have a lower elastic modulus and higher failure stress compared to the standard aluminum alloy. The investigation of the tensile, compression and flexural strengths of the combination of natural/synthetic fibers with metal laminates as reinforcement in a polymer matrix was carried out using the ASTM standards (Mohammed et al. 2018). The flexural test which characterizes the interfacial bonding of fiber/matrix was carried out using three-point bending method as per ASTM D790 standard.

The role of adhesion between aluminum sheets and fiber composite prepreg on the mechanical property profiles of carbon-fiber-reinforced metal laminates (CFRMLs) was investigated (Glyn et al. 1997). Differences in adhesive bonding were achieved by using two different aluminum surface treatments, one with a standard P2-Etch procedure and another with a modified FPL-Etch procedure with the subsequent application of a silane coupling agent. Double-cantilever beam tests were conducted to measure the interfacial fracture energy and an increase in interfacial fracture toughness by up to six times was achieved by using the latter method. Optical and scanning electron microscopy were used to study the failure behavior and fracture mechanisms of the CFRMLs. No clear differences were found in laminate mechanical properties

such as tensile strength and Young's modulus. A reduction of 10% in the relative value of the interlaminar shear strength was observed for the laminate with poor interfacial adhesion associated with the P2-Etch method, in both three-point and five-point bending tests. The manufacturing principles of fiber metal laminates and the features related to the composition of hybrid materials such as formability, layup techniques, etc., were discussed (Sinke 2009).

Damping measurement in materials and systems is complex due to the multiple sources from where the damping emanates. The damping survey in composite materials was carried out by including the various fundamental definitions, the measure of damping in terms of specific damping capacity, the bandwidth of half PowerPoint, loss tangent, the decay of free vibrations and the effects of various parameters on the material damping in composite materials (Bert 1980). The survey was carried out from the point of increasing the damping capacity of the material for the control of the resonant response of structures as well as to decrease the material damping as a source of excitation for the dynamic instability in hysteresis induced whirling in rotor-bearing systems in rotating machinery.

The analytical and experimental results carried out for the improvement and optimization of damping in polymer composite materials were summarized at both the macromechanical and micromechanical levels (Finnegan and Gibson 1999). The summary included a relevant review of developments in experimental techniques for measuring damping in composite materials and highlighted the need for further research of damping estimation in hybrid structures. The Survey on various damping research studies on composite damping mechanisms with the methodology of macro-mechanical, micromechanical, and viscoelastic approaches was carried out (Chandra et al. 1999). Some important works related to the improved damping models for thick laminates, improvement of laminate damping, and optimization of damping in fiber-reinforced composites were critically reviewed. The survey highlighted the need for further work on micromechanical studies on lateral and shear mode damping mechanisms.

In a summary of all his previous research investigations on damping in composite materials, it was highlighted that the modal testing by the use of impulsive excitation

in either a single mode or multiple modes of vibration can be used to determine elastic moduli and damping factors of composites and their constituents (Gibson 2000). It was concluded that the modal testing under the various environmental conditions has the potential to be a fast and accurate approach not only for the characterization of intrinsic material properties but also for the quality control and inspection as well. A detailed review of the various types of composite materials including the hybrid composites was carried out which included the various damping models and damping measurement methods adopted by various investigators (Treviso et al. 2015). The detailed review found that the experimental characterization of composites for the estimation of dynamic properties is still far from being standardized and the results seem to be setup-dependent meaning that traditional methods introduce non-negligible sources of damping. The review concluded that even though experimental characterization of composites is not standardized, the better understanding of the physics underlying the energy dissipation mechanisms in composite materials can be addressed by experimental characterization only.

The use of varying definitions and the mathematical expressions of the vast nature of past works add up to the complexities. The definition of loss factor in terms of energy quantities as applied to composite viscoelastic systems was examined and simple relations to express the loss factors of series- parallel arrays of massless viscoelastic springs of composite structures were derived (Ungar and Kerwin 1962). In one of the earliest material damping studies carried out, the hysteretic material and structural damping mechanisms from the structural resonance point of view were analyzed (Lazan 1968). The loss factor values of fiber-reinforced composites were predicted based on strain energy dissipation using the finite element method (Chandra et al. 2003). The investigation was carried out by considering the dissipation of energy due to fiber and matrix and correlate the same with various micromechanical theories such as Saravanos–Chamis damping model. Damping in fiber–interphase–matrix composite was also calculated as an attempt to understand the effect of interphase. The contribution of energy dissipation due to the sliding at the fiber-matrix interface was incorporated to evaluate its effect on loss factors in the fiber-reinforced composite having damage in the form of hairline debonding.

Experimental determination of material damping of composite materials was evolved with the diverse range of applications of advanced composite material in aerospace, automotive, and other scientific research areas such as space sciences. The energy and wave propagation methods in the frequency domain such as the power input method are more of an in-situ method more suitable for the evaluation of structural damping. The impact vibration testing technique on the cantilever beam using the logarithmic decrement of free decay method in the time domain and the estimation of modal loss factor using the 3dB method in the frequency domain are being extensively used for the damping estimation. The experimental dynamic tests were carried out to substantiate the partial differential equation models derived from a cantilevered beam with a tip mass at its free end (Banks and Inman 1991). The experimental dynamic tests were performed using the standard experimental modal analysis and spline inverse procedures. Based on these dynamic tests, the damping in a composite beam was examined for the four models of viscous air damping, Kelvin-Voigt damping, time hysteresis, and spatial hysteresis damping. The material damping of a continuous fiber organic matrix composite cantilever beam test specimen was experimentally determined using an impulse excitation technique (Roger et al. 1991). From the impulsive test results, it was found that the variation of loss factor to be nonlinear with the increasing frequency and insensitive to specimen thickness.

Experimental modal analysis was performed on two hollow tubular shafts supported on anti-friction bearings under non-rotating conditions (Singh and Gupta 1993). The modal testing was carried out on two shafts with 45^0 and 60^0 fiber angles with and without the lumped mass to validate the theoretical predictions carried out using the beam formulations. The damping measurement of the non-rotating composite shaft was carried out by obtaining the logarithmic decrement from the decay plot of the free impulsive vibration response. Results indicated higher damping for the shaft of 60^0 fiber angle and lumped disc mass. As an extension, damping measurements were made on rotating shafts by obtaining the decay curve after filtering out the components other than that corresponding to the damped natural frequency (Gupta and Singh 1998). The primary objective was to evaluate the effect of speed of rotation on the modal damping in the first lateral mode of a composite rotor. Half PowerPoint method was used on the

imbalance response plot to measure the rotor system damping. Damping values so obtained are compared with the theoretically predicted values and with the earlier experimental results of non-rotating composite shafts. It was concluded that damping estimation of the rotating shaft shall be carried by isolating rotating material damping from other sources such as the external damping backed with an accurate theoretical model.

Experimental investigation of the damping of the rectangular carbon-epoxy laminates was carried out using a sinusoidal impulse excitation technique (Talbot et al. 1997). Damping was measured from the temporal decay characteristics following impulsive excitations. The free decay rate was determined from the transient vibration signal by performing the time-frequency analysis. The resonance technique was used for determining the stiffness and damping properties of the cables made of composite materials (Wei et al. 2000). As the resonance frequencies of a system is a function of its material elastic properties and mass, the resonance technique was used to determine the stiffness of a vibrated material through the application of acoustic energy. The damping properties were determined using both the free exponential decay curve and half-peak bandwidth methods. The influence of specimen length and measurement set-up was also investigated. The applicability and accuracy of the resonance technique for a composite structure were discussed. The measured elasticity of optical cables was found to be in good agreement with the derived theoretical value.

A synthesis for the damping analysis of laminate materials, laminates with interleaved viscoelastic layers and sandwich materials was developed using the finite element analysis and experimental investigation using the beam specimens (Berthelot et al. 2006, 2008). The damping of the glass-epoxy laminates was investigated using an impulse technique on beam test specimens. The experimental evaluation of damping was performed on beams of different lengths: 160, 180, and 200 mm to have a variation of the values of the peak frequencies. Beams had a nominal width of 20 mm and a nominal thickness of 2.5 mm. The test specimen was supported horizontally as a cantilever beam in a clamping block. An impulse hammer was used to induce the excitation of the flexural vibrations of the beam and the beam response was detected by a laser vibrometer. Finite element analysis was used to derive the different strain

energies stored in the material directions of the constituents of composite materials. The energy dissipated by damping in the materials and the composite structure was obtained as a function of the strain energies and the damping coefficients associated with the different energies stored in the material directions. The results obtained were compared with the experimental results of the frequency response of the structure. The vibration characteristics of composite beams were experimentally studied by impulse excitation technique under fixed- free boundary condition (Murugan et al. 2015). The glass, carbon and hybrid of glass/carbon laminates were fabricated with two different stacking sequences by hand layup method and tested for evaluating the mechanical properties. The experimentally study found that the stacking sequence influenced the mechanical properties and vibration characteristics of the beams tested.

The free vibration method was used to evaluate the damping behavior of fiber metal laminates (Botelho et al. 2006). The vibration damping results were used to calculate the storage and loss modulus of aluminum T2024-T3 alloy sheets, carbon-epoxy, graphite-epoxy along with the hybrid metal fiber made up of T2024-T3 sheets with carbon-epoxy, graphite-epoxy composite laminates. The vibration testing response was found to be an effective tool in measuring the dynamic properties of hybrid composites. The loss factors of the hybrid structures and the constituent materials were determined by both frequency and time domain test methods (Sarlin et al. 2012). The damping properties of laminated structures consisting of steel, rubber, or epoxy adhesive and glass fiber reinforced epoxy composite laminates were carried out. The loss factor results of the constituent materials were used to estimate the loss factor of the hybrid structures by the rule of mixtures and the results were compared with the experimental results. By using the loss factor results of the constituent materials, the loss factor of the hybrid structures was estimated by the rule of mixtures and the results were compared with the experimental results. It was observed that the use of weight fractions instead of volume fractions in the rule of mixtures provides a good average estimation of the damping behavior of the hybrid structure and the results of the rule of mixtures method can be used as rough estimates during the design phase of hybrids. The characterization of elastic and damping properties of fiber metal laminated hybrid composite material in the frequency domain was carried out using a forced vibration

test (Iriondo et al. 2015). The complex modulus values were extracted from the test results of the forced vibration test. The viscoelastic behavior inherited by the composite material was found to be due to the bonding resin material influencing the damping behavior.

Dynamic mechanical analysis (DMA) is widely used in dynamic characterization of viscoelastic materials as it provides an insight into the interfacial adhesion mechanism of fiber and matrix in terms of storage modulus, loss modulus, and loss tangent. The measurement of flexural modulus and loss factors of high damping composite material beams was carried out using DMA in addition to the free-free method (Benchekchou et al. 1998). The optimization of damping in the structure was also carried out by varying the composite material parameters using ANSYS. The free–free beam test was conducted on two CFRP beams and the measurements were made in a large oven. The beam was suspended by threads at the two nodal points of the first free – free flexural mode of vibration. The loss factor was determined by steady-state sinusoidal excitation of the beam at the fundamental resonance frequency and by applying the logarithmic decrement method to a stored decaying signal obtained after switching off the excitation. DMA was used to evaluate the viscoelastic damping properties of the material sample in terms of storage modulus and loss modulus under the specified temperature and frequency ranges. DMA results indicated lower values for storage modulus and higher loss factors than the free – free beam test.

The experimental investigation of damping enhancements in carbon reinforced composites with carbon nanotubes embedded in the epoxy matrix was carried out (Devalve et al. 2013). The composite material laminates were analyzed using the dynamic mechanical analysis and other modal analysis techniques to estimate the additional damping provided by the carbon nanotubes in terms of loss factor in carbon-epoxy composite material samples. The modal testing techniques of base excitation and impact hammer excitation on cantilever beam samples were also used. DMA was carried out in dual-cantilever mode to measure the material loss factor of each composite sample in the stationary frame of reference.

Finite element prediction was carried out and substantiated by the dynamic mechanical and thermal analysis (DMTA) for the measurement of the stiffness and damping properties of a unidirectional carbon reinforced composite lamina (Pathan et al. 2017). Measurement of the stiffness and damping properties of the constituents of the unidirectional composite was performed by the DMTA analyzer with a load capacity of 35 N in the isothermal frequency sweeps in the range 0.1- 10 Hz at three different temperatures of 25°C, 40°C and 50°C. Tests were performed using the available fixture of a maximum span of 32mm. It was found that the macroscopic material stiffness increases with increasing the imposed frequency and decreases with increasing the temperature. Conversely, material damping decreases with increasing the frequency and increases with increasing the temperature. The axial modulus and corresponding loss factor were scarcely sensitive to frequency and temperature for the carbon fiber composites tested. Finite element predictions were found to be in broad agreement with the experiments. Similarly, an assessment of the vibrational behavior of the three-layered sandwich composite plates was carried out using the analytical formulations and verified using the dynamic mechanical analysis (Ege et al. 2018).

The viscoelastic behavior of pure epoxy, E-glass/epoxy and three hybrid composites made of S-Glass-E-glass/epoxy, Carbon-E-glass/epoxy and Kevlar-E-glass/epoxy were characterized using the dynamic mechanical analyzer over the temperature range of 30ºC to 50ºC at four frequencies of 1, 10, 50 and 100 Hz (Vasudevan et al. 2018). The experimentally obtained storage modulus and loss tangent values were theoretically validated. The results indicated that the Carbon-E-glass/epoxy composites exhibit the highest storage and least loss moduli due to stiffening effect whereas pure epoxy exhibits the least storage modulus and highest loss tangent peak at all the frequencies. It was observed that the glass transition temperature (T_g) increases with the increase in frequency. The sharp decrease in storage and loss moduli were observed in the glass transition zone, which was attributed to the enhanced mobility of polymer chains owing to matrix softening. Using the scanning electron microscopy, the higher debonding regions were seen in tested samples of Kevlar-E-glass/epoxy hybrid composites at higher frequencies.

The dynamic mechanical analysis was used to estimate damping in hybrid carbon fiber elastomer metal laminates (Vincent et al. 2019). The dynamic mechanical analysis was performed on fiber metal elastomer laminates of carbon fiber composites to characterize their temperature and frequency dependent damping behavior. A numerical model was built based on the dynamic mechanical analysis of the constituents and micromechanical studies. Three-point bending DMA experiments on hybrid laminates were simulated and the results were compared with the experimental investigations. Besides, a numerical parameter study on different lay-ups was also carried out. Due to the existence of two glass transitions in the hybrid material which is a complex thermo-rheological situation, Vincent et al. observed that only small frequency ranges can be depicted using the experimentally determined master curves in these temperature ranges. Hence, it was concluded that only small frequency ranges can be depicted with the experimentally determined master curves in these temperature ranges and the depiction of the frequency dependent material behavior with the numerical model in these temperature ranges have to be investigated in the future studies.

The damping characteristics of composite structures made of polymer materials embedded into the phenolic resin matrix fiberglass-reinforced laminates was investigated using single cantilever beam vibration and modal analysis techniques as per the ASTM E756-05 standard (Zeng et al. 2020). For the viscoelastic polymer material test samples, dynamic mechanical spectra were obtained from the dynamic mechanical analyzer TA Q800 in tensile mode. The free vibration decaying test of the composite structure was conducted on a rectangular plate by force hammer method using single point excitation and multi-point response.

Two-dimensional specific damping capacity (SDC) prediction of fiber composite plates was carried out using the various composite material damping formulations (Adams and Bacon 1973; Ni and Adams 1984; Maheri and Adams 1995; Saravanos and Chamis 1991). It was found that the specific damping coefficient predicted using the Saravanos–Chamis theory of arbitrary laminate consistently agrees with the experimental results (Billups and Cavalli 2008). Billups and Cavalli also pointed out the requirement of further studies to find out the reasons for the deviations in the results from these theories. A 2-D analytical model was developed for characterizing the

flexural damping response of the composite laminates (Tsai and Chang 2009). The specific damping capacity was estimated based on the extension of the Ni-Adams model accounting for the energy dissipation contributed by the laminar stresses. The specific damping capacity of [0/-60/60]$_s$ and [0/90/45/-45]$_s$ laminates calculated were compared with the experimental data and the finite element (FEM) results. The analysis results found that the 2-D model was adequate for the evaluation of the damping as the interlaminar stress effect in the 3-D model was not significant. The specific damping capacity of the composite material fly estimated based on the Adams − Bacon theory and Ni-Adams theories were used as loss factor in the rotor dynamic analysis of the rotating composite material shaft (Sino et al. 2009; Montagnier and Hochard 2014; Willy et al. 2017).

The updating of the theoretical model using the experimental results is an important aspect in the vibrational analysis of complex structural problems. Since most of the numerical models, either damping is not included, or an approximated equivalent form is included. Hence damping updating techniques are being developed to improve the accuracy of the numerical models. A survey was carried out to provide an accurate review of the state of the art on model updating concerned with the correction of finite element models by processing records of dynamic response obtained from the tests (Mottershead et al. 1993). An analytical model updating method was presented by using an incomplete set of measured FRF data and the advantages of using FRF data over the modal data was demonstrated (Lin et al. 1994). The FRF measurement using a standard impulse test on three cases including a simple free-free beam in flexural vibration was carried out (Adhikari et al. 2009). The results were incorporated into the stiffness and damping matrix derived by finite element modeling. Adhikari et al. found the modal damping factors recalculated using the damping matrix agree with the measured values.

A finite element model was developed to formulate the stiffness matrices considering the effects of axial, flexural, and rotation on the eigen-nature of rotating composite shaft (Ghoneam 2011). The critical speed of the rotating composite shaft and the instability regions were computed to estimate the dynamic behavior of the system in the resonance state. The results were compared with those obtained by using the finite element method and the experimental measurements using the frequency response

function (FRF) method. An updating formulation was developed (Pradhan et al. 2012) which separately updates the damping matrix from that of updating stiffness and the mass matrix utilizing the concept of normal frequency response functions. A direct structural damping identification method of normal FRFs estimated from the experimental complex FRFs was proposed (Arora 2014) which was subsequently used for the identification of general structural damping. A gradient based inverse sensitivity algorithm was used (Subhajit and Sushanta 2016) for the determination of proportional viscous damping model of fiber reinforced composite beams using the finite element model updating. A method of modeling the damping matrix of a structure from the incomplete experimental modal analysis data combined with a representation of the mass and stiffness matrices developed by the finite element methods and reduced by the standard model reduction techniques using matrix reduction was presented (Minas et al. 1991). Minas et al. employed the matrix reduction technique developed in complex modal, transient, and harmonic dynamic problems to reduce the matrix sizes to achieve faster and less expensive computation. Static reduction techniques that ignore the inertia effects such as Guan reduction and the dynamic reduction techniques which include the inertia effects are being developed using iterative algorithms updating the finite element model damping matrix.

Sub-structuring is a matrix reduction methodology used in the finite element dynamic analysis to reduce the computational effort by condensing the large groups of finite elements into a single super element. In one of the earliest works of substructure technique (Craig and Bampton 1968), a method was presented with an example for treating a complex structure as an assemblage of substructures using the basic mass and stiffness matrices having the geometrical compatibility along the substructure boundaries. The viscoelastic material was modeled using the component mode synthesis combining the robust Craig - Bampton condensation procedure used for dealing with the large-scale viscoelastic damped systems (Lima et al. 2010). The finite element method was used to incorporate the viscoelastic material behavior in the form of storage modulus and loss factors in combination with the frequency-temperature and the elastic-viscoelastic correspondence principles.

2.5 Research Gap found from literature survey

Based on the in-depth survey of literature of the relevant previous works on the dynamics of rotating composite shaft and dynamic characterization of composite/hybrid composite materials, the following research gaps were identified.

1. Most of the rotating composite material shaft research investigations were from the point of low-speed automotive and rotorcraft applications. Limited research works have been published on high-speed composite shaft applications of gas turbines.

2. Very few research works included the effect of material damping of the composite shaft on the rotor dynamic stability as most of the research was on the low-speed subcritical applications. Hence, the estimation of material damping and its modeling as rotating internal damping (RID) in the composite shaft has to be emphasized in detail in the present work.

2.6 Objectives

Considering the research gaps of the previous works of composite/hybrid composite rotating shafts listed above, it was proposed to carry out the present research work with the following objectives.

1. Finite element rotor dynamic modeling and analysis of the high-speed rotor-bearing systems to propose the most appropriate hybrid composite material shaft application. Parametric study to select the best composite material laminate configuration.

2. To fabricate and characterize the hybrid composite material for the estimation of the tensile and flexural strengths based on ASTM standards.

3. Experimental dynamic characterization of the hybrid composite material beam and hybrid tube samples for the investigation of material damping of composite material using the cantilever free vibration method

4. Experimental dynamic mechanical analysis (DMA) for the viscoelastic material characterization of material loss factor over an operating temperature and frequency range.

5. Based on the experimental results, remodel the rotating shaft and carry out the rotor dynamic analysis of the high-speed rotor-bearing system. Finite element analysis of rotor dynamic instability of the rotor-bearing system and its effective control.

CHAPTER 3

3 MATHEMATICAL FORMULATIONS

This chapter lists the important equations of the mathematical formulations for the mass, stiffness, and damping properties of the composite material laminate used in the present work.

3.1 Composite Material Formulations

From the fundamental micromechanics of composite material, the equivalent Young's modulus in the two transverse directions and the shear modulus of the lamina as shown in Figure 3.1 are given by,
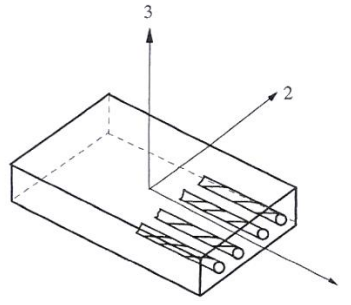
Figure 3.1.   Representation of principal axes in a composite lamina (Kaw 2000)

$$E_1 = V_m E_f + V_f E_m \quad E_2 = \frac{V_m E_f}{V_m E_f + V_f E_m} \qquad G_{12} = \frac{G_m G_f}{V_m G_f + V_f G_m} \tag{3.1}$$

From fundamentals of macro-mechanics of composite material, the orthotropic unidirectional composite lamina is a Plane Stress problem. Due to the small thickness compared to the other dimensions, the stresses in the direction-3 are zero (as $\sigma_3 = \tau_{13} = \tau_{23} = 0$). Hooke's law takes the form

$$\begin{Bmatrix} \sigma_1 \\ \sigma_2 \\ \tau_{12} \end{Bmatrix} = \begin{bmatrix} Q_{11} & Q_{12} & 0 \\ Q_{12} & Q_{22} & 0 \\ 0 & 0 & Q_{66} \end{bmatrix} \begin{Bmatrix} \varepsilon_1 \\ \varepsilon_2 \\ \gamma_{12} \end{Bmatrix} \quad \begin{Bmatrix} \tau_{21} \\ \tau_{31} \end{Bmatrix} = \begin{bmatrix} G_{23} & 0 \\ 0 & G_{31} \end{bmatrix} \begin{Bmatrix} \gamma_{21} \\ \gamma_{31} \end{Bmatrix} \tag{3.2}$$

Q_{ij}, the stiffness tensors of the plane lamina are given by,

$$Q_{11} = \frac{E_1}{1 - \vartheta_{12}\vartheta_{21}} \quad Q_{12} = \frac{E_2 \vartheta_{12}}{1 - \vartheta_{12}\vartheta_{21}} \qquad Q_{22} = \frac{E_2}{1 - \vartheta_{12}\vartheta_{21}} \quad Q_{66} = G_{12} \tag{3.3}$$
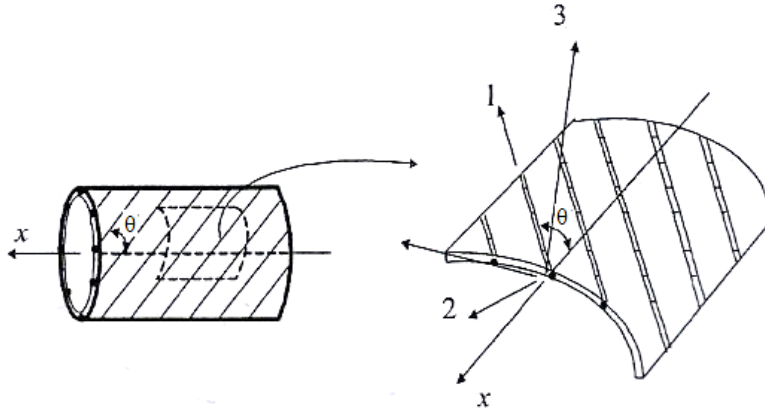
Figure 3.2.   Principal axes on an angle lamina of the tubular shaft (Chang 2005a)

For the angle lamina of a tubular shaft, as shown in Figure 3.2, the expression for the stress-strain relationship and invariants is given as

$$\begin{Bmatrix} \sigma_x \\ \sigma_y \\ \tau_{xy} \end{Bmatrix} = \begin{bmatrix} \overline{Q}_{11} & \overline{Q}_{12} & \overline{Q}_{16} \\ \overline{Q}_{12} & \overline{Q}_{22} & \overline{Q}_{26} \\ \overline{Q}_{16} & \overline{Q}_{26} & \overline{Q}_{66} \end{bmatrix} \begin{Bmatrix} \epsilon_x \\ \epsilon_y \\ \gamma_{xy} \end{Bmatrix} \qquad \begin{Bmatrix} \tau_{yz} \\ \tau_{zx} \end{Bmatrix} = \begin{bmatrix} G_{yz} & 0 \\ 0 & G_{zx} \end{bmatrix} \begin{Bmatrix} \gamma_{yz} \\ \gamma_{zx} \end{Bmatrix} \tag{3.4}$$

$\overline{Q}_{ij}$, the transformed stiffness tensors of the angle lamina are given by

$$\begin{aligned}
&\overline{Q}_{11} = U_1 + U_2 \cos 2\theta + U_3 \cos 4\theta \qquad \overline{Q}_{12} = U_4 - U_3 \cos 4\theta \\[2mm]
&\overline{Q}_{22} = U_1 - U_2 \cos\theta + U_3 \cos 4\theta \qquad \overline{Q}_{16} = \frac{U_2}{2}\sin 2\theta + U_3 \sin 4\theta \\[2mm]
&\overline{Q}_{26} = \frac{U_2}{2}\sin 2\theta - U_3 \sin 4\theta \qquad\quad \overline{Q}_{66} = \frac{1}{2}(U_1 - U_4) - U_3 \cos 4\theta
\end{aligned} \tag{3.5}$$

The laminate invariants U_i are given by,

$$\begin{aligned}
&U_1 = \frac{1}{8}(3Q_{11} + 3Q_{22} + 2Q_{12} + 4G_{12}) \qquad U_2 = \frac{1}{2}(Q_{11} - Q_{22}) \\[2mm]
&U_3 = \frac{1}{8}(Q_{11} + Q_{22} - 2Q_{12} - 4G_{12}) \\[2mm]
&U_4 = \frac{1}{8}(Q_{11} + Q_{22} + 6Q_{12} - 4G_{12}) \\[2mm]
&U_5 = \frac{1}{8}(Q_{11} + Q_{22} - 2Q_{12} + 4G_{12})
\end{aligned} \tag{3.6}$$

The resultant force and moments matrix of the angle lamina is given by

$$\begin{bmatrix} N_x \\ N_y \\ N_{xy} \\ M_x \\ M_y \\ M_{xy} \end{bmatrix} = \begin{bmatrix} A_{11} & A_{12} & A_{16} & B_{11} & B_{12} & B_{16} \\ A_{12} & A_{22} & A_{26} & B_{12} & B_{22} & B_{26} \\ A_{16} & A_{26} & A_{66} & B_{16} & B_{26} & B_{66} \\ B_{11} & B_{12} & B_{16} & D_{11} & D_{12} & D_{16} \\ B_{12} & B_{22} & B_{26} & D_{12} & D_{22} & D_{26} \\ B_{16} & B_{26} & B_{66} & D_{16} & D_{26} & D_{66} \end{bmatrix} \begin{bmatrix} \varepsilon_x^0 \\ \varepsilon_y^0 \\ \gamma_{xy}^0 \\ \kappa_x \\ \kappa_y \\ \kappa_{xy} \end{bmatrix} \qquad (3.7)$$

$$\begin{bmatrix} [N] \\ [M] \end{bmatrix} = \begin{bmatrix} [A] & [B] \\ [B] & [D] \end{bmatrix} \begin{bmatrix} [\varepsilon^0] \\ [\kappa] \end{bmatrix}$$

The expressions for the extensional stiffness matrix A_{ij}, bending stiffness matrix B_{ij} and bending-extensional stiffness matrix D_{ij} are given by,

$$A_{ij} = \sum_{k=1}^n [\bar{Q}_{ij}]_k (h_k - h_{k-1}) \qquad\qquad i=1,2,....6$$

$$B_{ij} = \frac{1}{2}\sum_{k=1}^n [\bar{Q}_{ij}]_k (h_k^2 - h_{k-1}^2) \qquad\qquad i=1,2,....6 \qquad (3.8)$$

$$D_{ij} = \sum_{k=1}^n [\bar{Q}_{ij}]_k (h_k^3 - h_{k-1}^3) \qquad\qquad i=1,2,....6$$

$$h = \sum_{k=1}^n t_k$$

h is the thickness of the laminate, t is the thickness of the lamina, n is the number of laminae in the laminate.

The expression for the curvature and strain components of laminate are given by

$$\kappa_x = \frac{C_{11}}{h^*} M_x \quad \kappa_y = \frac{C_{12}}{h^*} M_y \quad \kappa_{xy} = \frac{C_{16}}{h^*} M_{xy} \qquad h^* = \frac{h^3}{12} \qquad (3.9)$$

$$\varepsilon_x = z\kappa_x \qquad \varepsilon_y = z\kappa_y \qquad \gamma_{xy} = z\kappa_{xy} \qquad\qquad (3.10)$$

h^* is a normalizing factor, C_{ij} is a normalized flexural compliance matrix, z is the distance from the lamina to the mid-plane of laminate.

3.2 Viscoelastic Material Damping Formulations

The dynamic behaviour of composite material may be modeled as a mix of pure solid-state elastic and pure fluid state viscous behaviour due to the viscoelastic material property of matrix. In a conventional viscous damping model, the damping force is

modeled as a function of volume, shape, and velocity of an object traversing in the damping media. The area of the hysteretic loop shown in Figure 3.3 denotes the amount of energy lost per unit volume of the material undergoing cyclic loads due to damping where the damping force does not depend on the frequency of oscillation of harmonic motion.
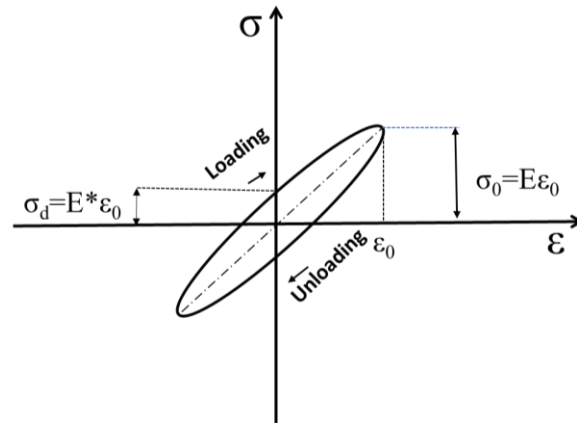
Figure 3.3.   Hysteretic damping cycle of a typical viscoelastic material

The viscoelastic materials dissipate a part of the strain energy when subjected to external load inducing the phase shift between stress and strain at a loss angle δ. For the sinusoidal vibratory motion of a viscoelastic material of frequency ω having the maximum deformation amplitudes of ε_0 and γ_0, the stress-strain relationship is linear and the shear directions are given by

$$\sigma = \varepsilon_0 E \cos \delta \sin \omega t + \varepsilon_0 E \cos \omega t \sin \delta$$

$$\tau = \tau_0 G \cos \delta \sin \omega t + \tau_0 G \cos \omega t \sin \delta \qquad (3.11)$$

The complex modulus which represents the young's modulus of viscoelastic materials in the complex form in the frequency domain

$$E^* = \frac{\sigma^*}{\varepsilon^*} = \frac{\sigma_0}{\varepsilon_0} e^{i\delta} = E' + iE'' \qquad G^* = G' + iG'' \qquad (3.12)$$

The dynamic elastic storage modulus E' and G' which represent the energy stored in linear and shear directions during deformation are given by

$$E' = E \sin \delta \quad G' = G \sin \delta \qquad (3.13)$$

The relationship of loss modulus (E'') which represents the amount of energy lost during the release of the external load with the storage modulus is given by

$$\frac{E''}{E'} = \tan \delta_E = \eta_E \qquad \frac{G''}{G'} = \tan \delta_G = \eta_G \qquad (3.14)$$
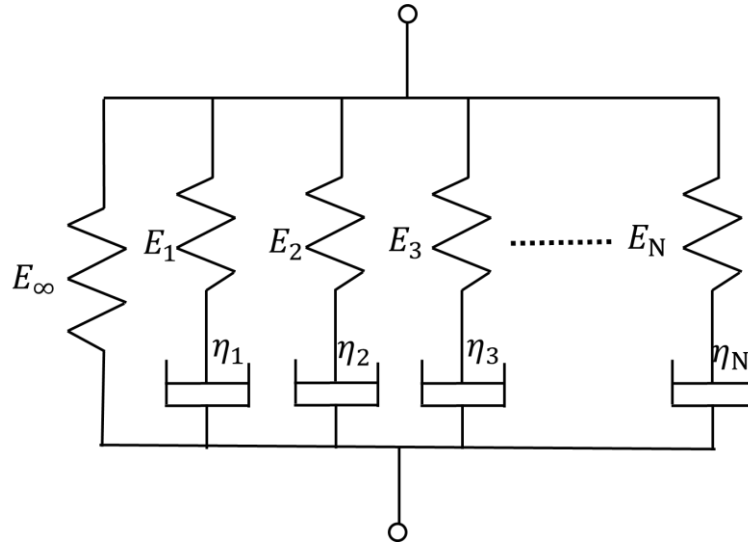
Figure 3.4.   The generalized Maxwell model of viscoelastic material

The generalized Maxwell viscoelastic model is shown in Figure 3.4. The Prony series of Prony parameters E and $\boldsymbol{\eta}$ of time constant τ along with the time varying relaxation tensile modulus E(t) consisting of N number of decaying exponentials is given by (David 2001)

$$E(t) = E_\infty + \sum_{i=1}^{N} E_i e^{\frac{-t}{\tau_i}} \qquad (3.15)$$

Similarly, the shear and bulk modulus are given by

$$G(t) = G_\infty + \sum_{i=1}^{N} G_i e^{\frac{-t}{\tau_i^G}} \qquad K(t) = K_\infty + \sum_{i=1}^{N} K_i e^{\frac{-t}{\tau_i^K}} \qquad (3.16)$$

A general model for viscoelastic material is given by

$$\sigma = E\left(\varepsilon - \int_{-\infty}^{t} G(t - \tau) \frac{d\varepsilon(\tau)}{dt} d\tau\right) \qquad (3.17)$$

G(t-τ) is the damping kernel of viscoelastic material known as the relaxation function of the material of internal damping C_i and relaxation parameter μ_i.

The expression of $G(t-\tau)$ is given as

$$G(t - \tau) = \sum_{i=1}^{n} C_i \, \mu_i \, e^{-\mu_i(t-\tau)} \tag{3.18}$$

The dynamic equation of motion of a discrete system with a damping kernel independent of instantaneous velocities is given by,

$$m\ddot{u} + \int_0^t G(t - \tau) \, \dot{u}(\tau) d\tau + ku = 0 \tag{3.19}$$

During each loading cycle of the viscoelastic material as shown in Figure 3.3, the amount of strain energy dissipated under deformation given by,

$$\Delta U = \oint \sigma(\varepsilon) d\varepsilon = \frac{1}{2} \int \{\epsilon_i\}^T [\psi] \{\sigma_i\} dV \qquad i=1, 2,\ldots 6 \tag{3.20}$$

Ψ is the specific damping capacity which is the measure of the amount of strain energy dissipated during the hysteretic stress cycle. The membrane and shear damping components of the specific damping capacity matrix is given by,

$$[\psi]_m = \begin{Bmatrix} \psi_1 & 0 & 0 \\ 0 & \psi_2 & 0 \\ 0 & 0 & \psi_{12} \end{Bmatrix} \qquad [\psi]_s = \begin{Bmatrix} \psi_{23} & 0 \\ 0 & \psi_{13} \end{Bmatrix} \tag{3.21}$$

The general expression of specific damping capacity and its relationship with the loss factor is given as,

$$\psi = \frac{\Delta U}{U_{max}} = 2\pi\eta \tag{3.22}$$

The maximum strain energy stored in each ply during the elastic deformation per each loading cycle which corresponds to the summation of strain energies along the fiber direction, transverse direction of the fiber and the shear direction is given by,

$$U_{max} = \frac{1}{2}\sigma_{max}\varepsilon_{max} \tag{3.23}$$

According to the classical damping theory of composite materials by Adams and Bacon, the specific damping coefficient of composite material laminate is given by (Adams and Bacon 1973),

$$\psi_{\text{Laminate}} = \frac{2 \sum_{k=1}^{n} \int_{h_{k-1}}^{h_k} \left(\delta(\Delta U_1) + \delta(\Delta U_2) + \delta(\Delta U_{12}) \right) dz}{\{N\}^T \{\varepsilon^0\} + \{M\}^T \{\kappa\}} \tag{3.24}$$

The equations of specific damping in each lamina in three directions are given by (Ni and Adams 1984)

$$\left.\begin{array}{l}
\psi_1 = \frac{8\psi_L}{C_{11}p^3} \sum_{k=1}^{p/2} m^2 \left(Q_{11}^k C_{11} + Q_{12}^k C_{12} + Q_{16}^k C_{16} \right) (m^2 C_{11} + mn C_{16}) W_k \\[3mm]
\psi_2 = \frac{8\psi_T}{C_{11}p^3} \sum_{k=1}^{p/2} n^2 \left(Q_{11}^k C_{11} + Q_{12}^k C_{12} + Q_{16}^k C_{16} \right) (n^2 C_{11} - mn C_{16}) W_k \\[3mm]
\psi_{12} = \frac{8\psi_{LT}}{C_{11}p^3} \sum_{k=1}^{p/2} mn \left(\begin{array}{c} Q_{11}^k C_{11} + \\ Q_{12}^k C_{12} + Q_{16}^k C_{16} \end{array} \right) (2mn C_{11} - (m^2 - n^2) C_{16}) W_k \\[3mm]
\psi_{\text{Laminate}} = \psi_1 + \psi_2 + \psi_{12}
\end{array}\right\} \tag{3.25}$$

Where 'p' is the number of plies, $m=\cos(\theta)_k$, $n=\sin(\theta)_k$ θ is the kth ply angle, W_k is the weighting factor based on the position of the kth lamina given as $k^3-(k-1)^3$.

The specific damping capacity of an arbitrary laminate under general loading based on the Saravanos and Chamis theory is given by (Billups 2008)

$$\psi_{\text{Laminate}} = \frac{\begin{Bmatrix} N \\ M \end{Bmatrix}^T \left(\begin{bmatrix} A^* & B^* \\ C^* & D^* \end{bmatrix} \right)^T \left(\begin{bmatrix} A^* & B^* \\ C^* & D^* \end{bmatrix} \right) \begin{bmatrix} A_D & B_D \\ B_D & D_D \end{bmatrix} \begin{Bmatrix} N \\ M \end{Bmatrix}}{\begin{Bmatrix} N \\ M \end{Bmatrix}^T \left(\begin{bmatrix} A^* & B^* \\ C^* & D^* \end{bmatrix} \right)^T \begin{Bmatrix} N \\ M \end{Bmatrix}} \tag{3.26}$$

A_D, B_D, C_D, D_D are components of stiffness matrix multiplied by damping coefficients.

3.3 Vibration Damping Estimation Formulations

There are different ways to measure damping in materials such as logarithmic decrement, viscous damping ratio (ξ), loss factor (η), Q factor, Energy ratio, etc., Damping in general can be measured using logarithmic decrement in time domain and half-power bandwidth in frequency domain.

The damping ratio obtained using the logarithmic decay of time history response curve over n-number of peaks is given by,

$$\xi = \frac{1}{n}\frac{2.303}{2\pi}\log_{10}\left(\frac{\text{Amplitude at Peak}-1}{\text{Amplitude at Peak}-n}\right) \tag{3.27}$$

Half power implies that kinetic energy at the bounding frequencies is half the peak energy based on the square of the amplitude ratio. Half power points are two frequencies on either side of the peak response at which the response amplitude is 1/N times (N>1) the peak amplitude Q. The loss factor measured using the half-power bandwidth is given by $\boldsymbol{\eta}$. Loss factor is used to quantify damping in viscoelastic materials by measuring the vibrating energy dissipated using various mechanisms.

$$\eta \cong 2\xi \cong \frac{1}{Q} \tag{3.28}$$

The simplified approximate relationship of loss factor with other units of damping measurements such as damping ratio ζ and damping quality factor Q^{-1} is given by,

$$\eta = Q^{-1} = \frac{\Delta\omega}{\omega_n} = \sqrt{\frac{1-\left[1-\frac{1}{2}\left(\frac{\Delta\omega}{\omega_n}\right)^2\right]^2}{N^2-1}} \tag{3.29}$$

For a case of N=2.5 which implies the amplitudes at the two bounding frequencies are 3.01 dB below the peak amplitude and η is small, then the above equation reduces to

$$\eta = \frac{\Delta\omega}{\omega_n} = 2\xi = Q^{-1} \tag{3.30}$$

The loss factor expressed in terms of Rayleigh's stiffness proportional damping as

$$\beta = \left[\frac{\eta}{\pi f_n}\right] \tag{3.31}$$

Where f_n is the natural frequency of vibration motion. The elastic modulus of a cantilever beam of mass m, length L, the moment of Inertia I, first natural frequency f_n, the mass of sensor used to measure the natural frequency M and material loss factor η can be estimated by (Botelho et al. 2006),

$$E = \frac{4\pi^2 f_n^2}{3I}\left[M + \frac{33}{140}m\right]L^3\left[1 + \frac{\eta^2}{4}\right] \tag{3.32}$$

3.4 Rotating Damping Formulations

For the modeling of internal damping in a rotating structure such as composite shaft, the coordinate systems in the stationary reference frame (OXYZ) and rotating reference frame (O′X′Y′Z′) are defined as shown Figure 3.5 (Ehrich 1992, Yuki et al. 2001, ANSYS 2001)
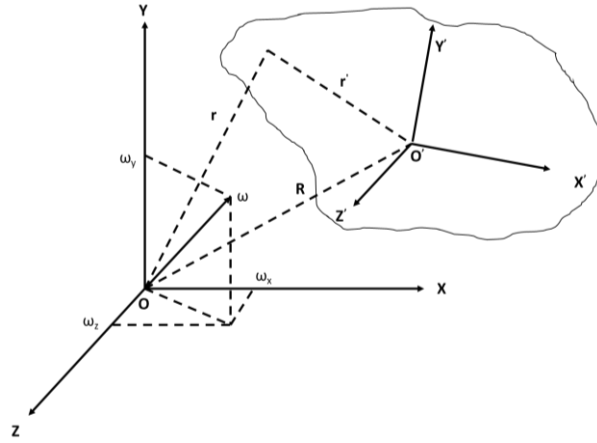
Figure 3.5.   The coordinate system in stationary and rotating reference frames

The displacement and velocity vectors in rotating reference frames are given by

$$\{r'\} = [R]\{r\} \qquad \{\dot{r}'\} = [R]\{\dot{r}\} + [R]\{\omega^T\} \tag{3.33}$$

where R is transformation matrix. Introducing equivalent viscous damping in the rotating shaft in the stationary reference frame, the rotating damping force is given by

$$\{F_d\} = [R]^T[C_{eq}][R]\{\dot{r}\} + [R]^T[C_{eq}][R][\omega^T]\{r\} \qquad \{F_d'\} = [C]\{\dot{r}'\} \tag{3.34}$$

The rotating internal damping matrix in the above expression is given by

$$[\Omega] = [C_{eq}][\omega^T] \qquad [\omega] = \begin{bmatrix} 0 & -\omega_x & \omega_z \\ \omega_x & 0 & -\omega_z \\ -\omega_z & \omega_z & 0 \end{bmatrix} \tag{3.35}$$

In the equation of motion of the rotating dynamic system, the rotating damping is included as

$$[M]\{\ddot{u}\} + ([C] + [C_{eq}] + [G])\{\dot{u}\} + ([\Omega] + [K])\{u\} = F(t) \tag{3.36}$$

39

Both the gyroscopic damping matrix [G] and the internal damping matrix [Ω] are proportional to the rotating velocity. The internal damping matrix [Ω] in the above equation causes a circulatory matrix modifying the apparent stiffness of the rotating structure leading to unstable motion. However, this unstable force can be effectively nullified by a large external damping force thus moving the threshold unstable speed ω* beyond the operating speed

$$\omega^* = 1 + \frac{[C]}{[C_{eq}]} \tag{3.37}$$

In a rotor-bearing system having external viscous external and hysteretic internal damping, the equivalent damping of the hysteretic damping is given by

$$[C_{eq}] = \frac{[K]\eta}{\omega_n} \tag{3.38}$$

3.5 Rotor Dynamic Formulations

By including the internal damping in the Timoshenko beam theory with the shear deformations and rotary inertia effects, the equation of motion of the isotropic shaft is given as (Goodwin 1989, Lalanne 1998, de Silva 2005, Chen and Gunter 2007)

$$\frac{\partial^2}{\partial x^2} EI \frac{\partial^2 q}{\partial x^2} + \frac{\partial^2}{\partial x^2} \left(E^* + \frac{\widetilde{E}}{\omega} \right) I \frac{\partial^2 q}{\partial t \, \partial x} + \frac{EI}{\kappa AG} \frac{\partial^2 q}{\partial t^2} = f(x, t) \tag{3.39}$$

Where E is the Young's modulus and G is the shear modulus of the material of the shaft, I is the moment of inertia, A is the area of cross-section, E* is the complex modulus, $\widetilde{E}$ is the loss modulus, κ is the shear coefficient of the section of the shaft and ω is the frequency of the external excitation f (x, t) in the case of steady forced vibrations.

The general form of the dynamic equation of motion of a rotating vibrating system is given as (Rao 1983, Vance 1988),

$$[M]\{\ddot{X}\} + ([G] + [C])\{\dot{X}\} + ([R] + [K])\{X\} = \{F\} \tag{3.40}$$

Where [M] is the global mass matrix, [K] is the stiffness matrix, [C], [G] are damping and gyroscopic matrices, and {F} is the external force vector in a stationary reference

frame. [R] is the rotating damping matrix due to the internal damping of the rotating shaft.

The above dynamic equation of motion can be solved using numerical methods. The finite element method is one of the popular numerical methods where global mass, stiffness, and damping matrices assembled to be broken down to a finite number of elemental matrices. In a normalized coordinate system of x from -1 to 1, the elemental mass at any layer linking to nodes i and j is given by,

$$[M_e] = \int_{-1}^{1} \int_{-1}^{1} \int_{-1}^{1} [N_i] \rho [N_j] \, dxdydz \tag{3.41}$$

Where [N] is the element shape function matrix at each node at i and j, ρ is the density of the material

Similarly, the elemental stiffness matrix is given by,

$$[K_e] = \int_{-1}^{1} \int_{-1}^{1} \int_{-1}^{1} [B]^T [\overline{D}][B] \, |J| dxdydz \tag{3.42}$$

where [B] is the element strain matrix, J is Jacobean matrix and $[\overline{D}]$ is the transformed material stiffness matrix equal to $[T]^{-1}[D][T]$, [T] is transformation matrix and [D] is the material stiffness matrix in the local coordinate system given as

$$[D] = \begin{bmatrix} D_{11} & D_{12} & 0 & 0 & 0 \\ D_{12} & D_{22} & 0 & 0 & 0 \\ 0 & 0 & \kappa G_{12} & 0 & 0 \\ 0 & 0 & 0 & \kappa G_{12} & 0 \\ 0 & 0 & 0 & 0 & G_{12} \end{bmatrix} \tag{3.43}$$

$$D_{11} = \frac{E_1}{1 - \vartheta_{12}\vartheta_{21}} \quad D_{12} = \frac{E_2 \vartheta_{12}}{1 - \vartheta_{12}\vartheta_{21}} \quad D_{22} = \frac{E_2}{1 - \vartheta_{12}\vartheta_{21}}$$

The isotropic bearing supports are modeled as Kelvin-Voigt model consisting of stiffness and viscous damping parameters. The external damping present in the rotor-bearing system in viscous damping form such as squeeze film damper can be represented in the form of a classical form of damping as Rayleigh damping proportional to the stiffness matrix. The hysteretic damping of viscoelastic materials is also approximately represented in the time domain as equivalent proportional damping.

The loss factor $'\eta'$, which represents the hysteretic damping is the ratio of the imaginary and real parts of the complex modulus. The external damping matrix is given by,

$$[C] = \sum_{j=1}^{b} \left(\alpha_j [M_j] + \left(\beta_j + \frac{\eta_j}{|\omega|} \right) [K_j] \right) \tag{3.44}$$

where α and β are proportional constants of mass and stiffness matrices respectively corresponding to 'b' number of bearing supports. Both forms of external damping can be incorporated in the external spring-damper elements as proportional damping. The mass proportion of the external damping is generally ignored as it is relevant to low-frequency dampers only.

The rotating damping matrix can be represented in the following form

$$[R] = [C_{rotor}][\omega^T] \tag{3.45}$$

The general dynamic response of the vibrating system is given by

$$\{u_i\} = \{\varphi_i\} e^{\bar{\lambda}_i t} \tag{3.46}$$

and the quadratic equation of Eigen solution is given by,

$$-\bar{\lambda}_i^2 [M]\{\varphi_i\} = [K]\{\varphi_i\} + \bar{\lambda}_i [C]\{\varphi_i\}$$

$$\bar{\lambda}_i = a_i + j b_i \qquad \delta_i = 2\pi \frac{a_i}{b_i} \qquad \zeta = \frac{-a_i}{\sqrt{a_i^2 + b_i^2}} \tag{3.47}$$

φ_i is the displacement vector and $\bar{\lambda}_i$ is the complex value at the mode i, a_i is a real part of eigenvalue representing the stability of the eigenproblem, b_i is the imaginary part of eigenvalue representing the frequency and j is $\sqrt{-1}$. The complex eigenvalues and eigenvectors are evaluated using the QR eigenvalue algorithm and inverse iterations. Further, the stability criteria such as Routh and Hurwitz may be used to evaluate the rotor dynamic instability. The ith eigenvalue will be stable if a_i is negative and unstable if a_i is positive.

The damping in the freely vibrating system can be measured using the logarithmic decrement, which is a function of modal damping ratio (ζ). The logarithmic decrement δ_i represents the logarithm of the ratio of two consecutive peaks in the dynamic

response, a positive value indicating the instability threshold. Alternatively, the modal damping ratio can also be used by ascertaining a positive value, the stability of the rotor-bearing system can be ensured.

Considering the first two rigid body translational and conical and the subsequent lateral flexural modes, the vibratory displacement at the center of the shaft due to external excitation such as rotating unbalance may be given as,

$$u(y,t) = u_r(t) + \left(z - \frac{l}{2}\right)\theta_r(t) + u_f(y,t)$$

$$u_r(t) = u_{ry} + iu_{rz} \qquad \theta_r(t) = \theta_{ry} + i\theta_{rz} \qquad u_f(t) = u_{fy} + iu_{fz} \qquad (3.48)$$

The relatively softer bearing supports in comparison to the stiffer rotating shaft will ensure the first two modes as rigid body modes. If the bearing supports tend to be stiffer then the rigid body modes turn up as the subsequent flexural modes where the shaft will undergo flexural displacement which is undesirable. At each mode, the strain energy ratio of the rotating shaft to the bearing supports is an index which indicates the type of displacement at the whirling motion of the shaft. The strain energy of each element can be represented as,

$$U_e = \frac{1}{2}\sum_{i=1}^{n}\{\sigma\}^T\{\epsilon\}V_i + \frac{1}{2}(\{u\}^T\{K_e\}\{u\}) \qquad (3.49)$$

$\{\sigma\}$ is the stress vector, $\{\epsilon\}$ is the elastic strain vector, n is the number of nodal integer points, V_i is the volume at each nodal integer i, $\{u\}$ is the element degree of freedom vector and $\{K_e\}$ is element stiffness matrix.

3.6 Model Updating of Damping

The frequency domain dynamic equation of motion of viscoelastic material is given by,

$$-\omega^2 m + j\omega G(\omega) + k = f(\omega) \qquad (3.50)$$

$$G(\omega) = \sum_{i=1}^{max}\frac{\mu_i}{\mu_i + j\omega}C_i \qquad (3.51)$$

The receptance frequency response matrix H is given by

$$H(\omega) = \frac{u(\omega)}{f(\omega)} = \frac{1}{k - \omega^2 m + \omega G(\omega)} \qquad (3.52)$$

In a special case when μ_i tends to infinite value, the equation of motion reduces to have viscous material damping represented by the damping matrix C in terms of the proportional mass M and stiffness K matrices damping constants α and β.

$$[C] = \alpha[M] + \beta[K] \tag{3.53}$$

Frequency response function in a free vibratory motion is given by

$$H_{ij}(\omega) = -\omega^2 \sum_{i=1}^{n} \frac{\emptyset_{im}\emptyset_{in}}{\omega_i - \omega + 2\zeta_i\omega\omega_i} \qquad \zeta_i = \frac{1}{2}\left(\frac{\alpha}{\omega_1} + \beta\omega_i\right) \tag{3.54}$$

The stationary time-domain linear equation of motion is given by,

$$[M]\{\ddot{u}\} + [C]\{\dot{u}\} + [K]\{u\} = \{f(t)\} \tag{3.55}$$

The frequency domain equation to determine eigenvalues and eigenvector is given by

$$[M]s^2 + [C]s + [K]\{\phi\} = \{0\} \quad s = j\omega - \sigma \tag{3.56}$$

$\{\Phi\}$ is an eigenvector, σ is damping decay constant. For a given set of modal frequencies and damping of n nodes n>=2

$$2\begin{Bmatrix} \sigma_1 \\ \vdots \\ \sigma_n \end{Bmatrix} = \begin{bmatrix} 1 & \Omega_1^2 \\ \vdots & \vdots \\ 1 & \Omega_n^2 \end{bmatrix} \begin{Bmatrix} \alpha \\ \beta \end{Bmatrix} \qquad \Omega^2 = \sigma^2 + \omega^2 \tag{3.57}$$

The modal Assurance factor (MAC) determines the difference between theoretical and experimental modes (Allemang and Brown 1982).

$$MAC = \frac{\left|[\emptyset_{nu}]^T[\emptyset_{exp}]\right|^2}{\left([\emptyset_{nu}]^T[\emptyset_{exp}]\right)\left([\emptyset_{nu}][\emptyset_{exp}]^T\right)} \tag{3.58}$$

The signature assurance criteria (SAC) correlates the numerical and experimental frequency response functions (Subhajit and Sushanta 2016),

$$SAC = \frac{\left(|H_{nu}||H_{exp}^T|\right)^2}{\left(|H_{exp}^T||H_{exp}|\right)\left(|H_{nu}^T||H_{nu}|\right)} \tag{3.59}$$

CHAPTER 4

4 MATERIALS AND METHODS

In this chapter, the details of finite elements, the analysis steps used in the numerical analysis and the experimental methodology followed in the thesis work are described.

4.1 Finite element modeling and analysis

The numerical rotor dynamic investigation was carried out using the finite element analysis tools. The general-purpose finite element analysis tools such as ANSYS was used for the three-dimensional rotor dynamic investigation of the composite material shaft application. The new generation finite elements of ANSYS such as BEAM188, SHELL281, and COMBIN214 were used in the rotor dynamic analysis carried out in this present work. The two finite elements of BEAM188 and SHELL281 of ANSYS were used to model the rotating elements. COMBIN214 was used to model the stationary bearing supports. BEAM188 is a finite strain linear, quadratic, or cubic two-node element of ANSYS based on the Timoshenko beam theory with the shear deformation. BEAM188 is suitable for analyzing the slender beams having a slenderness ratio of more than 30. Each node of the BEAM188 element has three translational and three rotational in X, Y, Z axes. One additional warping degree of freedom provides an option for the restrained or unrestrained warping of cross-sections. The geometrical representation of the BEAM188 element is shown in Figure 4.1.
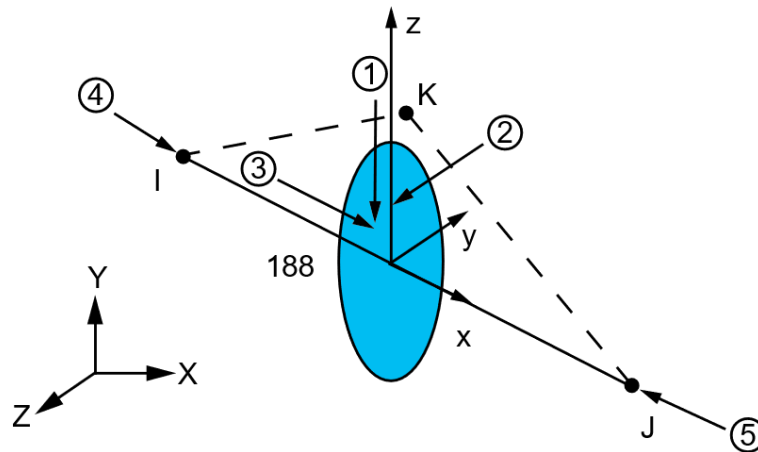
Figure 4.1.   Geometrical representation of beam 188

The layered ANSYS SHELL281 element shown in Figure 4.2 is suitable for modeling the composite shells which include the shear deformation effects in the transverse direction. It is governed by the Mindlin-Reissner shell theory which is a first-order shear deformation theory, an extension of Love's shell theory suitable for long slender shells. The SHELL281 element has got a total of eight nodes, each node is provided with a total of six degrees of freedom of three translational and three rotational degrees of freedom in X, Y, and Z directions.
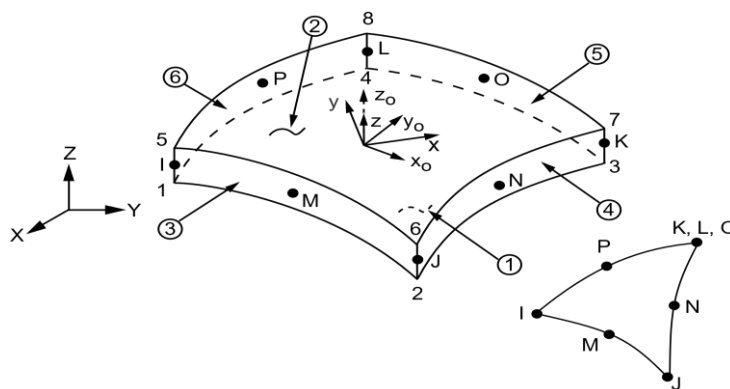
Figure 4.2.   Geometrical representation of Shell 281

COMBIN214, a 2-D spring damper bearing element as shown in Figure 4.3 is used for modeling bearing supports. The cross-coupling stiffness and damping coefficients are being ignored in this work as all the bearings are rolling element bearings.
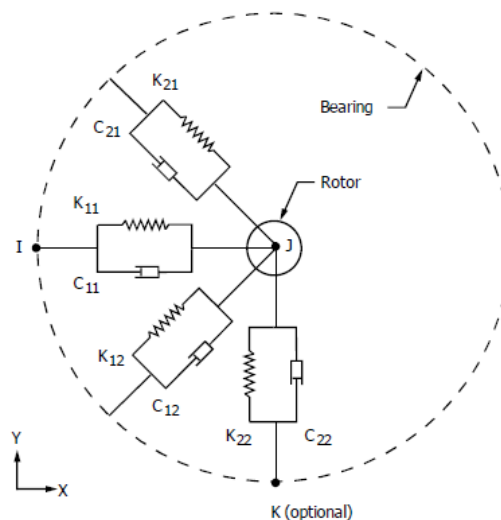
Figure 4.3.   Geometrical representation of COMBIN214 element

Along with the ANSYS which was used in most of the numerical analysis carried out in this work, DyRoBeS a rotor dynamic program based on the finite element method and MATLAB based rotor dynamic codes were also used. The finite beam element of DyRoBeS used for the lateral vibration analysis is described by two translational and two rotational degrees of freedom at each shaft station. The flexible bearing support element is described by the two translational degrees of freedom. The MATLAB based code is a combined finite element and transfer matrix code used for the analysis of bearing support characteristics and the stability analysis of rotor-bearing systems.

4.2 Case Studies of Previous Research

Three case studies covered in the literature survey were revisited to validate the modeling and analysis approach followed in the present thesis work. The critical speed analysis of a thin walled ten layered laminated composite helicopter tail rotor driveshaft analyzed by Zinberg and Symonds was carried out and compared with other works covered in the literature survey. Similarly, the RID models of Zorzi -Nelson and Genta and Amati were also revisited and compared.

4.2.1 Zinberg and Symonds Tail Rotor Shaft Analysis

The details of boron-epoxy composite material tail rotor shaft are given in Table 4.1 (Zinberg and Symonds 1976)

Table 4.1.   Geometric details of Zinberg & Symonds tail rotor shaft

Length	Mean radius	Thickness	Layer orientations
2470 mm	62.84 mm	1.321 mm	[90, 45, -45, 0_6, 90]

The critical speed analysis of the Zinberg composite tube using EMBT was carried out in ANSYS using the BEAM188 element. For the critical speed analysis using the EMBT method, the values of longitudinal Young's modulus of 142 GPa and shear modulus of 16.5 GPa were used as per Zinberg and Symonds analysis. For the shell modeling, each layer of the cylindrical shell was modeled using the SHELL281 element with the boron-epoxy with the values of longitudinal Young's modulus of 211 GPa and shear modulus of 24 GPa.

4.2.2 Zorzi-Nelson Rotating Damping Model

The simply supported steel shaft analyzed by Zorzi and Nelson was supported at both ends by two identical bearings. The details of the rotating beam model with internal damping are given in Table 4.2 (Zorzi and Nelson 1977).

Table 4.2.   Details of Zorzi & Nelson rotating shaft

Geometric Properties	Material Properties	Bearing stiffness
Length=1.27m Diameter = 0.1016m	E=210E9 Pa ρ = 7800 kg/m^3 μ=0.3 η_v=0.02, η_h=0.02	$K_{yy} = K_{zz}$ = 175E5 N/m $C_{yy} = C_{zz}$ = 1750 Ns/m

The rotating beam was evaluated using the ANSYS Beam188 element. The rotating shaft was discretized into five elements of equal length as per the original work. The viscous damping was applied as stiffness matrix multiplier (β) and hysteretic damping was applied as an equivalent viscous damping in terms of β damping.

4.2.3 Hollow Steel Shaft Supported on Two End Bearings

The details of the hollow steel shaft of which the ends are supported on two bearings (Genta and Amati 2010) are given in Table 4.3.

Table 4.3.   Details of the hollow rotating shaft

Geometric Properties	Material Properties	Bearing stiffness
Length=1.5m Diameter = 0.05m	E=211GPa ρ = 7860 kg/m^3 η=0.02	$K_{yy} = K_{zz}$ = 2E6 N/m $\eta_{yy} = \eta_{zz}$ = 0.06
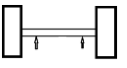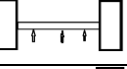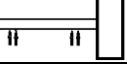
The analysis was carried out using the ANSYS BEAM188 element. The results were also verified using the DyRoBeS and MATLAB finite element code.

4.3 Composite Shaft Rotor-Bearing Systems

Three high-speed rotor-bearing system configurations of small to medium-small aero gas turbine industrial applications of steel material shafts were selected for the evaluation of application composite material shaft. These three rotor-bearing

configurations were selected based on the initial assessment of the possibility of improvements in the rotor dynamic behavior. The existing steel shaft rotor-bearing support systems of all the three configurations were optimized for all the design requirements. The geometrical details of the three rotor-bearing systems are as given in Table 4.4.

Table 4.4.   Rotor Shaft -Bearing System Configurations

Configuration		Shaft dia (mm)	Shaft length (mm)	Bearing span (mm)	Inertia (kgm^2)	Bearing stiffness (N/m)	Mass (kg)	Max Speed (rpm)
1		25	100 *(80)	60	0.001	2e7/3e7	7	55000
2		30	690 *(400)	450	0.06	1e7/5e7/ 1e7	12	30000
3		30	800 *(500)	560	0.1	5e7/5e7/ 1e7/5e7	20	23000

Note: * Length of composite shaft is given in brackets optimized to fit into the existing gas turbine engine layouts; the total shaft length remains the same as that of the existing metal shaft along with bearing supports location and other details.

The first configuration is a gas generator rotor-bearing system (GGRBS) of an auxiliary power system and a starter engine of a transport aircraft. The gas generator rotor system comprising of a single-stage centrifugal compressor and two-stage axial turbines is supported on two rolling element bearings. The second configuration is a low-pressure rotor-bearing system (LPRBS) of a small turbofan engine. It is supported at the ends on two rolling element bearings of flexible supports provided with squeeze film damping. The additional third bearing was proposed to increase the stiffness of the long slender shaft as it passes through the high-pressure spool. The third configuration is a power turbine rotor-bearing system (PTRBS) of a turboshaft engine supported on two-end bearing supports. Two bearings of the left support are housed in rigid supports and of the two bearings of the rear support on the overhang turbine side, one is housed in a flexible support and the other in rigid support. The power turbine shaft is also a slender shaft as it passes through gas generator spool and requires expensive high-speed balancing due to its flexibility at high speeds while passing through a flexure mode.

The rotor dynamic analysis was carried out using SHELL281, BEAM188, and COMBIN214 elements of ANSYS software for modeling the shaft, bladed rotor discs, and bearing supports respectively. The bladed discs were modeled using the BEAM188 element in terms of mass, transverse inertia, and rotary inertia along with the center of gravity equal to the actual values. The finite element models of the three rotor-bearing systems are shown in Figure 4.4, Figure 4.5, and Figure 4.6.
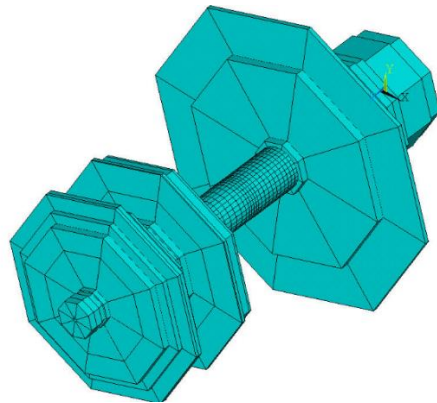
Figure 4.4.   Finite element model of GG rotor-bearing system
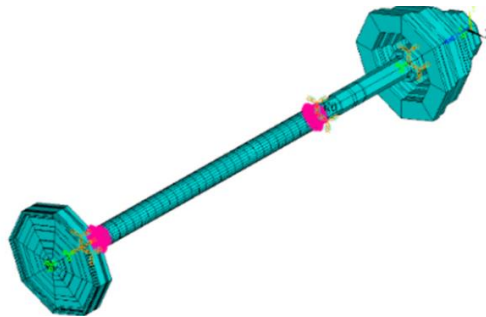
Figure 4.5.   Finite element model of LP rotor-bearing system
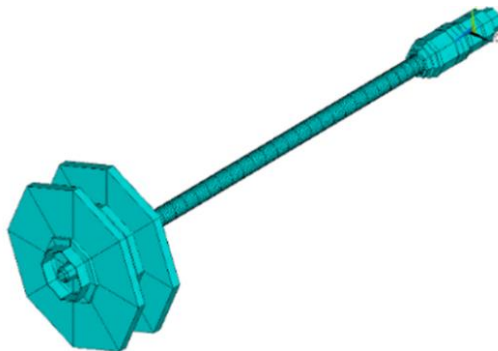
Figure 4.6.   Finite element model of PT rotor-bearing system

4.3.1 Preliminary Modal Analysis

The modal analysis was carried out as a preliminary investigation to verify the viability of using the composite material shaft. The composite tubular shaft of 5 mm wall thickness was arrived based on the basic approximate strength calculations to withstand the general operating requirements. The layer orientation of [90, 45, -45, 0_6, 90] was selected based on the previous research works (Zinberg 1970; Chang et al. 2004a). The analysis was carried out using the four composite materials of glass-epoxy, graphite-epoxy, carbon-epoxy, and boron-epoxy materials. The material properties of these materials are given in Table 4.5. The modal frequency values of the first three lateral modes of the rotor-bearing systems were evaluated and compared with the existing steel material shaft values. The rotor-bearing system found to have no advantage with the composite material shaft was eliminated from further analysis.

Table 4.5.   Material Properties

Sl. No	Property	unit	Steel	Glass/ Epoxy	Graphite/ Epoxy	Carbon/ Epoxy	Boron/ Epoxy
1	E_1	GPa	210	50	139	177.0	211
2	E_2	GPa		12	11	7.0	24.1
3	μ_{12}	-	0.3	0.2	0.313	0.3	0.36
4	G_{12}	GPa	84	5.6	6.06	5.8	6.9
5	G_{23}	GPa		5.6	3.78	5.8	6.9
6	Density, ρ	kg/m^3	7830	2000	1578	1600	1965
7	Tensile strength, S_1	MPa	950	490	880	870	1500
8	Shear Strength, S_{12}	MPa	450	70	97	35	110
9	Shear Strength, S_{23}	MPa	-	15	15	15	15

4.3.2 Parametric Analysis

A parametric study was carried out on the selected rotor-bearing systems. The modal analysis and the torsional stress analysis were carried out to select the best shaft configuration by parametrically varying the number of layers, layer sequences, and the layer thickness on the four composite material compositions given in Table 4.5. As found in the preliminary modal analysis, the modal frequency values of the first three lateral modes of the rotor-bearing systems were evaluated and compared with the existing steel shaft values. The torsional stress analysis was carried out to evaluate the

composite shaft strength due to the power transmitted by the shaft generated by the turbines mounted on the shaft. The maximum operational torque was applied at one end of the shaft and the other end was fixed as shown in Figure 4.7. The composite shaft was modeled using the ANSYS SHELL281 element.
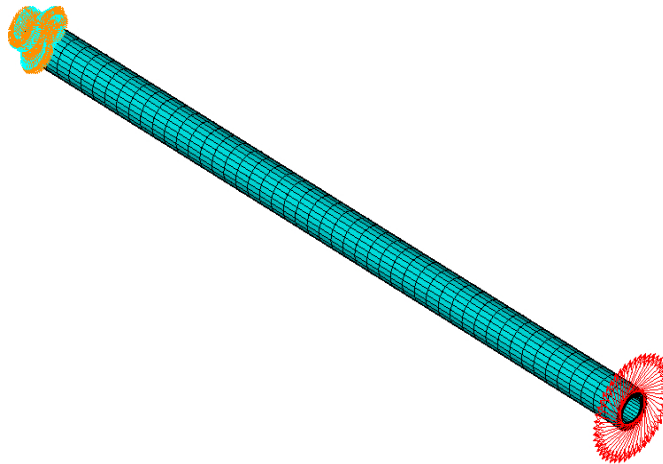
Figure 4.7.   FE Model of the composite shaft subjected torsional load

4.3.3 Critical Speed Analysis

The critical speed evaluation was carried out using the Campbell diagram which graphically represents the whirling speeds of the rotor-bearing system. In a generic Campbell diagram applied to any rotating system or a component, the natural frequencies are plotted against the rotational speed and the critical speeds are identified where the excitation lines intersect the natural frequency lines.

In the Campbell diagram of lateral vibration of a rotor-bearing system, due to the gyroscopic damping effect of the rotary inertia of the rotating discs mounted on the shaft, each lateral mode is split into two diverging components. The frequency component which increases as the speed increased is the forward whirl mode and the component which decreases as the speed is increased is the backward whirl mode. In the forward whirl mode, the shaft whirls in the same direction of rotation whereas in the backward whirl mode the shaft whirls in the opposite direction to the rotation. The point of intersection of forward and backward modes with the line of the first-order excitation is identified as the lateral critical speed.

In a conventional sub-critical design approach, the lateral critical speeds were kept away from the operating speeds with sufficient separation margins. As the rotating machines were evolved over the years, many super-critical rotating machines with the critical speeds placed close to the operating speeds were commissioned. However, the operation of the super-critical rotating machine is not always smooth as the excessive vibration at the critical speed can be detrimental to the safety of the rotating machine. These machines will be under continuous vibration health monitoring and to be immediately shut down even for a slight increase in the vibration levels. The frequent shutdowns not only cause reliability issues but also increase the total life cycle cost.

Identifying the critical speeds of the rotor-bearing system using the Campbell diagram is an important step in the present work. The rotor-bearing system for which the use of composite shaft can eliminate the supercritical operation is to be selected for further analysis.

4.3.4 Stability Analysis

Similar to the Campbell diagram, the stability analysis was carried out by using the stability map which graphically represents the logarithmic decrement value at the speed of rotation. Mathematically, as given in equation (3.47) in section 3.5, the real part of the complex eigenvalue at each mode represents the stability of the rotor-bearing system. As brought out in section 3.5, the negative real part represents the stability of the rotor-bearing system. Initially, the rotor dynamic stability analysis was carried out considering the rotating internal damping. The internal damping in the existing rotor-bearing system is primarily due to the coupling arrangement employed to join the turbine rotors. A set of known equivalent viscous damping coefficients due to the frictional joints of rotors were considered to evaluate the dynamic behavior due to rotating damping. Stability analysis was also carried out for an assumed range of rotating damping due to the composite material shaft. The stability threshold was determined by plotting the logarithmic decrement values of the rotor-bearing system at each lateral mode in both forward and backward whirl modes versus the rotational speed. For the rotor-bearing system to be rotor dynamically stable, the logarithmic

value shall be negative. When the logarithmic decrement of each lateral mode changes its sign from negative to positive, it indicates that the initiation of instability at the threshold speed of instability.

4.3.5 Unbalance Response Analysis

The unbalance response analysis was carried out to evaluate the vibration response of the composite shaft rotor-bearing system due to the residual unbalance of the rotating assembly. The displacement and bending stresses due to the residual unbalance at the operating speeds were compared with the values of the existing shaft configuration.

4.4 Hybrid Composite Shaft

The hybrid composite material tubular shaft comprised of laminated fiber-reinforced polymer matrix composite layers sandwiched between the steel tubes is shown in Figure 4.8. Though aluminium can be used in the inside surface of composite hollow shaft, only steel tube was selected considering the harsh environment of gas turbine engines.
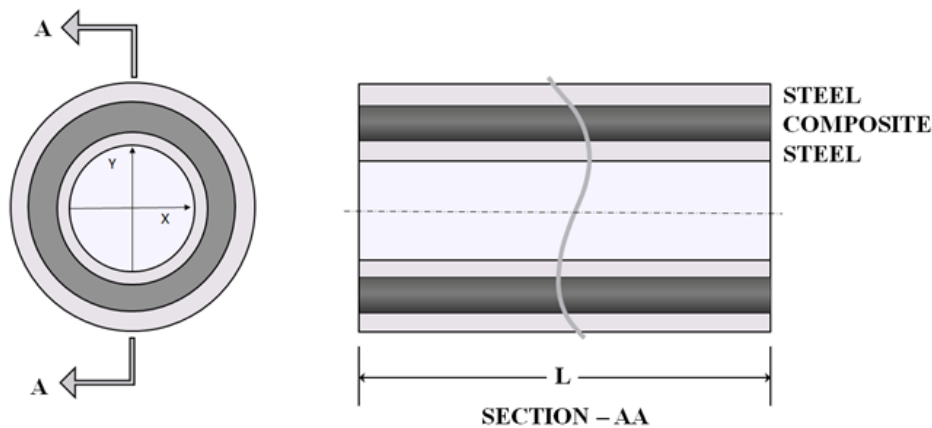
Figure 4.8.   Hybrid composite material shaft

In addition to the rotating shaft, the stationary bearing support system as shown in Figure 4.9 was also considered for the hybrid material application. The bearing support system consists of a flexible bearing housing made of steel alloy to house the bearings of high-speed rotor-bearing system, aluminium bearing housing support and the outer

casing made of steel alloy. The material properties are as given in Table 4.6. The bearing housing support is being envisaged as the other possible application for the hybrid material due to its natural frequency of 690 Hz close to the operating range of the rotating system. The use of hybrid composite material would increase this natural frequency beyond the operating speed of its rotating system.
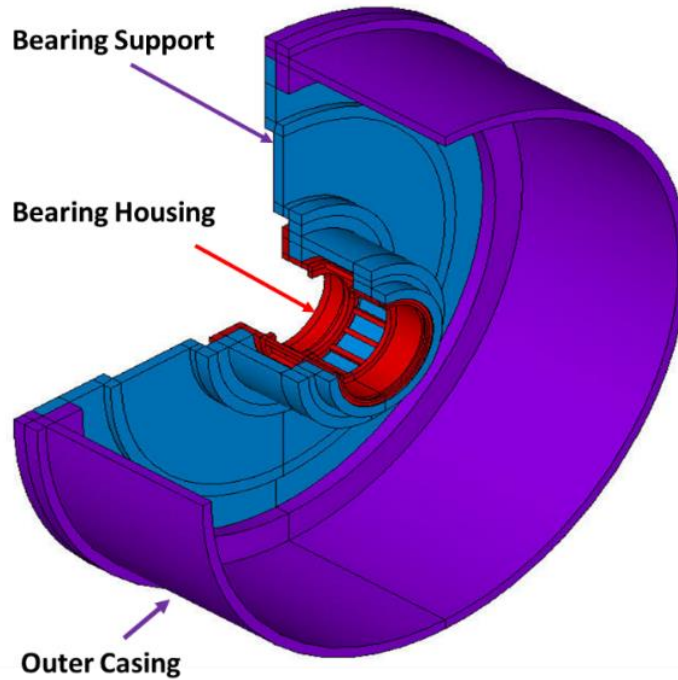
Figure 4.9.   The cut section of the supporting structure

Table 4.6.   Material properties for bearing support

Sl. No.	Property	unit	Steel	Aluminium	Graphite/ Epoxy	Carbon/ Epoxy
1	E_1	GPa	210	69	139	177.0
2	E_2	GPa			11	7.0
3	μ_{12}	-	0.3	0.28	0.313	0.3
4	G_{12}	GPa	84	28	6.06	5.8
5	G_{23}	GPa			3.78	5.8
6	Density	kg/m^3	7830	2600	1578	1600
7	Tensile strength, S_1	MPa	950	340	880	870
8	Shear Strength, S_{12}	MPa	450	210	97	35

The finite element model of the hybrid material shaft is shown in Figure 4.10. The finite element model of hybrid composite material bearing housing is shown in Figure 4.11.
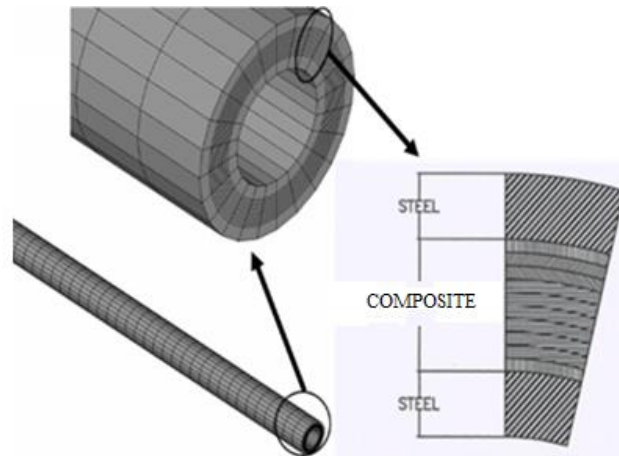
Figure 4.10.   Finite element meshing of hybrid composite material shaft
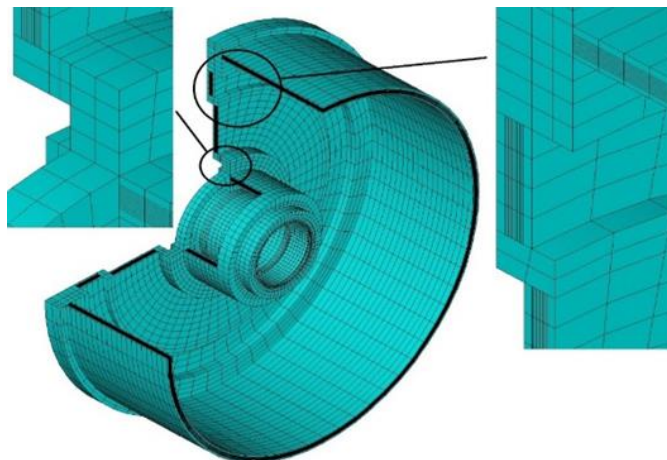
Figure 4.11.   Finite element model of hybrid composite bearing support

4.5 Experimental Characterization

The procedure and other details of mechanical and dynamic characterization tests carried out are presented in this section. The details of the material preparation, manufacturing, and test procedures along with the standards followed are explained in the following sections.

4.5.1 Material Preparation

For the balanced material properties of good quality, reliability, and easy availability, the T300 graphite/carbon fiber material was selected. T300 is a standard carbon fiber of tow size of 3K woven in a 4x4 V-twill weave. The aerospace quality LY 556 epoxy resin was used as a matrix element. A mixing rule of 60% for the fiber and 40% for the matrix is considered as per the manufacturing process followed in fabricating the composite material laminates. The material properties of the composite lamina evaluated for the carbon-epoxy laminate of T300 fiber (MIL-HDBK-17-2F 1999) and LY556 matrix (Hinton et al. 2004) is tabulated in Table 4.7.

Table 4.7.   Material properties of Fiber, Matrix, and Lamina

Sl No.	Material Properties	Unit	T300	LY 556	Composite
1	Young's Modulus, E_1	MPa	2.3E+05	3.35E+03	1.34E+05
2	Young's Modulus, E_2	MPa	1.50E+04	3.35E+03	7.00E+03
3	Young's Modulus, E_3	MPa	-	-	7.00E+03
4	Shear Modulus, G_{12}	MPa	1.50E+04	1.24E+03	5.80E+03
5	Shear Modulus, G_{23}	MPa	7.00E+03	-	5.80E+03
6	Shear Modulus, G_{31}	MPa	-	-	5.80E+03
7	Poisson's ratio, υ_{12}	-	2.00E-01	3.50E-01	2.80E-02
8	Poisson's ratio, υ_{23}	-	2.00E-01	3.50E-01	2.80E-02
9	Poisson's ratio, υ_{31}	-	-	-	4.0E-01
10	Tensile Strength, $+S_1$	MPa	3.53E+03	8.00E+01	1.94E+03
11	Compressive Strength, $-S_1$	MPa	-2.18E+03	-1.20E+02	-1.2E+03
12	Tensile Strength, $+S_2$	MPa	-	-	6.81E+01
13	Compressive Strength, $-S_2$	MPa	-	-	-1.02E+02
14	Density	g/m^3	1.76E+06	1.27E+06	1.6E+06

The carbon-epoxy plate/beam test samples were fabricated using the hand layup technique. The composite material laminate was made up of 3K woven carbon fiber fabric (T300) cut as per the predetermined laminate orientation angle and stacked up with a 40% volume fraction of aerospace grade epoxy resin (LY 556). The laminated carbon/epoxy part was then kept inside the vacuum bag for the removal of voids and excessive resin content if any as shown in Figure 4.12. The test samples were cured up to 120°C temperature in a heating furnace for about an hour.

Figure 4.12.   Fabrication of composite material laminate

The Steel (or Aluminium) sheets were then bonded with the cured carbon/epoxy laminates using the adhesive to form the hybrid composite. The sample analysis of steel and aluminium test samples was carried out using the Thermo Scientific ARL 3460 OES Spectrometer metal analyzer. The material composition of steel and aluminium samples from the sample analysis are given in Table 4.8 and Table 4.9 respectively. The mechanical strength properties of steel (AMS 5604) and aluminium (AMS 4708) used in the test samples are given in Table 4.10.

Table 4.8.   Steel (AMS 5604) sample analysis

Sl. No.	Contents	Reference range (%)	Test result (%)
1	Chromium (C)	15.0-17.5	15.3910
2	Manganese (Mn)	1.0 max	0.9222
3	Nickel (Ni)	3.0-5.0 max	3.4477
4	Copper (Cu)	3.0-5.0 max	3.1685
4	Silicon (Si)	1.0 max	0.3785
5	Carbon (C)	0.05-0.0.07	0.0551
6	Others	1.0 max	0.9218
7	Ferrous (Fe)	remaining	75.7152

Table 4.9.   Aluminium (AMS 4078) sample analysis

Sl. No.	Contents	Reference range (%)	Test result (%)
1	Zink (Zn)	5.10-6.10	5.3430
2	Magnesium (Mg)	2.10-2.90	2.6540
3	Copper (Cu)	1.20-2.00	1.4122
4	Chromium (C)	0.18-0.28	0.1925
5	Silicon (Si)	0.00-0.4	0.2510
6	Manganese (Mn)	0.30 max	0.2180
7	Others	0.15 max	0.1240
8	Aluminium (Al)	remaining	89.8053

Table 4.10.   Material properties of steel and aluminum

Sl. No.	Material Properties	Unit	Steel	Aluminum
1	Young's Modulus, E	MPa	2.0E+05	6.9E+04
2	Shear Modulus, G	MPa	8.0E+04	2.8E+04
3	Tensile Strength	MPa	1034	570
4	Yield Strength	MPa	931	500
5	Shear Strength	MPa	620	330
6	Brinell Hardness	MPa	320	150
7	Density	g/m^3	7.80E+06	2.76E+06

AW 106 resin/Hardener HV 953U epoxy adhesive used in the hybrid samples is made of AW 106 resin mixed with an equal amount by volume of HV953U hardener. As per the technical documentation from the supplier, AW 106/HV 953U epoxy adhesive is a viscous material suitable for bonding a variety of materials including composite materials and metals. The adhesive is electrically insulating which can be easily applied either manually by spatula and a stiff brush or mechanically with meter/mix and coating equipment. The AW 106/HV 953U epoxy adhesive cures at temperatures from 20ºC to 180ºC without releasing any volatile constituents. The curing duration reduces as the curing temperature increases. As per the manufacturer catalogue, the standard curing time is 15 hours at room temperature of 20ºC and 5 minutes at 150ºC. The technical details of the adhesive is given in Table 4.11. The test coupons of each test specimen were cut to the required dimensions using water jet cutting. Before carrying out the test, each test coupon was cured at 120°C for four hours in a heating furnace and brought back to room temperature by placing them at room temperature for about a week.

Table 4.11.   Technical details of Adhesive AW 106/HV 953U

Sl. No.	Contents	Unit	Test result	Test standard
1	Viscosity (25ºC)	cP	45000	ASTM D2393
2	Lap shear strength (25ºC)	MPa	17.6	ASTM D1002
3	Lap shear strength (100ºC)	MPa	22.5	
4	Fatigue strength (100ºC) with 50% static shear strength	Cycles	10^3-10^4	
5	Ultimate Tensile strength	MPa	33	ASTM D638
6	Glass Transition temperature, T_g	ºC	63	ASTM D4065
7	Shore Hardness	D	80	ASTM D2240

The composite shaft fabrication setup is shown in Figure 4.13. The setup consists of a two-piece die arrangement which was rigidly held using multiple clamps.

Figure 4.13.   Two-piece Die arrangement of Composite shaft fabrication

The fabrication process of the composite shaft involved many iterations to get the proper finish. Similar to the beam laminate fabrication, the T300 carbon fabric was cut as per the required layer orientation in the required sequence and wound on the mandrel. The vacuum-controlled smooth supply of epoxy was ensured to eliminate the laminate defects. The two-piece top and bottom parts of the die along with the fabricated composite tube is shown in Figure 4.14.

(a)

(b)

Figure 4.14.   (a) Top and bottom die (b) Composite tube

For the hybrid composite tubular shaft shown in Figure 4.15, the composite material tube was bonded to the inner and outer steel tubes using the AW adhesive. The

composite tube was precisely ground to maintain a uniform clearance with the inner and outer steel tubes. The insertion of the composite tube into the outer steel tube was precisely controlled. The steel tube was held by a stationary three-jaw chuck maintained within 20 microns radially. The composite tube applied with a uniform coat of adhesive on the outer surface was also held within 20 microns radially by a moveable carriage while inserting inside the steel tube.

Figure 4.15.   Hybrid composite shaft fabricated

4.5.2 Mechanical Characterization

As flexure and tension are the dominant loadings for both the rotating shaft as well as the supporting structure in lateral vibration modes, the test coupons were subjected to tension and flexural tests. Since the material under study includes the composite material and the combination of the metal with carbon-reinforced polymer matrix composite and sandwich-type, the various ASTM standards of polymer composite, metal, sandwich materials, etc., were studied.

The Shimadzu AGX plus universal testing machine of 100 kN capacity shown in Figure 4.16 was used to carry out the tensile and flexural tests by conforming to the testing requirements stipulated by the governing ASTM test standards.

Figure 4.16.   Shimadzu AGX plus universal testing machine

For the tensile test, ASTM D3039/D3039M standard was referred. The test methods of metal and sandwich laminate such as ASTM E8/E8M-16a were also referred. For the tensile test, tabbed test specimens of dimensions of 25 mm width and 250 mm length were used. For the three-point flexural test, ASTM D790-17 and ASTM D1184-98 standards were referred. For the 3-point flexural test, the test specimens of dimensions of 13 mm width and 180 mm length were used. The test coupons as per the dimensions were cut to sizes using water jet cutting.

4.5.3 Dynamic Characterization

The dynamic characterization testing was performed for evaluating the material damping present in the viscoelastic composite material proposed for the rotor-bearing support application. Damping is the behavior of a material or the system resulting in dissipation of energy when subjected to vibratory motion. The dislocation motion of atoms is responsible for the material damping in metals whereas in polymers it is the chain motion of atoms that generates the material damping.

The Dynamic characterization tests carried out in this work comprised of the free vibration test and Dynamic mechanical analysis (DMA). The free vibration tests were carried out using the beam and tube samples. All the carbon-epoxy and hybrid composite material laminates fabricated as per the procedure given in section 4.5.1 were used as the beam samples of sizes as per the ASTM damping estimation standard (ASTM D756–05 2017) to obtain the natural frequencies of interest of this work.

DMA testing of all the carbon-epoxy and hybrid laminates were also carried out on beam sample of sizes as per the DMA facility requirement. Based on the test results of modal testing and DMA of beam samples, tubular sample from the best material configuration of was fabricated and modal damping test was carried out. In addition to the damping estimation, the dynamic characterization test results were used to estimate the material stiffness values to substantiate the material selection. For the free vibration testing of composite and hybrid shafts, the tubular samples were fabricated from the most suitable material based on the characterization results of the beam samples.

4.5.3.1   Damping Estimation by Free Vibration

The schematic representation for the experimental free vibration testing setup shown in Figure 4.17 comprises a mounting frame to rigidly hold the test specimen, an impact hammer exciter, response signal measurement transducers such as piezoelectric accelerometers and the vibration data recorder with the analyzer. The testing hardware is equipped with an inbuilt signal conditioner, antialiasing filters, etc.,
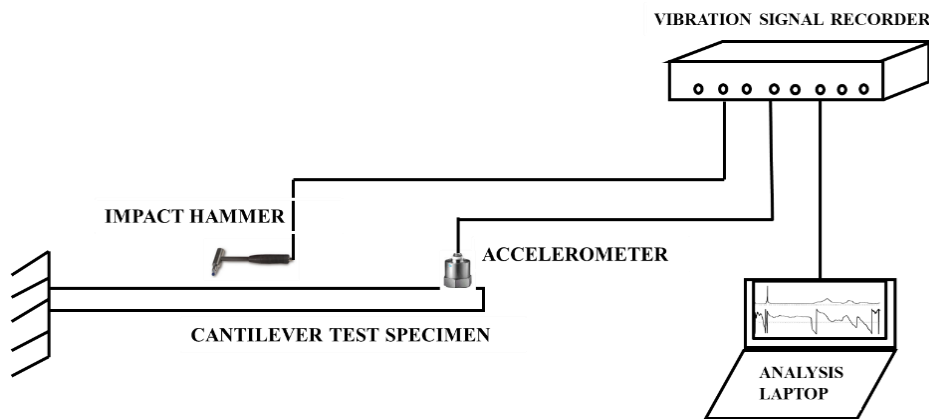
Figure 4.17.   Schematic representation of free vibration test setup

The test specimen was rigidly fixed to the mounting fixture as a cantilever beam as shown in Figure 4.18. The first two lateral mode shapes of the cantilever beam specimen where the damping was estimated are shown in Figure 4.19.
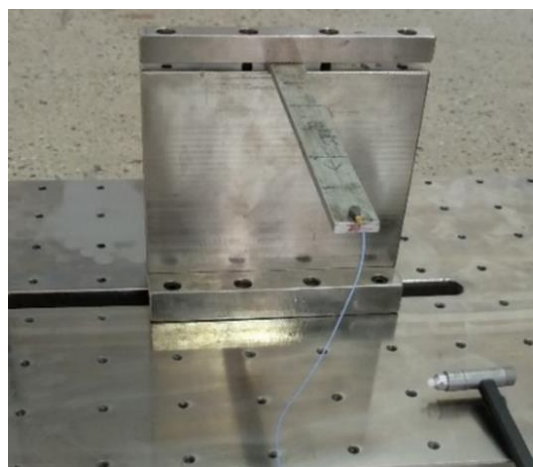
Figure 4.18.   Experimental damping measurement setup of beam specimen
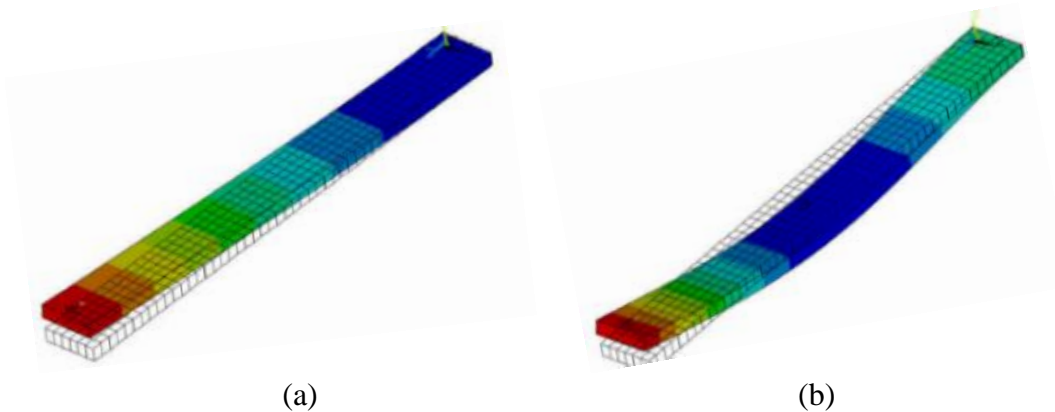
<center>(a)   (b)</center>

<center>Figure 4.19.   Cantilever beam (a) I Mode shape (b) II Mode shape</center>

The vibration response was measured from the test specimen due to the impacts imparted on the test specimen using the impact hammer having the impact force range of ±500 lbf (pk-pk) with 10 mV/lbf sensitivity. The response from the vibrating beam was measured by a miniature accelerometer of mass 0.6 grams glued close to the free end of the test specimen and acquired using the 8 channel Spider S80 vibration data analyzer as shown in Figure 4.20. Spider S80 is capable of acquiring the data at the sampling rate of 102.4 kHz.

<center>Figure 4.20.   Instrumentation used in damping measurement</center>

The test specimen response was averaged for a minimum of five intermittent impacts to obtain a clear force response function. The damping coefficient of each test specimen was derived using half-power bandwidth method and logarithmic decay. The half-power bandwidth also known as 3-dB power bandwidth method uses the frequency

<center>64</center>

response function plot and the logarithmic decay is evaluated from the consecutive peaks of the time signal response using the mathematical formulations given in section 3.3. Similar to an eigensolution, FRF can be expressed as a complex function of real and imaginary parts comprising of the amplitude which is a ratio of the input force to the response such as g/N and the phase angle of input and output response signals. The coherence function was used to validate the relevance and quality of the response to the input. To verify that the response peeks considered were indeed of the first two lateral modes, each test coupon was divided into five equal zones and keeping the accelerometer fixed at the free end, the test specimen was excited at each of the five zones starting from the fixed end to the free end.

The damping estimation of the tubular specimen was carried out using a portable setup as shown in Figure 4.21. One end of the tubular test specimen was rigidly fixed on a large machine foundation to eliminate the support flexibilities and the triaxial accelerometer was mounted at the free end to record the vibration response in both lateral directions. The damping estimation test was carried out for the steel, composite, and hybrid composite material tubes similar to the damping estimation of beam specimens as shown in Figure 4.22. The first two natural frequencies shown in Figure 4.23 were numerically estimated to select the right frequency for the damping estimation. For both beam and tubular specimen, the sampling frequency of 1200 Hz was selected by considering the first two lateral frequencies of interest.

Figure 4.21.   Portable experimental damping estimation setup

Figure 4.22.   Tubular test specimen (steel, composite and hybrid)
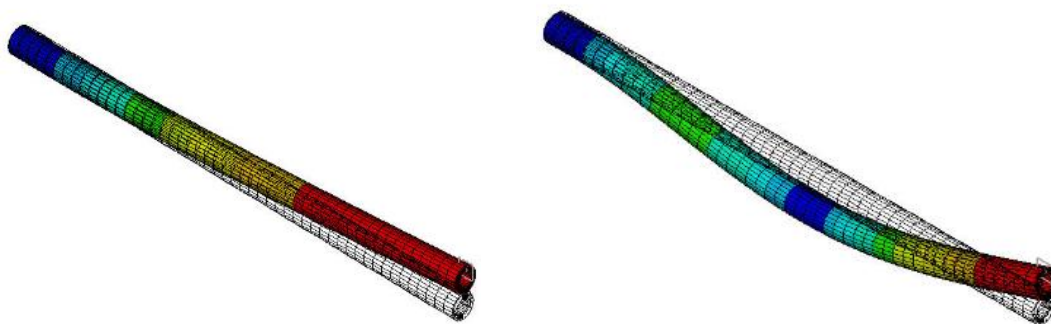
(a)   (b)
Figure 4.23.   Cantilever tube (a) I Mode shape (B) II Mode shape

4.5.3.2   Dynamic Mechanical Analysis

Dynamic Mechanical Analysis provides an accurate measure of material stiffness in terms of storage modulus and material damping in terms of loss modulus. The complex storage and loss modulus which measure the stiffness and damping characteristics of viscoelastic materials vary to the change in operating temperature. Dynamic Mechanical Analysis measures the glass transition temperatures, secondary transitions, and other variations caused by the manufacturing processes, cold crystallization, cure optimization, filler effects, etc., in the viscoelastic materials.   Depending on the molecular compositions designated by the glass transition temperature (T_g), the molecular bonding in viscoelastic materials change. At the softening temperature at the end of the glassy region and the beginning of the transition region, the viscoelastic material begins to soften as the storage modulus reduces and the loss modulus increases till the material attains its transition temperature as shown in Figure 4.24 (David 2001).
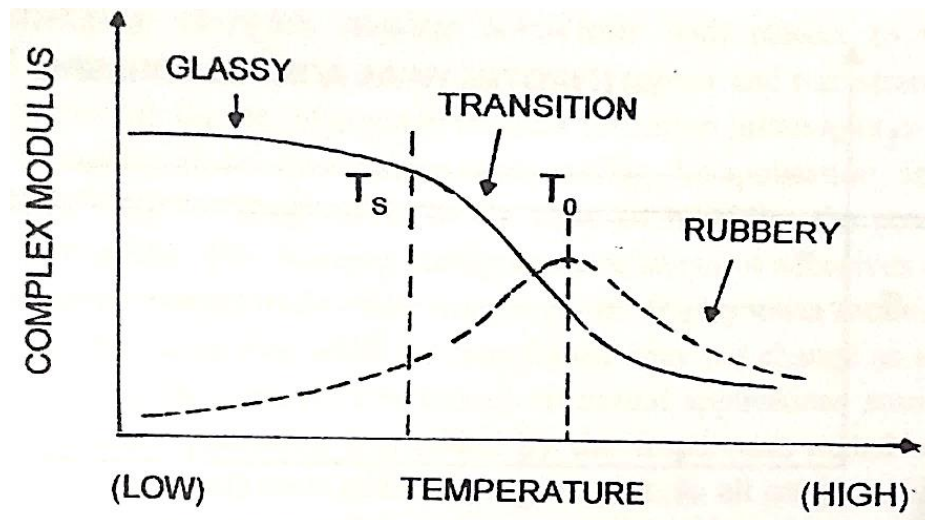
(a)
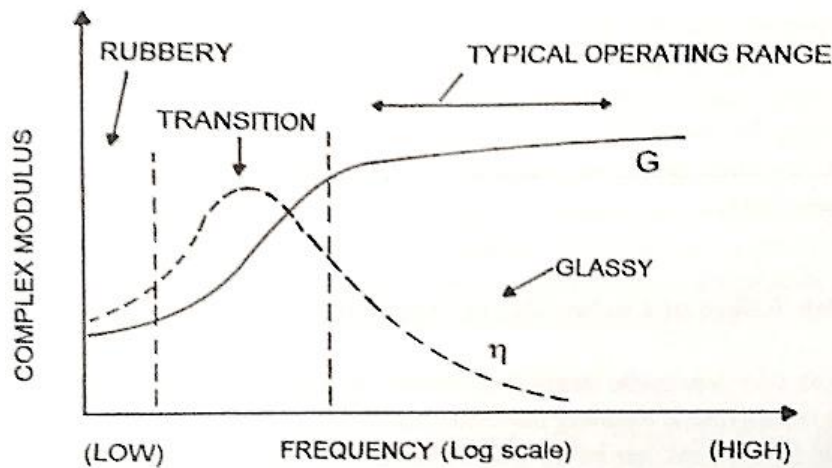
(b)

Figure 4.24.   Effect of (a) Temperature (b) Frequency on Viscoelastic material

Beyond the transition temperature, the loss modulus reduces and settles down to a steady value as it enters the rubbery region. Similar to the influence of temperature variations, frequency variation also affects the behavior of viscoelastic materials but in the reverse order. DMA uses either the transient or dynamic oscillatory tests to measure the viscoelastic properties. In a dynamic oscillatory test, a sinusoidal strain is measured for the sinusoidal stress applied on the material. The phase difference between the stress and strain determines the elastic and viscous nature of the material. For a purely elastic material, the phase lag is 0^0 and for a purely viscous material, the phase lag is 90^0 .

TA Q800 Dynamic mechanical analyzer, a sixth-generation dynamic mechanical analyzer shown in Figure 4.25 was used to carry out damping testing of test coupons in double cantilever mode in a stationary frame of reference. TA Q800 utilizes the non-contact, linear drive motor technology to provide precise control of the stress. The strain is measured using an optical encoder technology that provides precise sensitivity and resolution. The low friction air bearings used by the TA Q800 analyzer provide better performance compared to the traditional designs that employ LVDT technology, stepper motors, and mechanical springs.

The dynamic mechanical analysis was carried out in a stationary frame of reference in dual cantilever mode, samples are clamped at both ends and fixed at the center as shown in Figure 4.25.
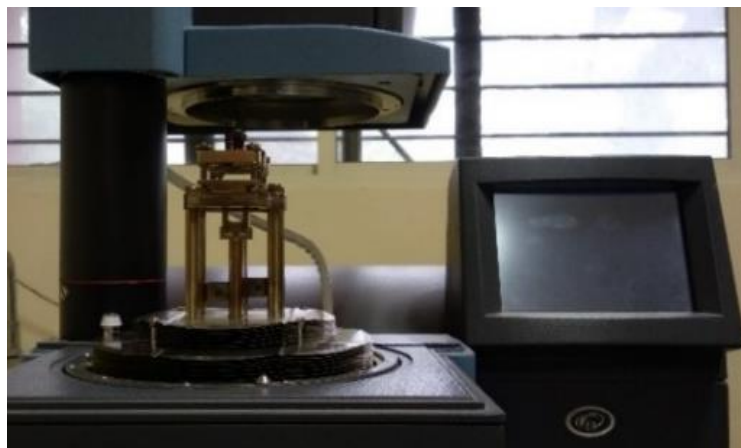
(a)

(b)

Figure 4.25.   (a) TA Q800 DMA Analyzer (b) Test coupon in dual cantilever mode

CHAPTER 5

5 RESULTS AND DISCUSSIONS

In this chapter, the results from the finite element analysis and experimental tests carried out as per the procedures laid down in the previous chapter are presented and discussed. The rotor dynamic analysis of composite shaft rotor-bearing systems, including the hybrid composite material shaft, are presented here. The test results of mechanical and dynamic characterization tests are presented and discussed in detail.

5.1 Case Studies of Previous Research

The analysis results from the three case studies of previous research works (Zinberg and Symonds 1970; Zorzi and Nelson 1976; Genta and Amati 2010) as per the procedure given in sections 4.2.1 to 4.2.3 are presented in the following sections.

5.1.1 Zinberg-Symonds Tail Rotor Shaft Analysis

The critical speed value of the Zinberg shaft obtained in this work using the beam model (EMBT) is 5724 rpm and using the shell element (SHELL281) is 5732 rpm. The critical speed values obtained in the present work are compared with the values of the original investigator and the other investigators using the various formulations as explained in the literature review are tabulated in Table 5.1. The critical speed value obtained using EMBT is close to the original analysis of Zinberg and Symonds with a difference of 0.9%. The difference between the values of other investigators (Singh et al. 1996) is less than 0.5% and is within 0.7% of the value obtained using Timoshenko beam theory beam formulation (Min-Yung Chang et al. 2004). The critical speed analysis was also carried out with slightly changed dimensions of 62.84 mm of mean diameter (Montagnier et al. 2014) and the critical speed obtained is within 2% of Zinberg and Symonds' original analysis. The results obtained using shell modeling and EMBT are very close with a difference of less than 0.2%. Hence Shell modeling using ANSYS SHELL281 element is found to be suitable for composite shaft modeling.

Table 5.1.   Comparison of first critical speed (rpm) of Zinberg shaft

Investigated by	Boron-Epoxy	Graphite-Epoxy
Zinberg and Symonds (1970) - Experimental unbalance response	6000	-
Zinberg and Symonds (1970) - Experimental without rotation (static)	5500	-
Zinberg and Symonds (1970) - EMBT	5780	-
Henrique dos Reis et al. (1985) - Donnel's shell theory	4950	-
Kim and Bert (1993) - Sanders shell theory	5872	5349
Kim and Bert (1993) - Donnel's shell theory	6399	5805
[1]Singh et al. (1996) -EMBT	5747	-
[1]Chang et al. (2004) – Timoshenko beam theory	5762	5197
[1]Gubran et al. (2005a) -MEMBT	5332	-
[1]Gubran et al. (2005a) -LBT	5620	-
[1]Sino et al. (2009) - SHBT	5767	-
[1]Qatu et al (2010) - Euler - Bernoulli beam theory	6148	-
[1]Qatu et al. (2010) - Finite element method-ABAQUS	5753	-
[1]Qatu et al. (2012) - FSDBT	5421	
[2]Montagnier et al. (2014) - EMBT	5852	-
[1]Present work using EMBT beam model in ANSYS	5724	-
[2]Present work using EMBT beam model in ANSYS	5673	-
[1]Present work using shell model in ANSYS	5732	5187

[1]Shaft mean diameter of 63.5/63.45 mm, [2]Shaft mean diameter of 62.84 mm (as used by Montagnier et al., 2014)

5.1.2 Zorzi-Nelson Rotating Damping Model

The results from the parametric study of Zorzi-Nelson rotating internal damping are tabulated in Table 5.2 only for the forward modes as instability due to internal damping does not affect the backward modes. For the internal viscous damping value of 0.0002s and isotropic bearing support stiffness of 175e5 N/m without external damping, both the rigid forward modes are unstable beyond their respective critical speeds. The addition of external support damping of 1750 Ns/m stabilizes the II Forward mode but the I Forward mode remains unstable. Besides, the I Forward mode stabilizes when the external damping is increased to 4500 Ns/m. When the external damping is completely removed, and stiffness anisotropy is introduced (K_{yy} =175e5 N/m and K_{zz} = 260e5 N/m), the rotor dynamic instability disappears in both the modes.

Table 5.2.　　Parametric study of Zorzi and Nelson damping model

Sl. No.	Bearing stiffness (N/m²)		Bearing damping (Ns/m)		Internal damping (s)	I Forward Critical		II Forward Critical	
	K_{YY}	K_{ZZ}	C_{YY}	C_{ZZ}	β	rpm	LD	rpm	LD
1	175e5	175e5	0	0	0	5097	0	10681	0
2	175e5	175e5	0	0	2e-10	5097	-2e-7	10681	0
3	175e5	175e5	0	0	2e-6	5097	-0.0025	10681	0.001
4	175e5	175e5	0	0	2e-4	5108	0.0001	10694	0.0018
5	175e5	175e5	1750	1750	2e-4	5093	0.0025	10693	-0.323
6	175e5	175e5	4000	4000	2e-4	5292	0.0011	11315	-0.699
7	175e5	175e5	4500	4500	2e-4	5288	-0.0013	11295	-0.789
8	175e5	250e5	0	0	2e-4	5133	0.0297	12573	-0.055
9	175e5	260e5	0	0	2e-4	5131	-0.02	12805	-0.058

For the hysteretic damping, loss factor of 0.04 at 4000 rpm was used as the value of 0.0002 used by Zorzi & Nelson was found to be too small to cause instability (Montagnier and Hochard 2007). This is justified by the stability thresholds arrived for the loss factor of 0.04 at the frequency of rotation of 66.6 Hz which is equal to the proportional damping (β) 0.000191s. The same is also verified by the mass unbalance response analysis on the Zorzi & Nelson model. The unbalance response with the proportional β damping of 0.0002s is shown in Figure 5.1.
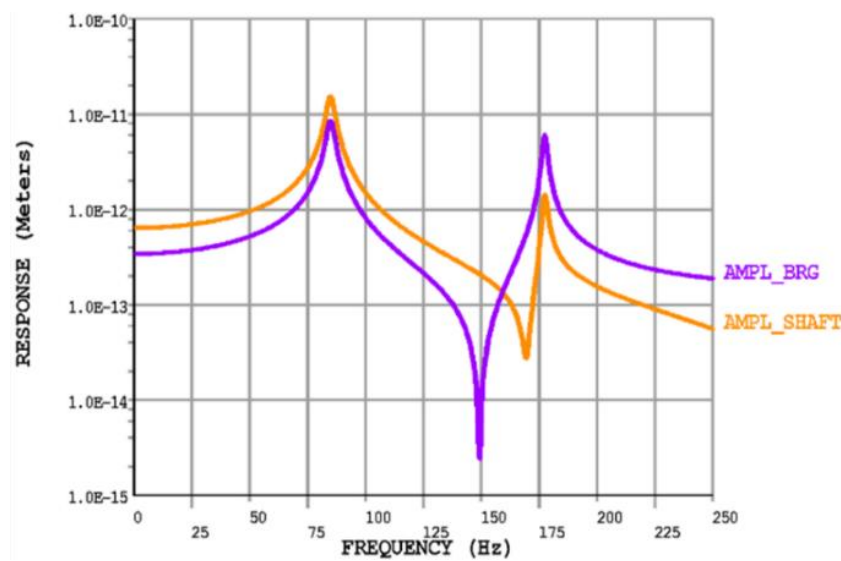
Figure 5.1.　　Unbalance response of Zorzi shaft with internal viscous damping

Similarly, the unbalance response with the same unbalance and loss factor 0.04 is shown in Figure 5.2. From the unbalance response analysis, it is evident that the hysteretic damping value of 0.0002 used by Zorzi and Nelson is the equivalent proportional damping for the hysteretic damping loss factor of 0.04. The equivalent viscous damping of 0.0002s in terms of β damping induces a similar effect as explained for viscous internal damping.
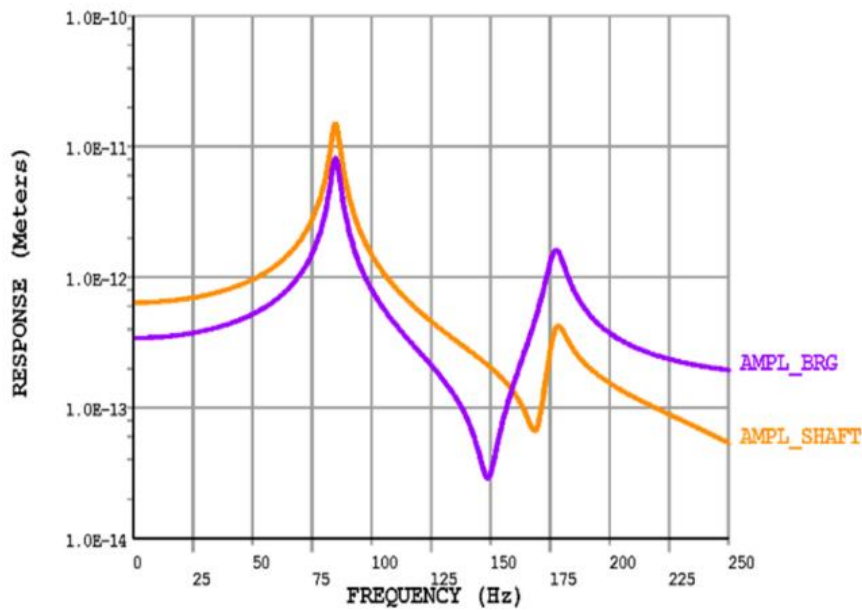
Figure 5.2.   Unbalance response of Zorzi shaft with internal hysteretic damping

Thus, it can be concluded that the equivalent proportional damping can be satisfactorily used to model the rotating internal damping in ANSYS for both the viscous and hysteretic damping models.

5.1.1 Hollow Steel Shaft Supported on Two End Bearings

The lateral natural frequencies of a non-rotating beam of 3 elements were found to be 64 Hz, 167.7 Hz, 277.8 Hz, and 632.86 Hz against the original published results of 58.92 Hz, 155.91 Hz, 273.53 Hz and 482.21 Hz (Genta and Amati 2010). However, for the more discretized model of 20 elements, the values were found to be closely matching (59.04 Hz, 154.08 Hz, 261.31 Hz, and 482.76 Hz).

72

The material loss factor was modeled as proportional stiffness damping. The Campbell diagram of the hollow shaft is shown in Figure 5.3. The stability map using the logarithmic decrement values obtained for the equivalent proportional damping is shown in Figure 5.4. I FW mode is found to be unstable above 873 Hz as observed in the original work. Thus, the methodology adopted in this work agrees well with the results of the original work.
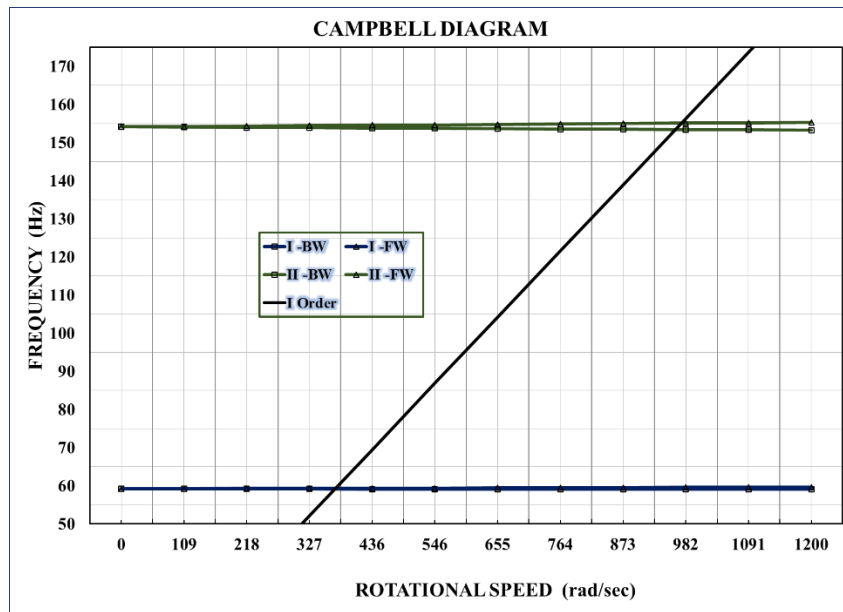
Figure 5.3.   Campbell diagram of hollow shaft
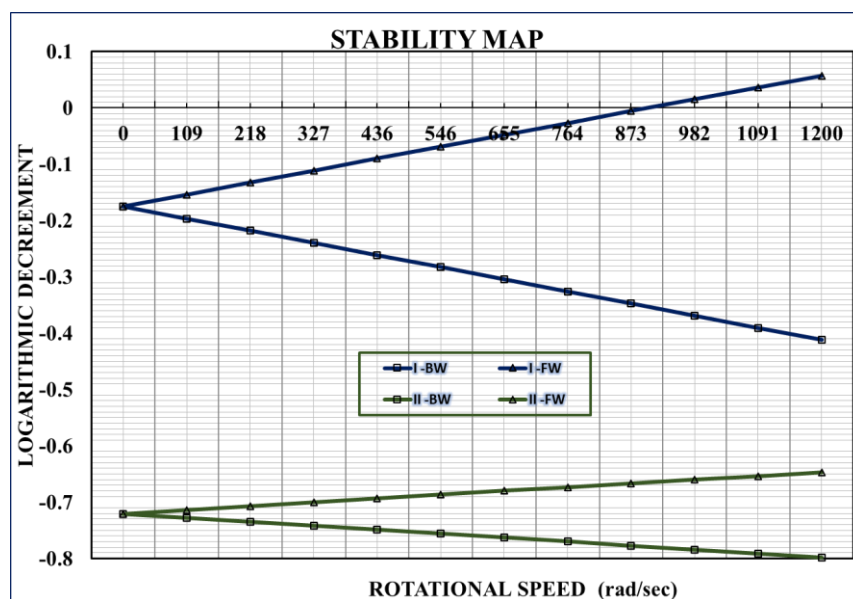
Figure 5.4.   Stability map of the hollow shaft

73

5.2 Composite Shaft Rotor-Bearing Systems

The rotor dynamic investigation of the composite shaft in three rotor-bearing systems given in Table 4.4 was carried out using the finite element method as per section 4.3. The numerical results obtained from the investigation are presented and discussed in the following subsections.

5.2.1 Preliminary Modal Analysis

The natural frequencies of the first three lateral modes of three rotor-bearing systems obtained from the modal analysis are tabulated in Table 5.3. The modal frequency values of the three rotor-bearing systems for the four composite shaft materials given in Table 4.5 of section 4.2 are compared with the existing steel shaft. For the first rotor-bearing configuration (GGRBS), the II modal frequency values for all the composite materials increase compared to the existing steel system. For the existing steel shaft rotor-bearing system, the critical speed due to the II mode is close to 550 Hz considering the gyroscopic damping effect of the rotor discs with a thin separation margin to the lower operating speed of 700 Hz. Hence increase in the existing II modal frequency is not acceptable for the smooth operation of the rotating machine. Hence the first rotor-bearing system was found to be not suitable for the composite shaft application.

Table 5.3.   Modal Analysis for the layer sequence [90, 45, -45, 0_6, 90]

Configuration	Material	Mode 1 (Hz)	Mode 2 (Hz)	Mode 3 (Hz)
1 (GGRBS)	Steel	160	405	950
	Glass/Epoxy	65	412	975
	Graphite/Epoxy	78	495	1150
	Carbon/Epoxy	85	524	1286
	Boron/Epoxy	91	590	1450
2 (LPRBS)	Steel	148	188	345
	Glass/Epoxy	156	198	359
	Graphite/Epoxy	155	194	362
	Carbon/Epoxy	155	194	362
	Boron/Epoxy	155	194	362
3 (PTRBS)	Steel	119	289	380
	Glass/Epoxy	102	301	363
	Graphite/Epoxy	113	342	465
	Carbon/Epoxy	117	333	498
	Boron/Epoxy	123	341	515

For the second rotor-bearing system (LPRBS), the preliminary modal analysis was not conclusive as the modal frequency values almost remain the same for all the materials. For the third configuration (PTRBS), the preliminary modal analysis indicates the advantage of the composite material shaft. Hence LP and PT rotor-bearing systems were taken up for further investigation.

5.2.2 Rotor Dynamic Analysis of LP Rotor-Bearing System

As the preliminary modal analysis was inconclusive, the LP shaft was further investigated. The parametric modal analysis as per section 4.3.2 and critical speed analysis as per section 4.3.3 was carried out.

5.2.2.1 Parametric Modal Analysis

As observed in the preliminary modal analysis, the LP shaft was found to be not sensitive to the parametric modal analysis for all the four types of composite materials. The modal frequency values of three layer sequences of the parametric modal analysis are tabulated in Table 5.4. The tabulated modal frequency values are almost constant for all the combinations for all the four composite materials indicating the ineffectiveness of composite shaft in the present form.

Table 5.4.   Modal frequency analysis of LP rotor-bearing system

Layer sequence		$[0, 90, -45, -90, -45, 0, 45, 90, -45]$			$[90, 45, -45, 0_6, 90]$			$[45, 0, 90, -45_2, 90_2, 0_2, 45]$		
Thickness (mm)		4	5	6	4	5	6	4	5	6
I Mode (Hz)	GL/E	156	156	156	156	156	156	156	156	156
	GR/E	155	155	155	155	155	155	155	155	155
	C/E	155	155	155	155	155	155	155	155	155
	B/E	155	155	155	155	155	155	155	155	155
II Mode (Hz)	GL/E	198	198	198	198	198	198	198	198	198
	GR/E	194	194	194	194	194	194	194	194	194
	C/E	194	194	194	194	194	194	194	194	194
	B/E	194	194	194	194	194	194	194	194	194
III Mode (Hz)	GL/E	359	359	359	359	359	359	359	357	358
	GR/E	362	362	362	362	362	362	362	362	362
	C/E	362	362	362	362	362	362	362	362	362
	B/E	362	362	362	362	362	362	362	362	362

GL/E- Glass/Epoxy, GR/E- Graphite/Epoxy,
C/E –Carbon/Epoxy, B/E- Boron/Epoxy

5.2.2.2 Critical Speed Analysis

The critical speed analysis of LP rotor-bearing system was carried out with the graphite-epoxy shaft of ten layers of layup sequence [90, 45, -45, 0_6, 90]. To have more clarity on the viability of composite shaft application for the LP shaft, the critical speed analysis was carried in two configurations. Along with the existing three-bearing support configuration, the two-bearing support configuration was also analyzed to check for any possible advantages of the composite shaft. The critical speeds were evaluated from the Campbell diagrams. The evaluated critical speeds and the strain energy levels in the shaft are tabulated in Table 5.5.

Table 5.5.　　　LP shaft critical speed (CS) and strain energy (SE) comparison

Modes		Steel shaft				Graphite-Epoxy shaft			
		Two bearings		Three bearings		Two bearings		Three bearings	
		CS (rpm)	SE (%)	CS (rpm)	SE (%)	CS (rpm)	SE (%)	CS (rpm)	SE (%)
1	I BW	5795	93.1	7892	13.9	6850	84.75	8084	17.9
	I FW	8802		8815		8895		8980	
2	II BW	8668	10.8	9998	32.7	8691	19.4	10702	27
	II FW	10842		12435		10961		12759	
3	III BW	11872	29.5	19044	65.2	11947	15	17646	73.3
	III FW	13922		>35000		12954		28876	

For the two-bearing support configuration, the Campbell diagrams of the existing steel and the proposed graphite-epoxy shafts are shown in Figure 5.5 and Figure 5.6 respectively. From the Campbell diagrams, it was found that all the three modes fall inside the operating speed range. For the composite shaft rotor-bearing system, the critical speed values of all the three critical modes are changed only marginally. The first critical mode remains to be a flexure mode in the proposed composite shaft as the rotor strain energy levels are only marginally improved for the graphite-epoxy shaft. Hence the critical speed analysis carried out effectively rules out the possibility of a simpler two bearing rotor-bearing system.
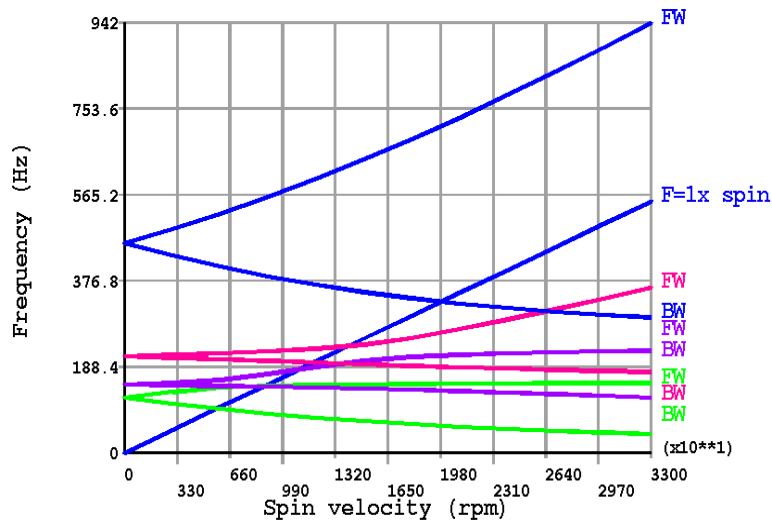
Figure 5.5.   Campbell diagram of LPRBS - steel shaft on two bearing supports
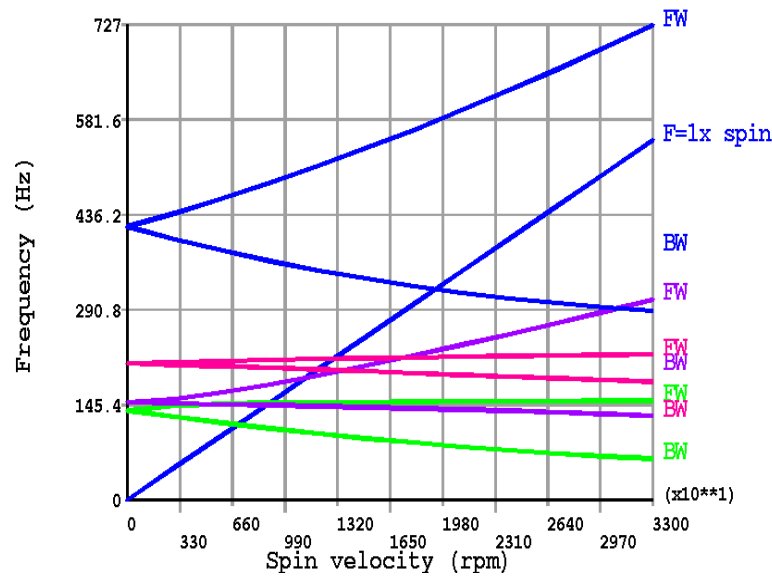
Figure 5.6.   Campbell diagram of LPRBS - graphite-epoxy shaft on two bearings

For the three bearing support configuration, the Campbell diagrams of the existing steel and graphite-epoxy shafts are shown in Figure 5.7 and Figure 5.8 respectively. The critical speed values and strain energy levels of the first two modes are marginally increased for the composite shaft rotor-bearing system compared to the steel shaft rotor-bearing system. However, the third mode of the composite shaft is reduced to fall within the operating range. Whereas, the third mode of the steel shaft is above the maximum

77

speed. Hence for the three bearings configuration also the graphite-epoxy shaft is found to be an ineffective solution in the present form.
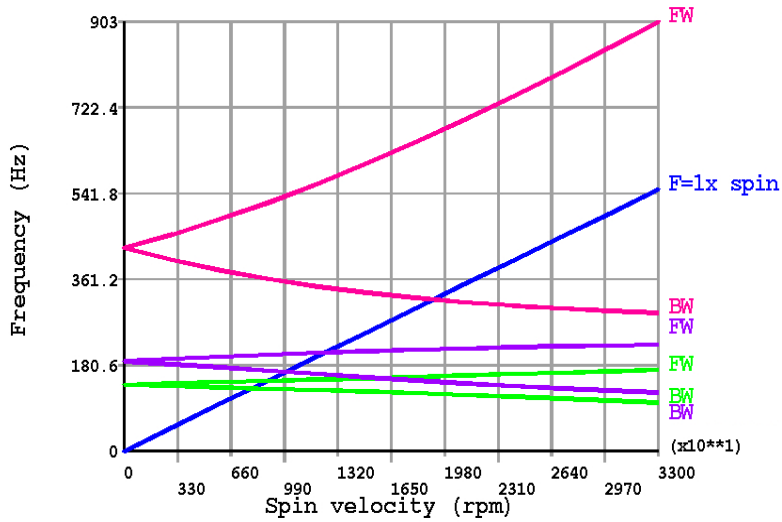
Figure 5.7.   Campbell diagram of LPRBS - steel shaft on three bearing supports
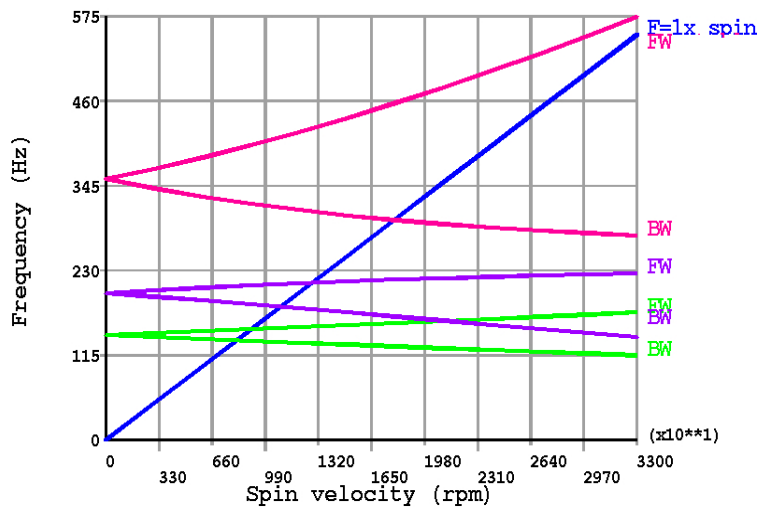
Figure 5.8.   Campbell diagram of LPRBS - graphite-epoxy shaft on three bearings

As evident from the parametric modal analysis, the other two composite materials also behave similarly like graphite-epoxy. Based on the parametric modal analysis and the critical speed analysis, it was concluded that the composite shaft application in the LP shaft requires further modifications in the gas turbine engine layout.   Hence further Analysis of the LP rotor-bearing system was discontinued.

78

5.2.3 Rotor Dynamic Analysis of PT Rotor-Bearing system

The preliminary modal analysis of the power turbine shaft rotor-bearing system discussed in section 5.2.1 indicated that the composite material shaft can improve the dynamics. Hence the detailed rotor dynamic investigations were carried out to ascertain the application and the analysis results are presented in the following subsections.

5.2.3.1 Parametric Analysis

The parametric modal analysis was carried out as per the procedure outlined in section 4.3.2. Some of the analysis results such as the combination of 12 layers with 5mm wall thickness are tabulated in Table 5.6. Similarly, in Table 5.7 the results obtained using the combination of 10 layers with 5mm wall thickness are tabulated. In Table 5.8, the modal frequency values for the combinations of 8 layers with 5mm wall thickness are tabulated.

Table 5.6.   Modal analysis for 12 layers and 5 mm wall thickness

	Sl. No.	1	2	3	4	5	6	7	8	9
Layer sequences (degrees)	1	0	0	45	45	-45	-45	90	90	90
	2	-45	90	90	90	-45	0	-45	45	45
	3	45	45	90	-45	45	45	90	-45	-45
	4	90	0	0	0	45	90	90	0	0
	5	0	45	0	0	0	0	90	0	0
	6	-45	-45	-45	-45	0	45	90	0	0
	7	0	90	-45	90	90	90	45	0	0
	8	45	45	45	45	90	-45	0	0	0
	9	90	90	45	0	45	90	-45	0	0
	10	-45	0	90	-45	45	45	90	90	0
	11	45	45	90	-45	-45	45	45	45	0
	12	0	-45	45	90	-45	0	0	-45	90
I Mode (Hz)	GL/E	92	93	90	92	91	92	91	94	96
	GR/E	103	103	97	100	98	101	99	107	112
	C/E	108	107	99	103	100	104	102	113	118
	B/E	110	109	103	107	103	107	106	115	121
II Mode (Hz)	GL/E	319	318	303	314	308	315	310	322	324
	GR/E	328	329	327	328	328	328	328	329	330
	C/E	329	329	328	329	328	329	328	330	330
	B/E	329	329	327	328	327	328	328	329	330
III Mode (Hz)	GL/E	372	369	344	356	349	359	350	394	420
	GR/E	580	565	482	530	500	542	512	625	660
	C/E	628	615	518	575	535	591	552	680	700
	B/E	605	595	520	565	528	578	552	650	680

Table 5.7.   Modal analysis for 10 layers with 5 mm wall thickness

Sl No.		1	2	3	4	5	6	7	8	9
Layer sequences (degrees)	1	0	0	45	45	-45	-45	90	90	90
	2	90	90	90	0	-45	0	-45	45	45
	3	45	-45	90	90	45	45	45	-45	-45
	4	0	90	0	-45	45	90	45	-45	0
	5	45	0	0	-45	0	0	45	-45	0
	6	-45	-45	-45	90	0	90	45	90	0
	7	90	0	-45	90	90	45	45	90	0
	8	45	45	45	0	90	-45	45	90	0
	9	90	90	45	0	-45	0	0	0	0
	10	0	-45	90	45	-45	90	90	45	90
I Mode (Hz)	GL/E	93	92	91	93	91	92	90	90	96
	GR/E	105	101	99	103	99	102	96	97	111
	C/E	110	104	101	107	101	106	97	102	117
	B/E	112	108	105	110	105	109	101	102	120
II Mode (Hz)	GL/E	320	315	309	318	311	316	307	327	324
	GR/E	329	328	328	329	328	328	327	327	330
	C/E	330	329	328	329	328	329	328	327	331
	B/E	329	328	328	329	328	328	327	327	330
III Mode (Hz)	GL/E	381	359	350	369	352	363	344	344	412
	GR/E	600	540	510	570	510	555	465	478	650
	C/E	650	585	550	620	550	605	486	510	695
	B/E	630	575	545	620	545	590	500	520	670

Table 5.8.   Modal analysis for 8 layers with 5 mm wall thickness

Sl No.		1	2	3	4	5	6	7	8	9
Layer sequences (degrees)	1	0	0	45	45	-45	-45	90	90	90
	2	-45	90	90	0	-45	0	-45	45	45
	3	45	45	90	90	45	45	90	-45	-45
	4	90	0	0	-45	45	90	90	0	-45
	5	0	45	0	-45	0	0	90	0	-45
	6	-45	-45	-45	90	0	90	90	0	-45
	7	0	0	-45	90	90	45	45	0	-45
	8	45	45	45	0	90	-45	0	90	90
I Mode (Hz)	GL/E	93	92	92	92	92	91	90	95	89
	GR/E	104	103	100	100	101	100	96	108	90
	C/E	108	107	104	103	104	103	98	114	90
	B/E	111	110	107	107	108	106	103	117	94
II Mode (Hz)	GL/E	320	319	315	314	315	313	302	323	276
	GR/E	329	329	328	328	328	328	327	330	320
	C/E	329	329	328	329	329	329	327	330	315
	B/E	329	329	329	328	328	328	327	330	323
III Mode (Hz)	GL/E	378	375	359	357	359	355	343	400	352
	GR/E	587	580	540	530	541	530	472	630	366
	C/E	641	626	590	570	585	575	503	680	352
	B/E	618	605	575	570	578	565	578	655	402

From the modal analysis results, as tabulated, it was found that for the layup sequences of [90, 45, -45, 0_8, 90], [90, 45, -45, 0_6, 90] and [90, 45, -45, 0_4, 90], the III lateral mode frequencies increase as desired. Also, there is an indication of increase in II lateral mode frequency. Hence the results were further closely analyzed for these layup sequences by varying the thickness and the results are tabulated in Table 5.9.

Table 5.9.   Modal frequency analysis of PTRBS

Layer sequence		[90, 45, -45, 0_4, 90]			[90, 45, -45, 0_6, 90]			[90, 45, -45, 0_8, 90]		
Thickness (mm)		4	5	6	4	5	6	4	5	6
I Mode (Hz)	GL/E	91	93	95	94	96	98	105	99	102
	GR/E	101	103	108	106	111	114	125	116	114
	C/E	100	104	108	108	118	120	130	120	126
	B/E	109	115	118	114	120	124	136	126	131
II Mode (Hz)	GL/E	323	323	322	325	324	322	323	326	324
	GR/E	330	330	329	330	330	329	330	331	330
	C/E	330	330	329	330	330	330	331	332	332
	B/E	330	330	329	330	330	330	330	331	331
III Mode (Hz)	GL/E	385	391	390	412	412	413	453	462	457
	GR/E	635	626	620	661	662	671	669	708	687
	C/E	635	635	625	700	701	708	725	772	746
	B/E	658	645	640	690	695	698	677	724	698

For the torsional stress analysis of the composite material power turbine shaft, the occasional over-torque of 415 Nm was applied at one end of the shaft and the other end was fixed as shown in Figure 4.7 of section 4.3.2. The normal maximum operating torque is approximately 350 Nm. The maximum Von-Mises stress, First Principal stress, and Shear stress values ($\tau xy= \tau zx$ and τyz) are tabulated as shown in Table 5.10, Table 5.11, Table 5.12, and Table 5.13 respectively.

Table 5.10.   Maximum Von-Mises Stress

Layer Sequences	Wall thickness (mm)	Von-Mises stress (MPa)			
		GL/E	GR/E	C/E	B/E
[90, 45, -45, 0_8, 90]	4	162	120	85.1	104
	5	146	111	80.4	97.4
	6	86.6	68	50.9	60.3
[90, 45, -45, 0_6, 90]	4	156	110	75	94.1
	5	141	102	70.9	87.9
	6	84.8	63.4	45.6	55.1
[90, 45, -45, 0_4, 90]	4	148	97.5	63	81.2
	5	134	90.2	59.3	75.7
	6	81.7	56.9	38.8	48.2

Table 5.11.   Maximum I Principal Stress

Layer Sequences	Wall thickness	I Principal stress (MPa)			
		GL/E	GR/E	C/E	B/E
[90, 45, -45, 0_8, 90]	4	93.4	69.3	48.7	60
	5	84	63.9	45.9	55.9
	6	49.7	38.5	27.9	33.9
[90, 45, -45, 0_6, 90]	4	90	63.5	42.8	54
	5	81.2	58.7	40.4	50.4
	6	48.5	35.7	24.5	30.7
[90, 45, -45, 0_4, 90]	4	85.1	56	35.9	46.4
	5	76.9	51.7	33.6	43.2
	6	46.5	31.7	20.4	26.4

Table 5.12.   Maximum Shear Stress ($\tau_{xy} = \tau_{zx}$)

Layer Sequences	Wall thickness (mm)	Shear stress (MPa)			
		GL/E	GR/E	C/E	B/E
[90, 45, -45, 0_8, 90]	4	93.6	69.5	49.1	60.3
	5	84.2	64.1	46.4	56.2
	6	50	39.2	29	34.7
[90, 45, -45, 0_6, 90]	4	90.2	63.7	43.3	54.3
	5	81.4	59	40.9	50.7
	6	48.9	36.5	25.9	31.7
[90, 45, -45, 0_4, 90]	4	85.4	56.3	36.3	46.8
	5	77.1	52.1	34.2	43.7
	6	47.1	31.7	21.9	27.7

Table 5.13.   Maximum Shear Stress (τ_{yz})

Layer Sequences	Wall thickness (mm)	Shear stress (MPa)			
		GL/E	GR/E	C/E	B/E
[90, 45, -45, 0_8, 90]	4	0.4	0.60	2.49	1.48
	5	0.5	0.78	3.3	1.95
	6	0.7	1.01	4.39	2.58
[90, 45, -45, 0_6, 90]	4	0.5	0.68	2.62	1.65
	5	0.7	0.88	3.47	2.17
	6	0.8	1.15	4.62	2.88
[90, 45, -45, 0_4, 90]	4	0.6	0.74	2.62	1.76
	5	0.7	0.98	3.45	2.31
	6	1.02	1.25	4.59	3.06

The maximum stress values of all the combinations are well within the normal and shear strength of the material used in the analysis. The von-mises stress, first principal stress, maximum tensile and shear stress plots of graphite-epoxy composite material tube of 5 mm wall thickness with layup orientation [90, 45, -45, 0_6, 90] are respectively shown in Figure 5.9, Figure 5.10, Figure 5.11 and Figure 5.12.
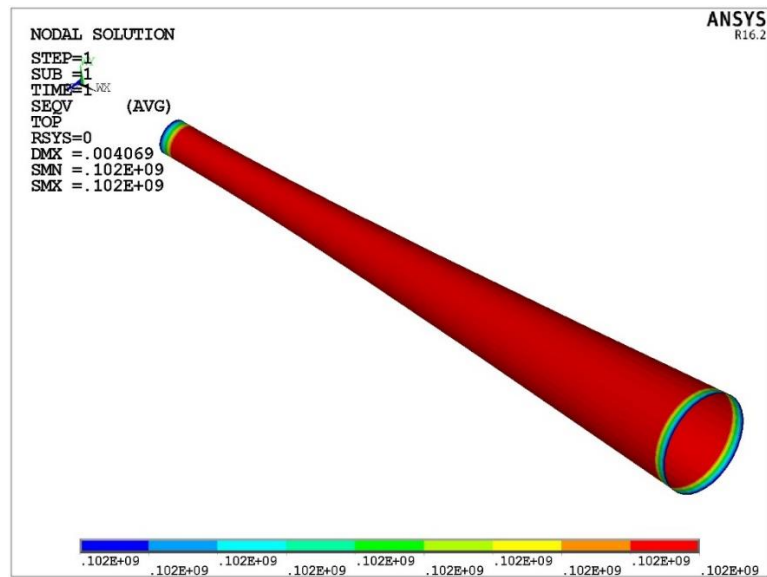
Figure 5.9.   Von-Mises stress plot of Graphite-epoxy tube
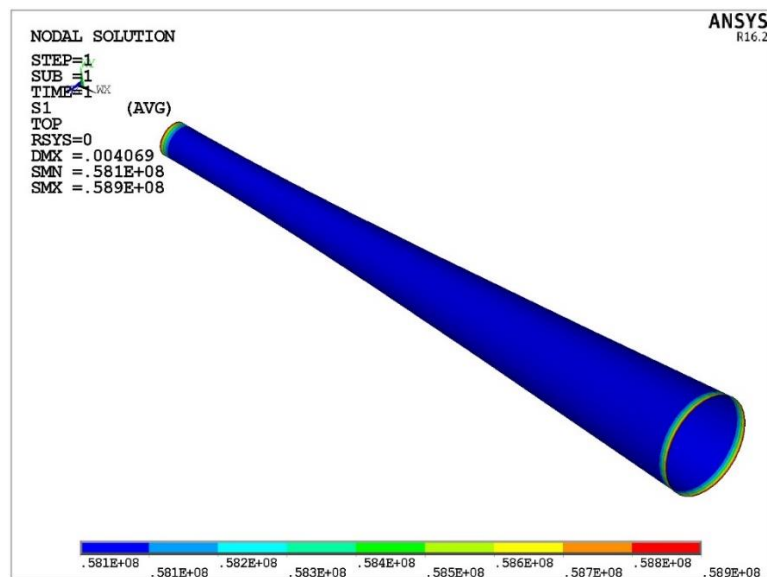
Figure 5.10.   I Principal stress plot of Graphite-epoxy tube
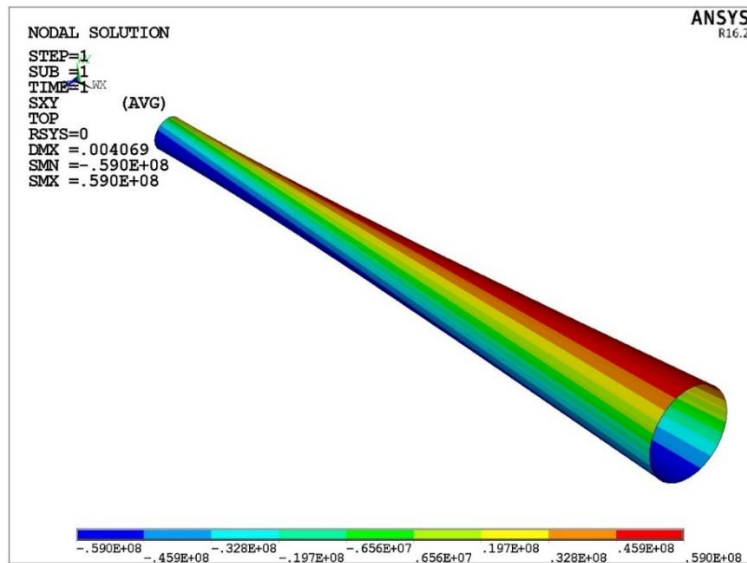
Figure 5.11.   Shear stress ($\tau_{xy} = \tau_{zx}$) plot of Graphite-epoxy tube
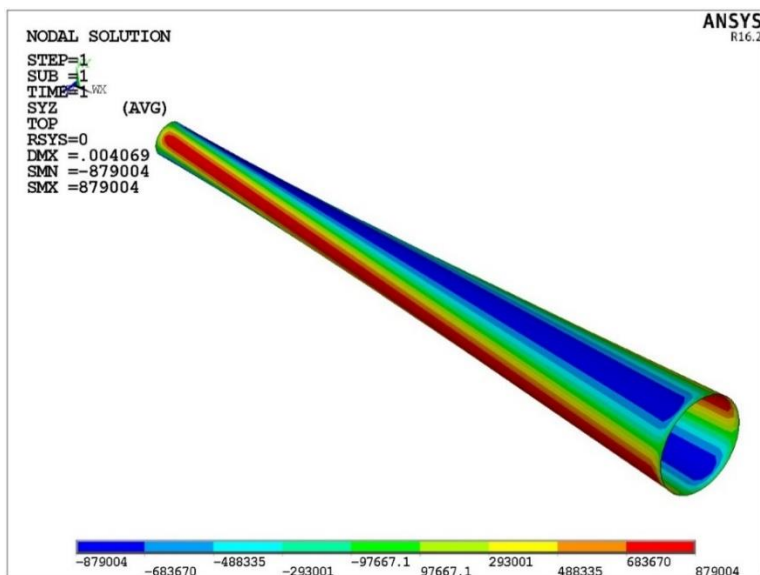
Figure 5.12.   Shear stress (τ_{yz}) plot of composite material tube

The parametric analysis carried out indicates an unfavourable situation for the glass-epoxy material. For the glass-epoxy material shaft, the modal frequency of III mode of the rotor-bearing system reduces compared to the existing steel shaft rotor-bearing system. From the torsional stress analysis also the glass-epoxy material was found to be not suitable as stress values are close to the ultimate strength values. For the other

three materials, the increase in I and II modal frequencies indicates an improvement in the shaft stiffness.

5.2.3.2   Critical Speed Analysis

The critical speed analysis was carried out using the graphite-epoxy material with ten layers of [90, 45, -45, 0_6, 90] layup sequence. Graphite-epoxy was selected among the three materials as glass-epoxy was found to be not adequate for the application. The Campbell diagrams of steel and composite shaft rotor-bearing system are shown in Figure 5.13 and Figure 5.14 respectively. The critical speed values evaluated from the Campbell diagrams and the corresponding percentage strain energies are tabulated in Table 5.14. The first critical speed of the composite shaft rotor-bearing system was found to be marginally increased with a reduced rotor strain energy compared to the original steel shaft rotor-bearing system. The second critical speed was also increased with a substantial reduction in the rotor strain energy. The Campbell diagram of the composite shaft rotor-bearing system indicates an increase in the third modal frequency.
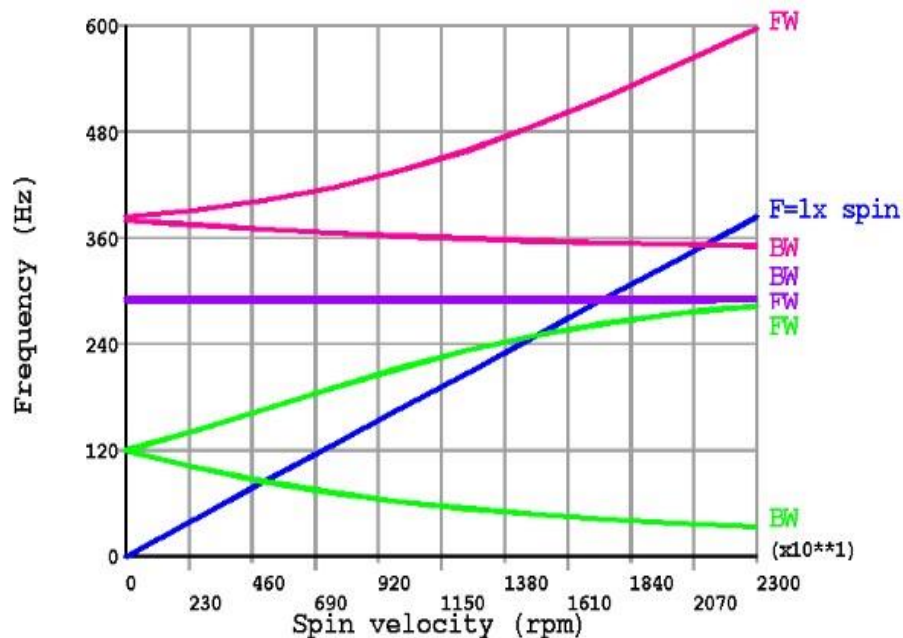
Figure 5.13.   Campbell diagram of PTRBS - Steel shaft
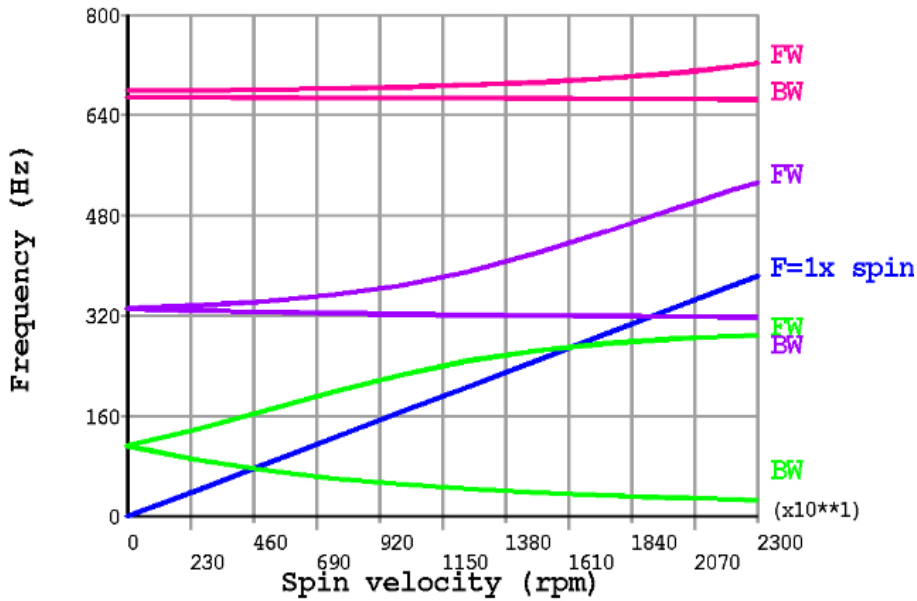
Figure 5.14.   Campbell diagram of PTRBS - Graphite-epoxy shaft

Table 5.14.   Power turbine rotor-bearing system critical speed analysis

Modes		Steel shaft		Graphite-Epoxy shaft	
		CS (rpm)	SE (%)	CS (rpm)	SE (%)
1	I BW	5054	54.8	4395	20
	I FW	15087		16215	
2	II BW	17308	33.1	19376	8.5
	II FW	17497		>23000	
3	III BW	21118	49.34	>23000	89.1
	III FW	>23000		>23000	

5.2.3.3   Stability Analysis

The stability analysis of the existing PT rotor-bearing system was carried out as per the section 4.3.4 for a set of known equivalent viscous damping coefficients. The damping values considered are due to the frictional joints of rotors due to the coupling arrangement employed to join the turbine rotors. For the existing steel shaft rotor-bearing system, the stability analysis was carried out for a set of practical damping values modeled as equivalent proportional damping. The existing steel shaft rotor-bearing system was found to be rotor dynamically stable as it meets the stability criteria for the supercritical shaft. All the logarithmic decrement values through which the stability of the rotor-bearing system was measured were found to be negative over the

86

entire operating speed range. The logarithmic decrement values extracted from the stability maps are tabulated in Table 5.15. The stability map of the existing power turbine rotor-bearing system for the internal damping of 0.00005s is shown in Figure 5.15.

Table 5.15.   Steel shaft rotor-bearing system with internal damping

Sl. No.	Beta damping coefficient (s)	I Forward Critical		II Forward Critical	
		rpm	Log decrement	rpm	Log decrement
1	0	15087	0	17497	0
2	0.00005	15120	-0.11	17415	-1.15
3	0.00010	15045	-0.08	17315	-0.01
4	0.00015	15021	-0.075	17234	-0.001
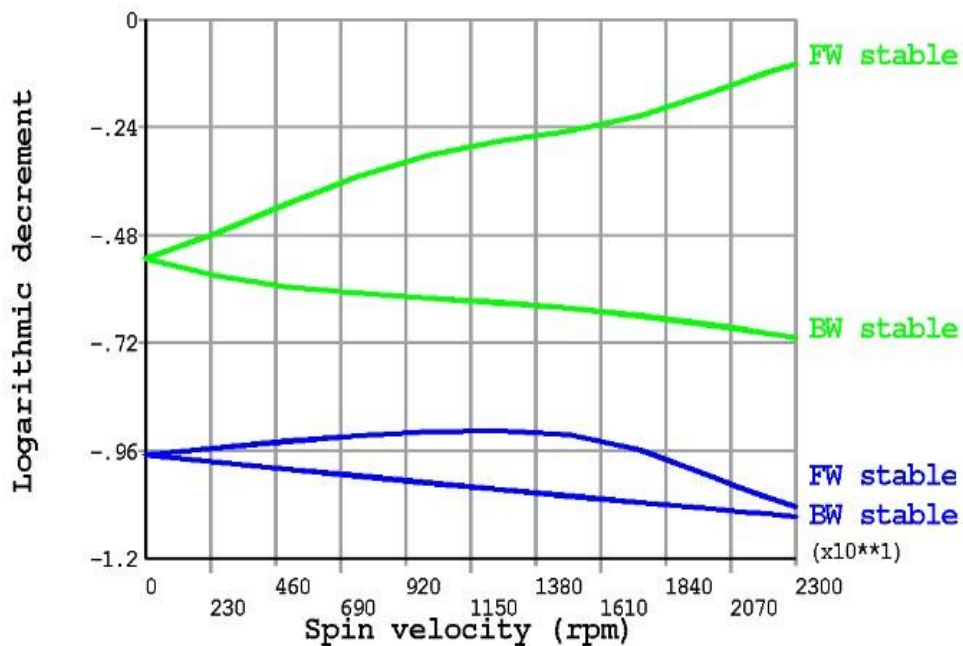
Figure 5.15.   Stability plot of steel shaft rotor-bearing system

The stability analysis of the composite shaft rotor-bearing system was also carried out to evaluate the effect of internal damping on its rotor dynamics. The composite shaft rotor-bearing system was also found to be rotor dynamically stable. The stability values of the composite shaft rotor-bearing system for a set of internal damping values in terms of logarithmic decrements are tabulated in Table 5.16. The stability map of composite shaft rotor-bearing system for the internal damping of 0.00005s is shown in Figure 5.16.

Table 5.16.　Composite shaft rotor-bearing system with internal damping

Sl. No.	Internal damping (s)	I Forward Critical		
		rpm	rad/sec	Log decrement
1	0	16260	1702.74	0
2	5.00E-04	16429	1720.44	-0.532
3	5.00E-03	16346	1711.75	-0.593
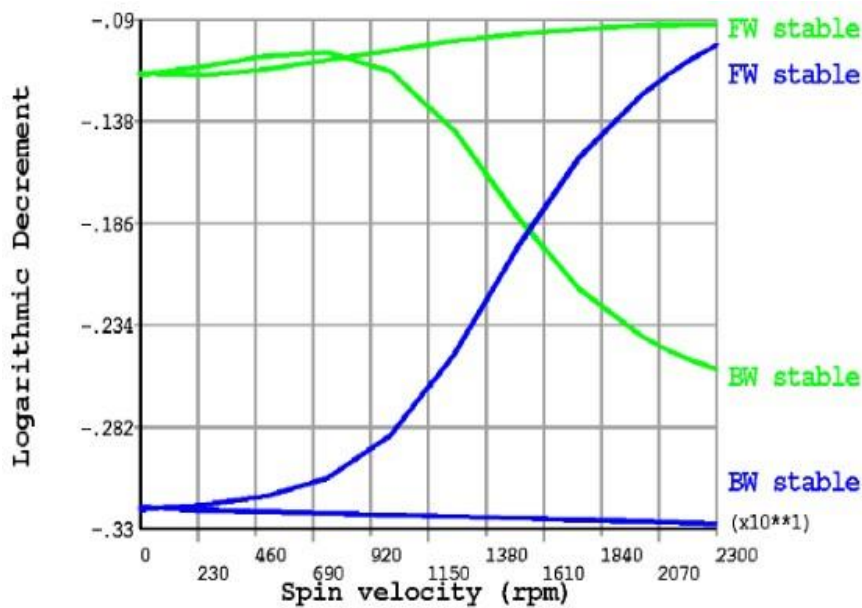
Figure 5.16.　Stability plot of graphite-epoxy shaft rotor-bearing system

5.2.3.4　Unbalance Response Analysis

Further, the residual unbalance response analysis for an unbalance of 5 cmg per plane on both the turbine discs was carried for both the steel and composite shaft rotor-bearing systems. The response amplitudes for the existing steel and composite shaft are shown in Figure 5.17 and Figure 5.18. The unbalance response amplitudes are tabulated in Table 5.17.

Table 5.17.　Unbalance response comparison (microns)

Sl. No.	Location	Steel shaft			Graphite/epoxy shaft	
		233 Hz	288 Hz	350 Hz	270 Hz	350 Hz
1	Shaft front	12.6	5	3	0.9	0.7
2	Shaft centre	157	14.6	23	22.5	15.5
3	Turbine end	33	10	2.9	19.2	5.6

From the unbalance response results tabulated, the composite shaft clearly shows an improvement over the existing steel shaft as the displacement at the center of the shaft reduced by 90%. The unbalance response thus carried out illustrates the improvement that can be achieved by the composite shaft rotor-bearing system which would eventually eliminate the high-speed balancing required for the existing rotor-bearing system.
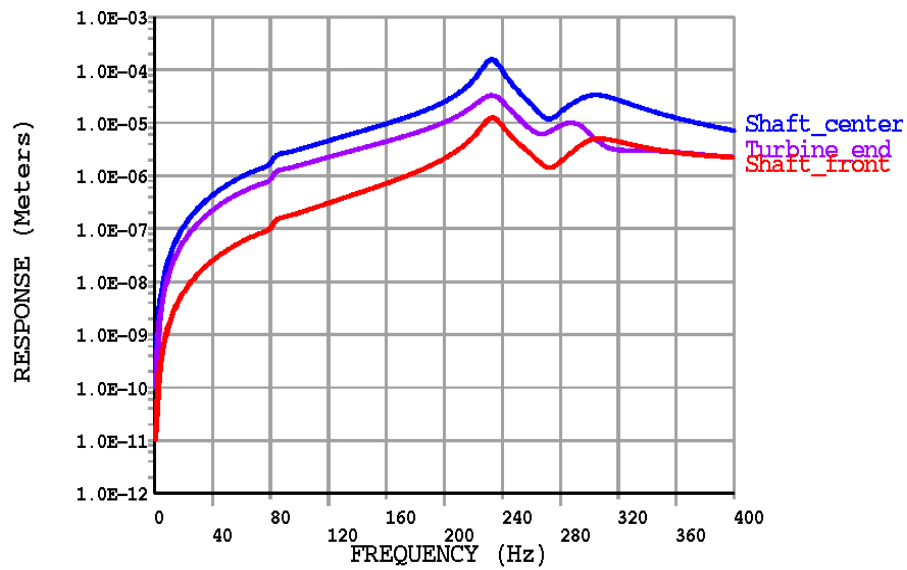
Figure 5.17.   Unbalance response of steel shaft of PT rotor-bearing system
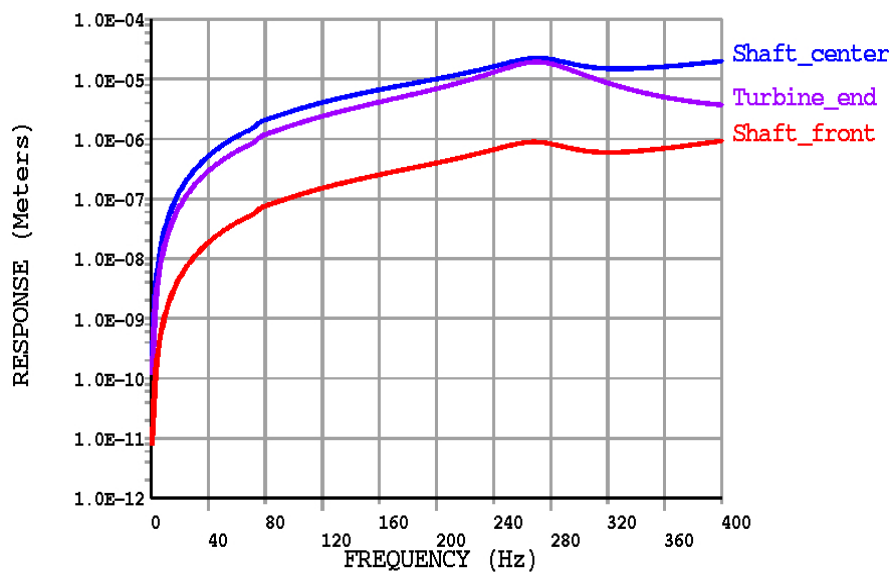
Figure 5.18.   Unbalance response graphite-epoxy shaft of PT

5.3 Hybrid Composite Material Shaft

As illustrated in the previous section 5.2.3, the power turbine shaft was found to be the right application for the composite shaft, the same was selected for the rotor dynamic study of hybrid composite material as well. The hybrid composite shaft was modeled as explained in section 4.4. The rotor dynamic results are presented in the following subsections.

5.3.1 Modal Analysis

For the initial estimates, the hybrid composite material proposed is comprised of graphite-epoxy composite material tube sandwiched by steel tubes. The outside diameter of the graphite-epoxy tubular shaft was reduced to 25 mm with 5 mm thickness to accommodate the outer and inner steel tubes. The range of modal frequencies of the first two mode shapes within the operating range as shown in Figure 5.19 was estimated. The estimated values of modal frequencies of the hybrid composite shaft are compared with the existing steel shaft as given in Table 5.18.

Table 5.18.   Modal analysis comparison

Mode Number	Existing shaft	Hybrid shaft
I	250 Hz	200 -260 Hz
II	280 Hz	330 - 430 Hz

(a)

(b)
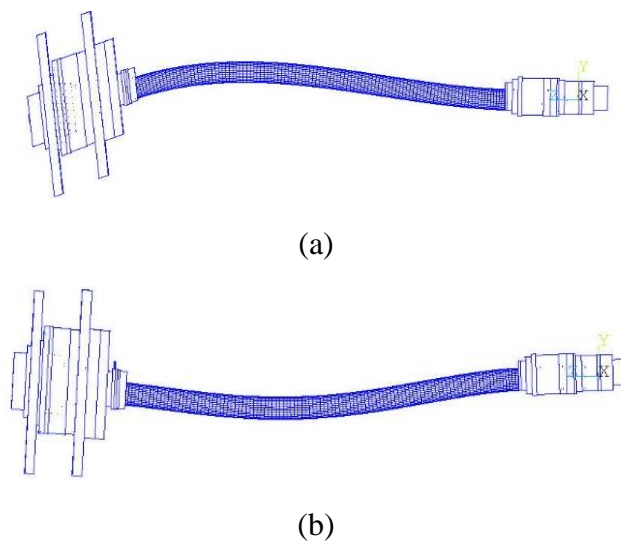
Figure 5.19.   Mode shapes of (a) I critical speed (b) II critical speed

Similarly, the modal frequencies of existing and hybrid bearing supports are compared in Table 5.19. The first two mode shapes of the bearing support are shown in Figure 5.20.

Table 5.19.   Modal analysis of supporting structure

Mode Number	Existing	Hybrid
I Mode (0D mode)	260 Hz	320-400 Hz
II Mode (1D mode)	690 Hz	850-900 Hz

(a)	(b)
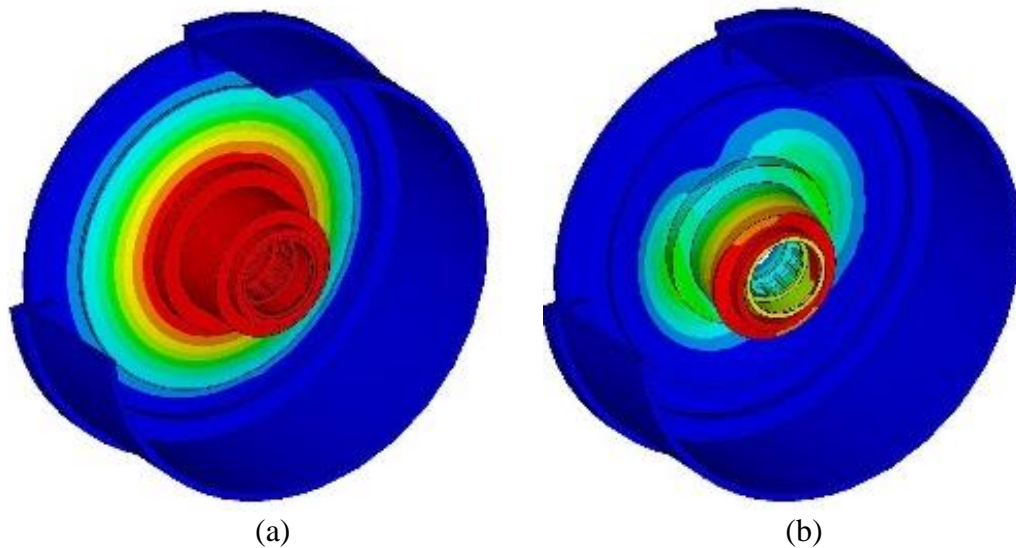
Figure 5.20.   Bearing supporting structure (a) 0D (Umbrella) mode (b) ID mode

The initial estimates of modal frequencies indicate that the hybrid composite material provides advantages to both the power turbine shaft and the bearing support. However, in the present study, the hybrid material is further analyzed for the power turbine shaft application.

5.3.2 Parametric Analysis

Parametric analysis of the hybrid composite shaft was carried out similar to the parametric analysis of composite material shaft presented in section 5.2.2.1.   The thickness of the composite material was varied by keeping the thickness of both the inner and outer steel tubes fixed at 1mm. The modal frequency values of some of the

selected iterations are indicated in Table 5.20. Based on the discrete analysis of various combinations, hybrid composite with a laminate sequence of [ST, 90, 45, -45, 0_6, 90, ST] was found to be the best from the modal analysis point of view.

The torsional stress analysis was also carried similar to the analysis carried out for the graphite-epoxy composite tube in section 5.2.2.1. The maximum values of Von-Mises stress, First Principal stress, Shear stresses ($\tau_{xy} = \tau_{xz}$ and τ_{yz}) on the outer steel layers for the three best rotor dynamic layer sequences arrived from the modal frequency analysis are tabulated in Table 5.21, Table 5.22, Table 5.23, and Table 5.24.

Table 5.20.   Modal frequency analysis for the variation in wall thickness (mm)

Layer sequence		[ST, 90, 45, -45, 0_6, 90, ST]			[ST, 45, -45, 90, 0_4, -45, 90, 45, ST]			[ST, 0, 45, -45, 90_6, 0, ST]		
Wall thickness		6	7	8	6	7	8	6	7	8
I Mode (Hz)	GL/E	103	112	126	102	111	118	101	110	117
	GR/E	112	118	123	108	115	121	105	113	119
	C/E	115	121	126	111	118	123	106	114	120
	B/E	117	122	127	113	119	124	108	115	121
II Mode (Hz)	GL/E	326	322	322	325	322	318	328	321	317
	GR/E	329	325	321	329	324	320	328	320	319
	C/E	330	326	322	329	325	321	328	324	320
	B/E	330	326	321	329	325	320	328	323	319
III Mode (Hz)	GL/E	458	454	488	447	448	443	434	442	440
	GR/E	552	503	477	524	488	46	488	470	457
	C/E	580	520	488	547	500	475	501	477	461
	B/E	575	518	487	544	499	474	504	478	461

Table 5.21.   Maximum Von-Mises Stress

Layer Sequences	Wall thickness (mm)	Von-Mises stress (MPa)			
		GL/E	GR/E	C/E	B/E
[ST, 90, 45, -45, 0_6, 90, ST]	6	575	549	551	527
	7	559	533	535	507
	8	544	514	521	489
[ST, 45, -45, 90, 0_4, -45, 90, 45, ST]	6	545	462	429	408
	7	524	431	396	373
	8	504	403	368	344
[ST, 0, 45, -45, 90_6, 0, ST]	6	575	549	551	527
	7	559	530	535	507
	8	544	514	521	489

Table 5.22.   Maximum I Principal Stress

Layer Sequences	Wall thickness (mm)	I principal stress (MPa)			
		GL/E	GR/E	C/E	B/E
[ST, 90, 45, -45, 0_6, 90, ST]	6	332	317	318	304
	7	323	307	309	294
	8	314	296	300	282
[ST, 45, -45, 90, 0_4, -45, 90, 45, ST]	6	315	267	248	235
	7	303	249	229	216
	8	291	233	212	199
[ST, 0, 45, -45, 90_6, 0, ST]	6	332	317	318	304
	7	323	306	309	294
	8	314	296	300	282

Table 5.23.   Maximum Shear Stress ($\tau_{xy} = \tau_{zx}$)

Layer Sequences	Wall thickness (mm)	Shear stress (MPa)			
		GL/	GR/E	C/E	B/E
[ST,90, 45, -45, 0_6, 90, ST]	6	332	317	318	304
	7	323	307	309	294
	8	314	296	300	282
[ST, 45, -45, 90, 0_4, -45, 90, 45, ST]	6	315	267	247	235
	7	302	249	228	215
	8	291	233	212	199
[ST, 0, 45, -45, 90_6, 0, ST]	6	332	317	318	304
	7	323	306	309	294
	8	314	296	300	282

Table 5.24.   Maximum Interlaminar Shear Stress (τ_{yz})

Layer Sequences	Wall thickness (mm)	Shear stress (MPa)			
		GL/E	GR/E	C/E	B/E
[ST, 90, 45, -45, 0_6, 90, ST]	6	0.18	0.18	0.26	0.28
	7	0.22	0.22	0.27	0.36
	8	0.25	0.33	0.49	0.46
[ST, 45, -45, 90, 0_4, -45, 90, 45, ST]	6	0.18	0.15	0.14	0.14
	7	0.22	0.18	0.17	0.16
	8	0.26	0.21	0.19	0.18
[ST, 0, 45, -45, 90_6, 0, ST]	6	0.18	0.17	0.2	0.21
	7	0.22	0.2	0.27	0.27
	8	0.25	0.25	0.35	0.39

From the comparison of modal frequency values of Table 5.20, it was found that the modal frequency values of the hybrid composite shaft of 6 mm thickness are higher for

the II and III modes. The hybrid [ST, 90, 45, -45, 0_6, 90, ST] shaft indicated the best modal frequency values. The stress values of all the combinations are found to be within the acceptable values. The Von-Mises stress, first principal stress, shear stress plots for the graphite-epoxy composite material tube of 7 mm wall thickness and laminate layup sequence of [ST, 90, 45, -45, 0_6, 90, ST] are shown Figure 5.21, Figure 5.22, Figure 5.23 and Figure 5.24.
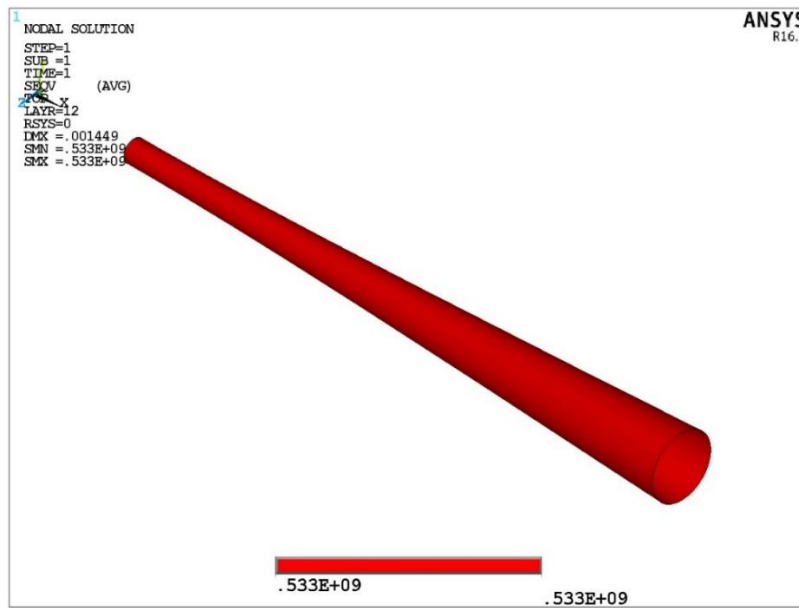
Figure 5.21.   Von-Mises stress plot of the hybrid composite tube
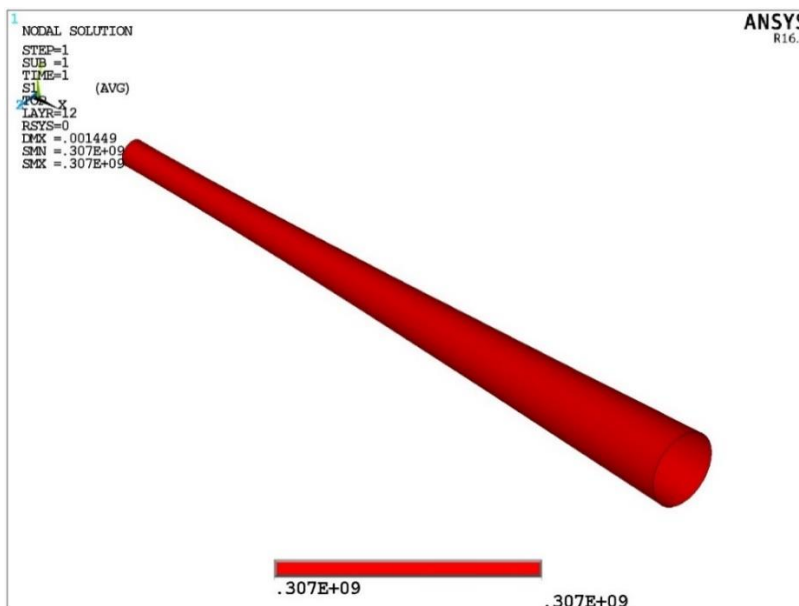
Figure 5.22.   I Principal stress plot of the hybrid composite tube
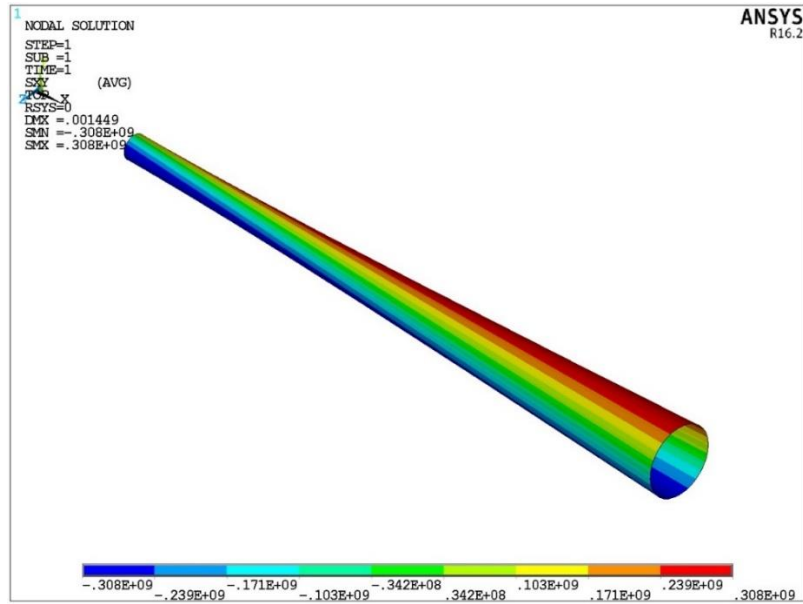
Figure 5.23.   Shear stress ($\tau_{xy} = \tau_{zx}$) plot of the hybrid composite tube
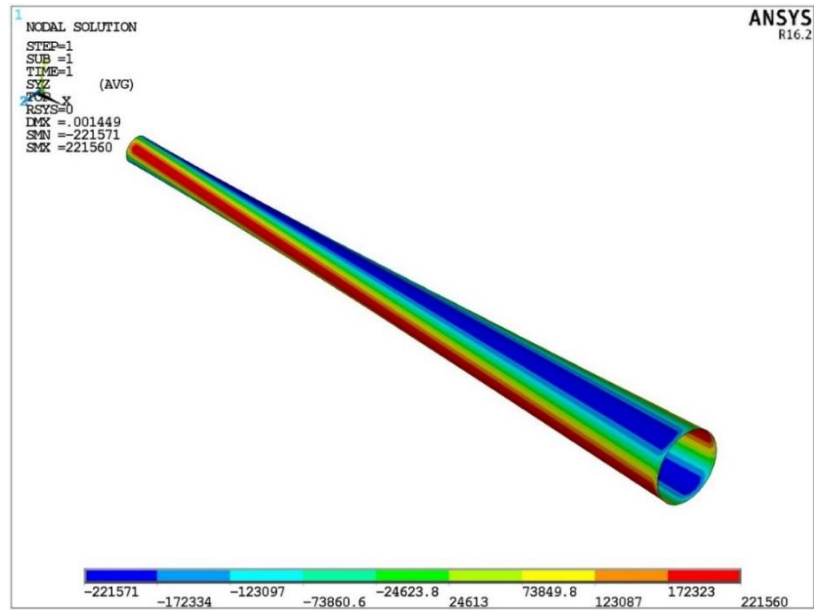
Figure 5.24.   Shear stress (τ_{yz}) plot of the hybrid composite tube

5.3.3 Critical Speed Analysis

For the critical speed analysis of hybrid composite shaft, graphite-epoxy tube of 4 mm thickness sandwiched between steel tubes of each 1 mm wall thickness of layer orientation [ST, 90, 45, -45, 0_6, 90, ST] was used. The critical speeds of the hybrid

shaft are compared with the existing solid steel shaft and graphite-epoxy shaft in Table 5.25. The Campbell diagram for the hybrid shaft is also shown in Figure 5.25.

Table 5.25.   Critical speeds (CS) and strain energy (SE) in the rotor system

Modes Shapes		Steel shaft		Graphite-Epoxy shaft		Hybrid Steel Graphite-Epoxy shaft	
		CS (rpm)	SE (%)	CS (rpm)	SE (%)	CS (rpm)	SE (%)
1	I BW	5054	54.8	4395	20	5005	22
	I FW	15087		16215		16075	
2	II BW	17308	33.1	19376	8.5	18861	16
	II FW	17497		>23000		>23000	
3	III BW	21118	49.34	>23000	89.1	>23000	82
	III FW	>23000		>23000		>23000	
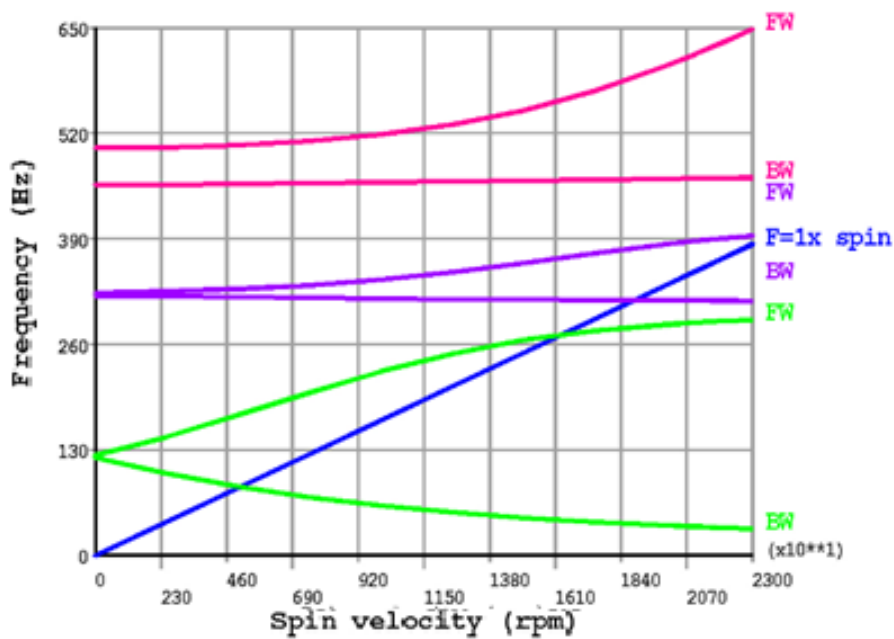
Figure 5.25.   Campbell diagram of hybrid shaft [ST, 90, 45, -45, 0_6, 90, ST]

From the tabulated results it can be observed that the critical speeds and the associated strain energy of hybrid composite material shaft are in between the values of steel and composite material shaft. Hence the hybrid composite material shaft can be used strategically to place the critical speeds according to the operating speed and vibration response of the rotor-bearing system.

5.4 Experimental Characterization

The test coupons of laminate configurations given in Table 5.26 were fabricated as per the fabrication steps of section 4.5.1.

Table 5.26.   Details of test coupons with laminate sequences

Sl. No.	AL- Aluminum sheet-1 mm, CE- carbon-epoxy, ST-Steel sheet – 1 mm		Thickness (mm)
1	CE1	CE (90, 45, -45, 0_6, 90)	4
2	CE2	CE (45, -45, 90, 0_4, -45, 90, 45)	4
3	CE3	CE (0, -45, 45, 90_6, 0)	4
4	Hybrid1	[AL, CE (90, 45, -45, 0_6, 90), ST]	6
5	Hybrid2	[AL, CE (45, -45, 90, 0_4, -45, 90, 45), ST]	6
6	Hybrid3	[ST, CE (90, 45, -45, 0_6, 90), ST]	6
7	Hybrid4	[ST, CE (45, -45, 90, 0_4, -45, 90, 45), ST]	6
8	Hybrid5	[ST, CE (0, -45, 45, 90_6, 0), ST]	6
9	Hybrid6	[AL, CE (90, 45, -45, 0_6, 90), AL]	6

The CE1 is a carbon-epoxy composite material laminate of layup sequence [90, 45, -45, 0_6, 90] selected based on the numerical analysis. CE2 is a carbon-epoxy composite material laminate of an arbitrary layup sequence [45, -45, 90, 0_4, -45, 90, 45]. CE3 is a carbon-epoxy composite material laminate which was cut in the perpendicular direction of the CE1 laminate to have an orthogonal layup sequence of CE1.

Hybrid1 and Hybrid2 are made of CE1 and CE2 laminates respectively sandwiched by aluminum and steel primarily for the bearing housing application.

Hybrid3 and Hybrid4 are made of CE1 and CE2 laminates respectively sandwiched by steel on both sides. Hybrid5 is made of CE3 sandwiched by steel on both sides. Hybrid6 is made of CE2 sandwiched by Aluminum on both sides.

The test coupons were cut to the required dimensions using the water jet cutting. Before carrying out the test, each test coupon was cured at 120°C for four hours in a heating furnace and brought back to room temperature by placing them in the room temperature for about a week.

5.4.1 Mechanical Characterization

Five test coupons of each test specimen listed in Table 5.26 were subjected to tensile and flexural tests as per the respective ASTM standards. For the tensile test, the test specimen of dimensions 25 mm width and 250 mm length and tabbed at each end were used. For the 3-point flexural test, the test specimen of dimensions 13 mm width and 180 mm length were used. The test coupons as per the required dimensions were cut using the water jet cutting. Some of the test coupons used are shown in Figure 5.26.

(a)

(b)

(c)
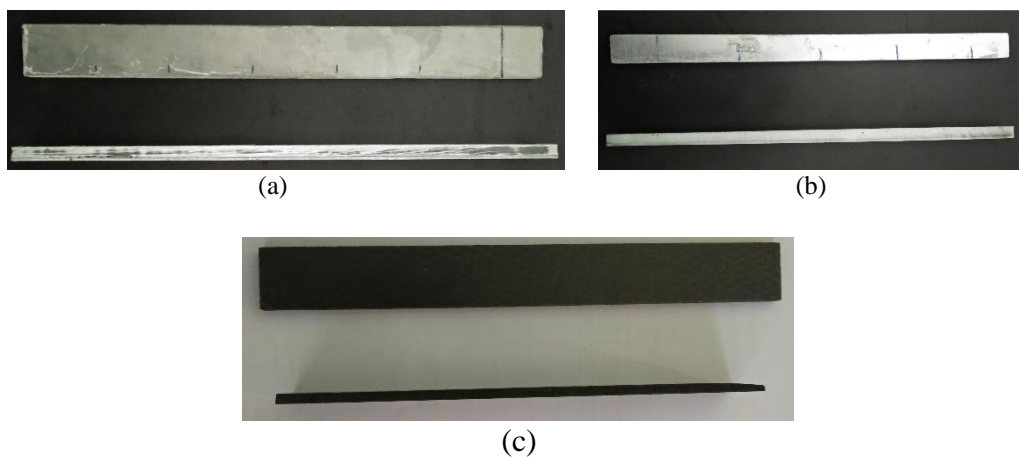
Figure 5.26.   (a) Hybrid Tensile (b) Hybrid Flexure (c) Carbon-epoxy test coupons

The average test results of five sets of test samples obtained from the tensile and flexure tests are tabulated in Table 5.27 and Table 5.28. The maximum tensile and flexural stress plots are shown in Figure 5.28 and Figure 5.29 respectively. The CE1 carbon-epoxy laminate exhibits better tensile and flexural strengths compared to CE2 and CE3 laminates. From both the tensile and flexure test results, it is evident that Hybrid3 exhibits higher tensile and flexure strengths in comparison to Hybrid4 and Hybrid5 due to the composite material layer sequence of CE1. The tensile strength of hybrid composite materials of Hybrid3, Hybrid4, and Hybrid5 were found to be higher than the corresponding carbon-epoxy laminates of CE1, CE2, and CE3. However, the flexural strength of Hybrid3, Hybrid4, and Hybrid5 were found to be slightly lower than the carbon-epoxy laminates CE1, CE2, and CE3.

Hence based on the tensile and flexure tests CE1 and Hybrid3 material were found to have the best mechanical strength characteristics.

Table 5.27.   Tensile test results

Coupon	Tensile strength (MPa)	Max Strain (%)	Applied Force (kN)
CE1	562.97	7.17	24.93
CE2	397.60	6.37	21.93
CE3	235.17	6.23	14.00
Hybrid1	461.97	5.08	75.06
Hybrid2	374.40	4.22	60.82
Hybrid3	615.63	4.92	99.93
Hybrid4	460.43	4.01	74.79
Hybrid5	313.80	3.48	40.57
Hybrid6	409.45	5.28	66.23

Table 5.28.   Flexure test results

Coupon	Flexure strength (MPa)	Max Strain (%)	Applied Force (kN)
CE1	565.03	1.02	0.94
CE2	333.37	1.27	0.77
CE3	243.63	1.07	0.69
Hybrid1	251.74	2.87	1.39
Hybrid2	207.63	3.31	1.14
Hybrid3	522.30	2.19	2.88
Hybrid4	264.30	0.99	1.46
Hybrid5	219.20	1.55	0.77
Hybrid6	127.9	4.16	0.72

The scanning electron microscope (SEM) display of the deformed specimen of Hybrid3 is shown in Figure 5.27 shows regions of cracks after the tensile and flexural tests.
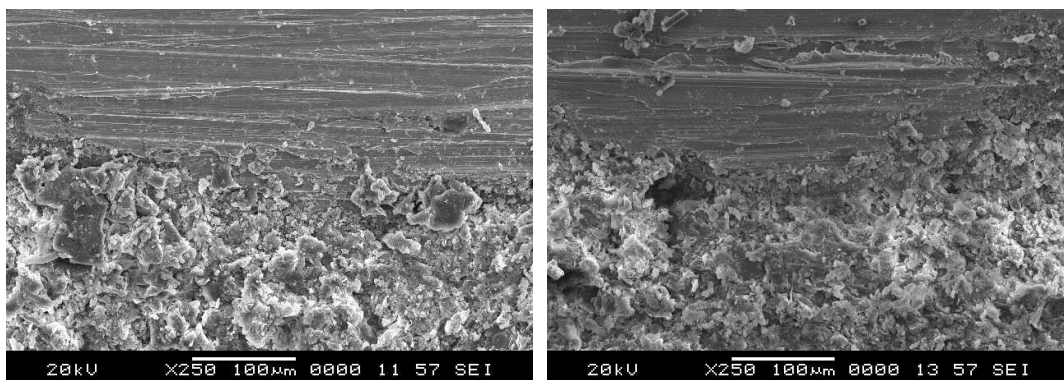

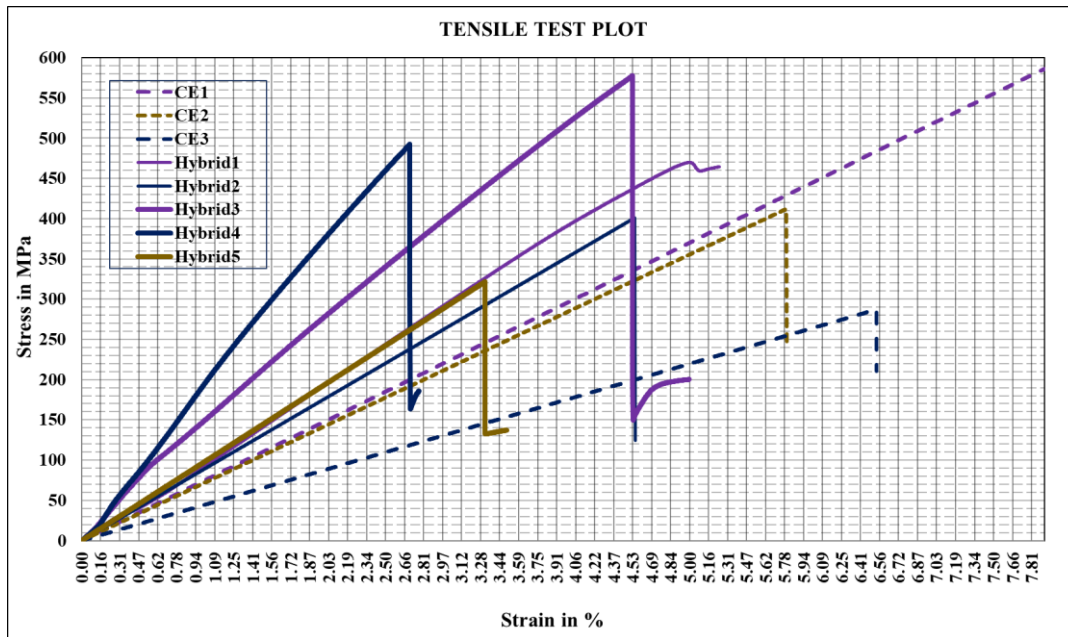Figure 5.27.   SEM image-Hybrid3 specimen after the tensile and flexure tests

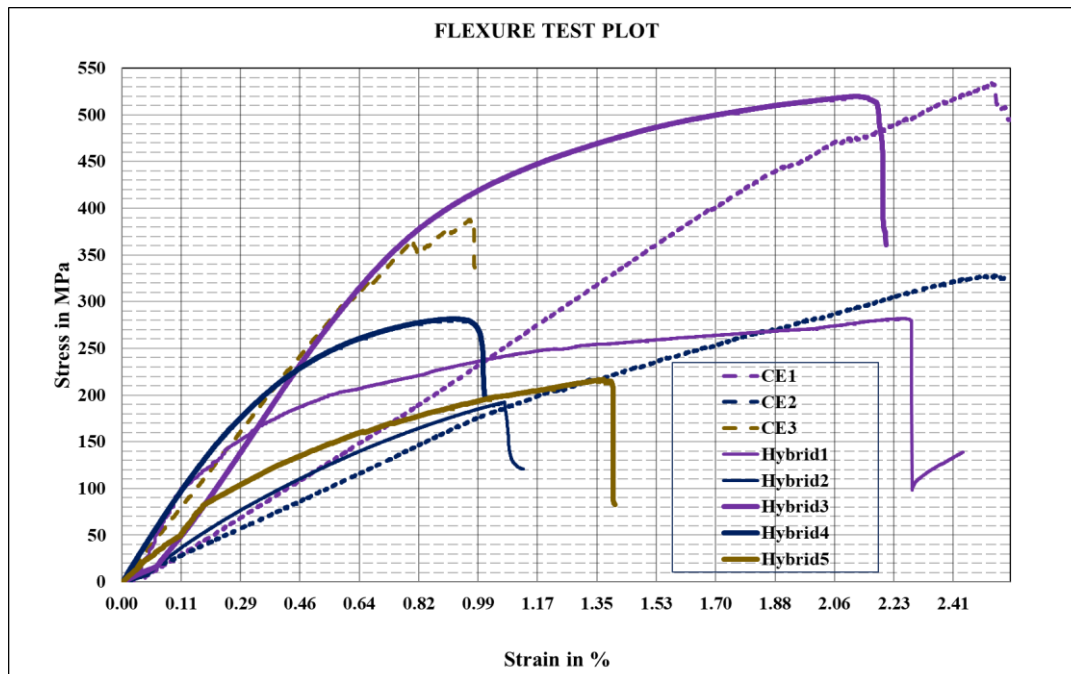Figure 5.28.   Tensile strength of Hybrid3 material

Figure 5.29.   Flexural strength of Hybrid3 material

5.4.2 Damping Estimation of Cantilever Beam

The damping estimation of cantilever beam samples was carried out as per the test procedure explained in section 4.5.3.1. The dimensions and the numerically estimated natural frequencies of the test specimen are given in Table 5.29. In addition to the test coupons of Table 5.26, the test coupon of aluminum material was also tested for the calibration of the test setup as per the requirement of test standard (ASTM D756–05, 2017).

Table 5.29.   Natural frequencies of test coupons

Sl. No.	Specimen	Length (mm)	Width (mm)	Mass (gm)	Frequency (Hz)	
					Mode I	Mode II
1	Aluminum	240	25	102.6	83	524
2	CE1	180	20	23	145	930
3	CE2	180	20	23	115	725
4	CE3	180	20	23	135	845
5	Hybrid1	180	13	36.9	155	888
		230	25	88.3	88	580
6	Hybrid2	180	13	36.9	156	910
		230	25	88.3	89	598
7	Hybrid3	180	13	50.4	183	983
		230	25	119.6	100	657
8	Hybrid4	180	13	50.4	155	980
		230	25	119.6	103	665
9	Hybrid5	180	13	50.4	160	962
		230	25	119.6	98	642
10	Hybrid6	180	13	25.2	180	1100
		230	25	63	94	572

To verify that the response peeks considered for the damping estimation were of the first two lateral modes, each test coupon was divided into five equal zones. By keeping the accelerometer fixed at the free end, the test specimen was excited at every five zones starting from the fixed end to the free end. The experimental modal frequency values were found to be very close (within ±2%) to the numerical result. The loss factor (η) and equivalent proportional viscous damping values (β) of all the test specimens were obtained using half-power frequency bandwidth (3 dB method) and logarithmic decrement as tabulated in Table 5.30. Among the carbon-epoxy laminates, CE1 is

having the least loss factor. However, among the hybrid combinations, the damping values are found to be almost the same with minor variations. The frequency response function (FRF), the frequency spectrum, and the logarithmic decrement plots of Hybrid3 specimen are shown in Figure 5.30, Figure 5.31 and Figure 5.32 respectively.

Table 5.30.   Experimental Damping values of beam specimen

| Specimen	Mode I		Mode II		ξ (LD)	E, Young's Modulus (N/mm^2)
	η (LF)	β (s)	η (LF)	β (s)		
Aluminum	0.004	1.5E-5	0.003	1.9E-6	0.0019	67E9
CE1	0.038	1.3E-4	0.028	9.6E-6	0.022	47E9
CE2	0.042	1.41E-4	0.026	9.4E-6	0.024	30E9
CE3	0.045	1.43E-4	0.029	9.7E-6	0.025	42E9
Hybrid1	0.0223	4.6E-5	0.0144	4.9E-6	0.012	73E9
	0.014	5.2E-5	0.009	5.5E-6	0.011	60E9
Hybrid2	0.019	3.9E-5	0.0126	4.4E-6	0.0115	73E9
	0.0209	7.4E-5	0.0147	8.7E-6	0.011	63E9
Hybrid3	0.0207	3.5E-5	0.01	3.1E-6	0.01	147E9
	0.0157	5.0E-5	0.008	5.5E-6	0.09	105E9
Hybrid4	0.014	2.8E-5	0.011	3.6E-6	0.008	98E9
	0.0207	6.4E-5	0.0101	4.7E-6	0.01	112E9
Hybrid5	0.021	3.1E-5	0.0118	3.9E-6	0.011	157E9
	0.017	4.9E-5	0.0104	4.5E-6	0.018	141E9
Hybrid6	0.013	2.7E-5	0.01	2.1E-6	0.01	50E9
	0.01	3.4E-5	0.01	2.7E-6	0.01	49E9
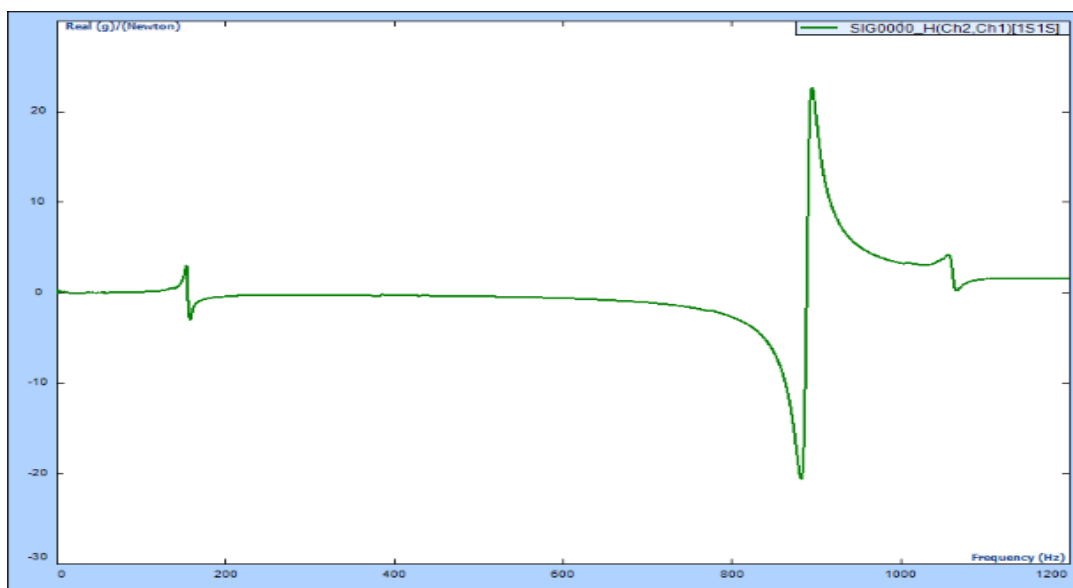
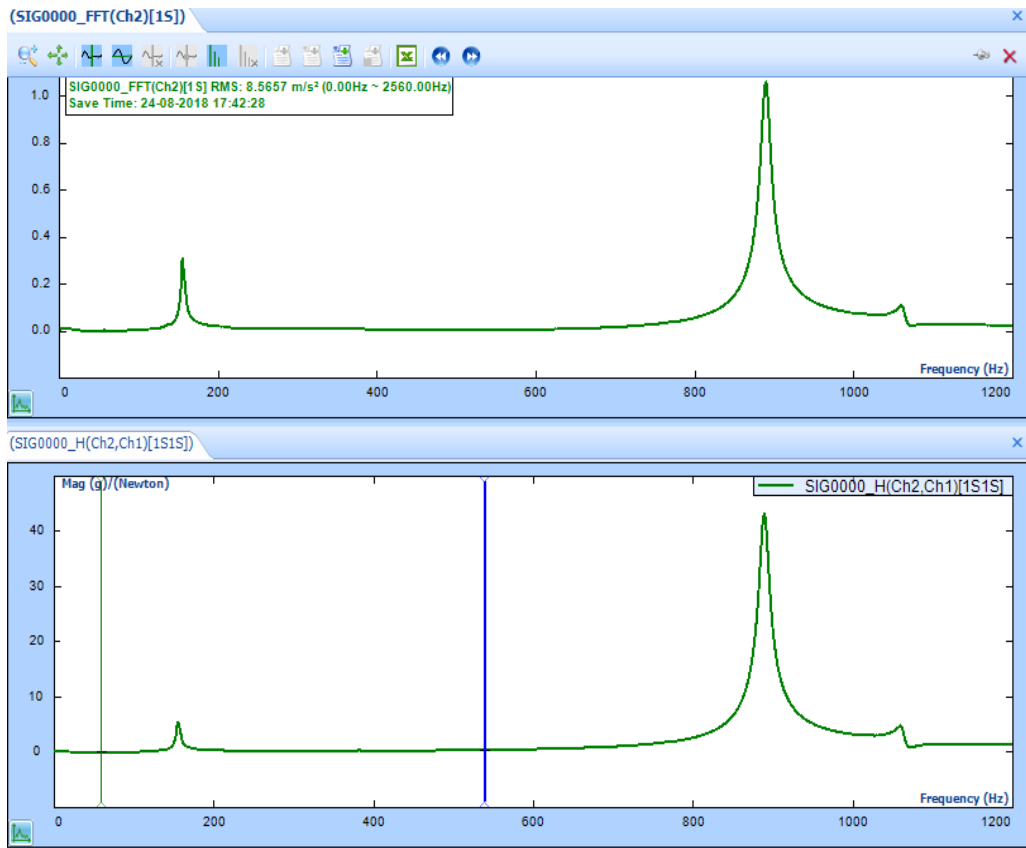Figure 5.30.   Frequency Response Function of Hybrid3

Figure 5.31. Response (Impact response v/s frequency) of Hybrid3
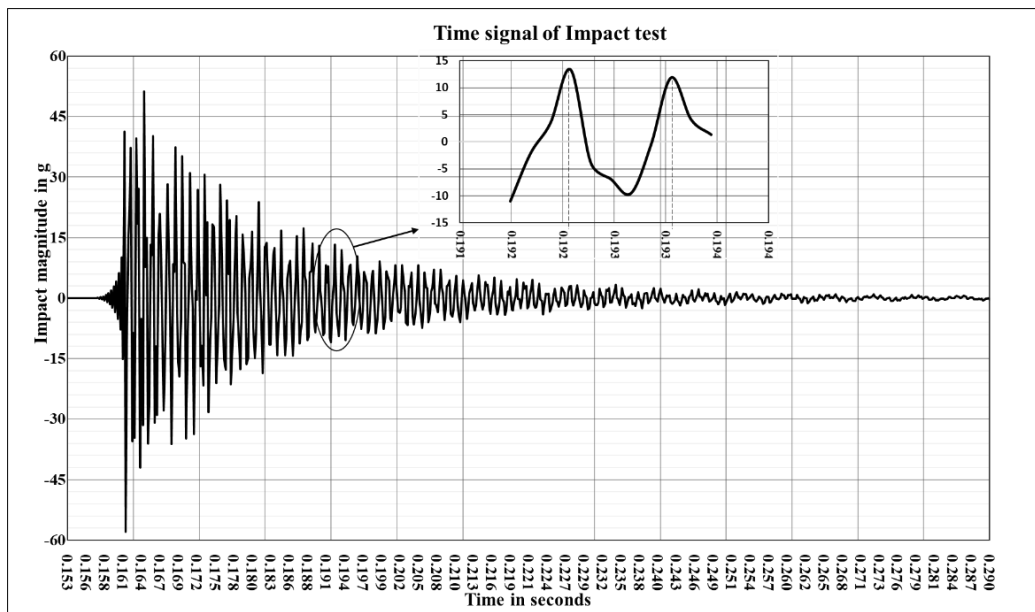

Figure 5.32. Logarithmic decay (Impact response v/s time) of Hybrid3

5.4.3 Dynamic Mechanical Analysis (DMA)

For each test specimen given in Table 5.26, the dynamic mechanical analysis was carried out as per the test procedure given in section 4.5.3.2. The test coupons were cut as per the dimensions of 55 mm length and 13 mm width required by the DMA test equipment using the water jet cutting. Before the testing, the test coupons were post cured at 120°C in a furnace for four hours and were kept at room temperature for about a week. The temperature profile from ambient temperature to the maximum temperature of 200ºC was swept at a constant excitation frequency of 1 Hz at a constant amplitude of 10 microns.

The storage modulus and loss factor values of CE1, CE2, CE3 laminates are compared in Figure 5.33 and the prominent results are tabulated in Table 5.31. It is evident from both Figure 5.33 and Table 5.31, CE1 is having higher stiffness in terms of the storage modulus though the loss factor values are almost the same. The softening temperature of all the three laminates are found to be the same at 66ºC. However, the glass transition temperature of the three laminates slightly varies with the CE1 at 132ºC. Hence from DMA, it is found that the CE1 is better suited to the rotating shaft application in comparison to the CE2. The CE3 laminate was tested to evaluate the orthogonal viscoelastic characteristics of CE1.
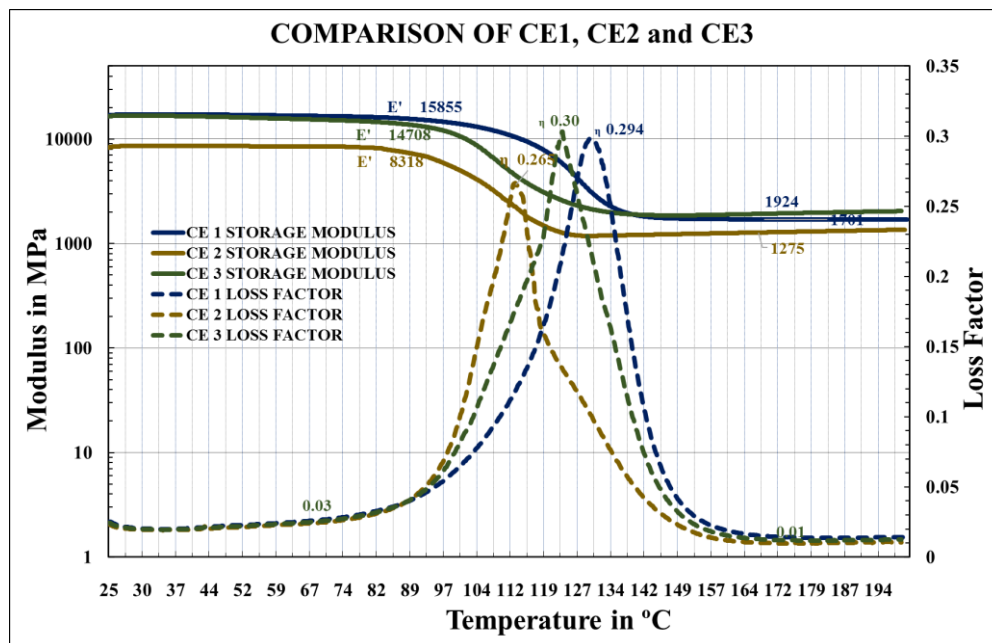
Figure 5.33.   Storage Modulus and Loss Factor of CE1, CE2, CE3

Table 5.31.   DMA Test results of Carbon-epoxy laminates

	Parameters	Unit	CE1	CE2	CE3
Transition region	Softening temperature, T_s	℃	66	66	66
	Loss factor, LF	-	0.024	0.025	0.025
	Storage modulus, SM	MPa	15855	8318	14708
	Glass transition temperature, T_g	℃	132	118	126
	Loss factor, LF	-	0.294	0.209	0.303
	Storage modulus, SM	MPa	2950	4691	3216
Rubbery region	Maximum applied temperature, T_m	℃	200	200	200
	Loss factor, LF	-	0.012	0.012	0.012
	Storage modulus, SM	MPa	1924	1275	1701

The DMA test results of hybrid of steel, carbon-epoxy, aluminum laminates Hybrid1 and Hybrid2 are shown in Figure 5.34. Similarly, in Figure 5.35 the DMA results of hybrid of steel, carbon-epoxy, steel laminates Hybrid3, Hybrid4, and Hybrid5 are plotted. The DMA results of hybrid of aluminum, carbon-epoxy, aluminum laminate Hybrid6 is shown in Figure 5.36.

Figure 5.34.   Storage Modulus and Loss Factor of Hybrid1 and Hybrid2

Figure 5.35.   Storage Modulus and Loss Factor of Hybrid3, Hybrid4, and Hybrid5

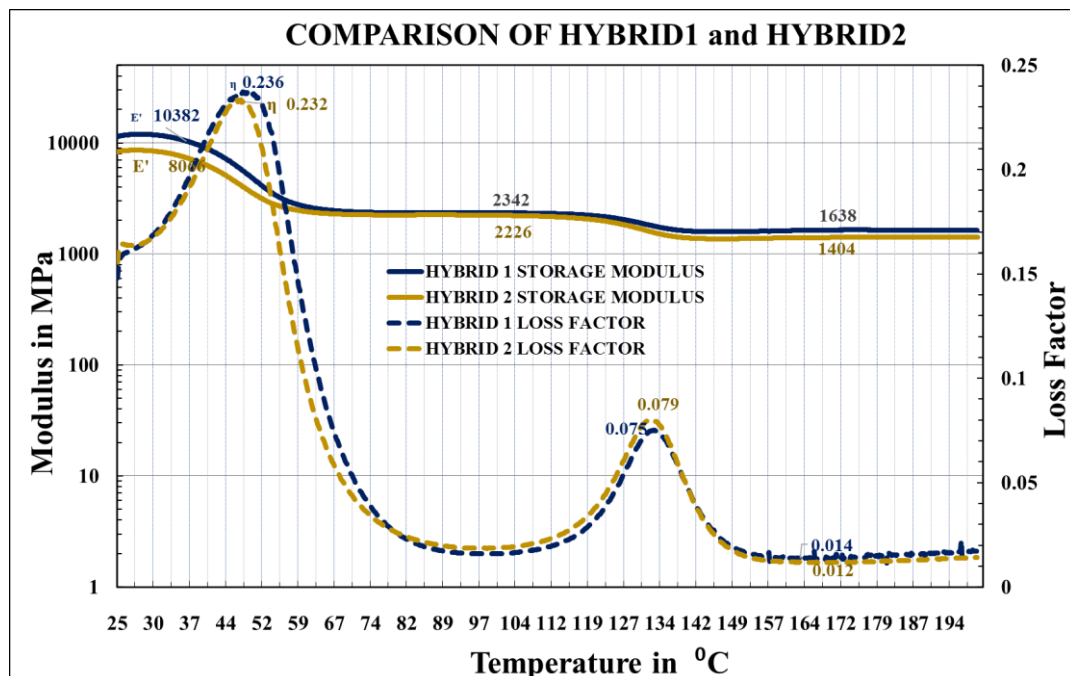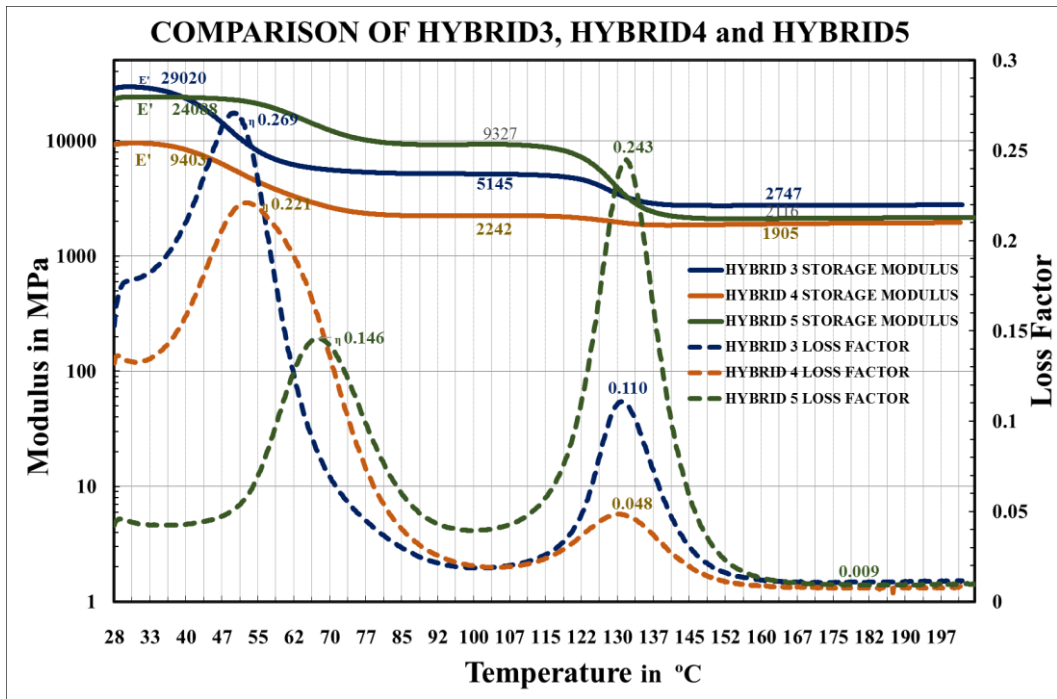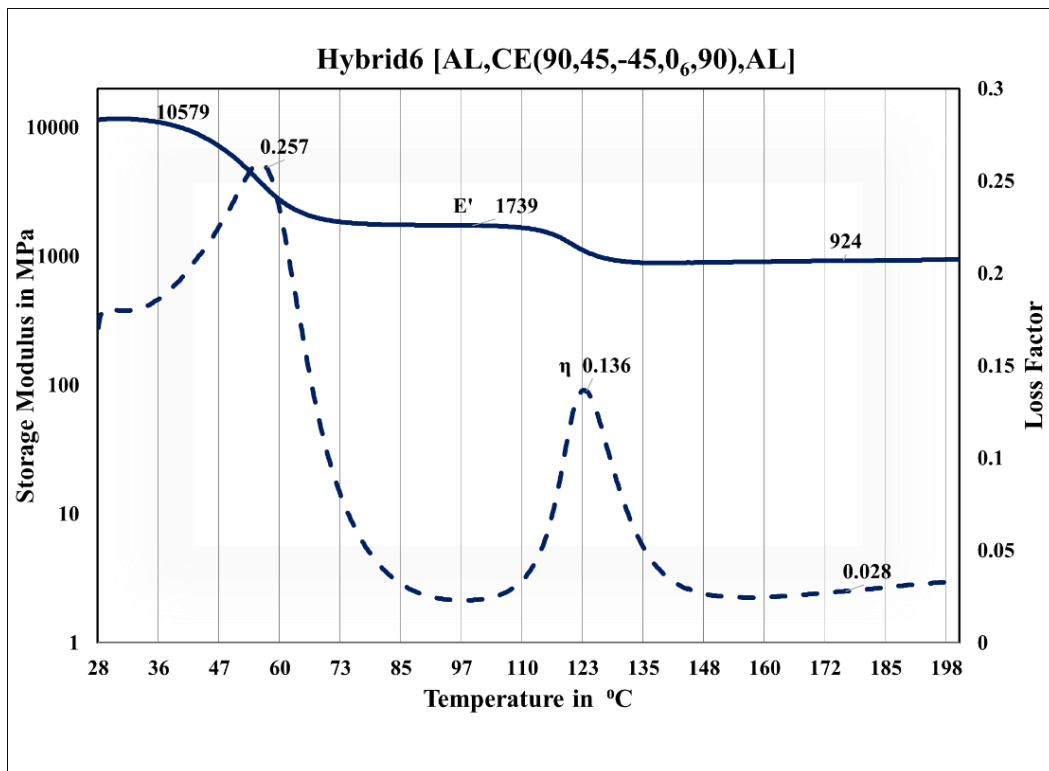
Figure 5.36.   Viscoelastic behavior of Hybrid6 at 1 Hz

From the dynamic mechanical analysis of all the hybrid laminates, the prominent values of storage modulus, loss factor and the transition temperatures are tabulated as shown in Table 5.32.

Table 5.32.   DMA Test results of hybrid material laminates

Parameters		Unit	Hyb1	Hyb2	Hyb3	Hyb4	Hyb5	Hyb6
Transition 1 region	T_s	ºC	32	32	37	37	37	32
	LF	-	0.17	0.17	0.19	0.14	0.04	0.17
	SM	MPa	10382	8066	29290	9408	24088	10579
	T_g	ºC	50	50	50	51	63	55
	LF	-	0.236	0.232	0.269	0.221	0.146	0.257
	SM	MPa	5665	3950	10970	4625	12606	3450
Transition2 region	T_s	^{0} C	105	105	105	105	105	105
	LF	-	0.017	0.19	0.02	0.021	0.04	0.026
	SM	MPa	2342	2226	5145	2242	9327	1739
	T_g	ºC	132	132	132	132	132	125
	LF	-	0.075	0.079	0.11	0.048	0.243	0.14
	SM	MPa	1700	1490	3070	1956	3025	924
Rubbery region	T_m	ºC	200	200	200	200	200	200
	LF	-	0.014	0.012	0.009	0.009	0.009	0.03
	SM	MPa	1638	1404	2747	1905	2116	920

From Figure 5.34 and the corresponding values from Table 5.32, it is evident that among the two carbon-epoxy laminates sandwiched between steel and aluminum, Hybrid1 is found to have a slightly better stiffness though the loss factor values are more or less same. The hybrid composite material sandwich laminates were found to have two glass transition temperatures due to the additional adhesive bond between the carbon-epoxy laminate and the metal. The first softening temperature of both laminates was found to be the same at 32ºC and the first glass transition temperature was at 50ºC. The second softening temperature of both laminates was found to be the same at 105ºC and the second transition temperature was at 132ºC. As Hybrid1 and Hybrid2 are analyzed for the bearing housing requirement which operates within the I transition, Hybrid1 has a slight edge over the Hybrid2 in terms of the stiffness.

From Figure 5.35 and the corresponding values from Table 5.32, it is evident that among Hybrid3, Hybrid4 and Hybrid5, Hybrid3 is found to have the best stiffness at the operating temperature range of power turbine shaft at 75ºC to 120ºC. The second

softening and transition temperatures of all three laminates were found to be the same at 105ºC and 132ºC respectively. By considering the operating temperature range of 75ºC to 120ºC, Hybrid3 is best suited for the rotating shaft application. It was also found that Hybrid5 exhibits the near orthogonal damping behavior in comparison to the Hybrid3 laminate.

From the plot in Figure 5.34, it is evident that for the Hybrid6 carbon-epoxy laminate sandwiched between the aluminum sheet, the viscoelastic behavior is similar to the Hybrid1 laminate till the transisiton1 region. The Hybrid6 laminate becomes soft as the modulus reduces and the loss modulus increases in the rubbery region.

Further, for the Hybrid3 sample, the dynamic mechanical analysis at 15 Hz and 30 Hz was carried out to analyze the damping behavior with an increase in the frequency with all the other parameters kept at the same level as shown in Figure 5.37.
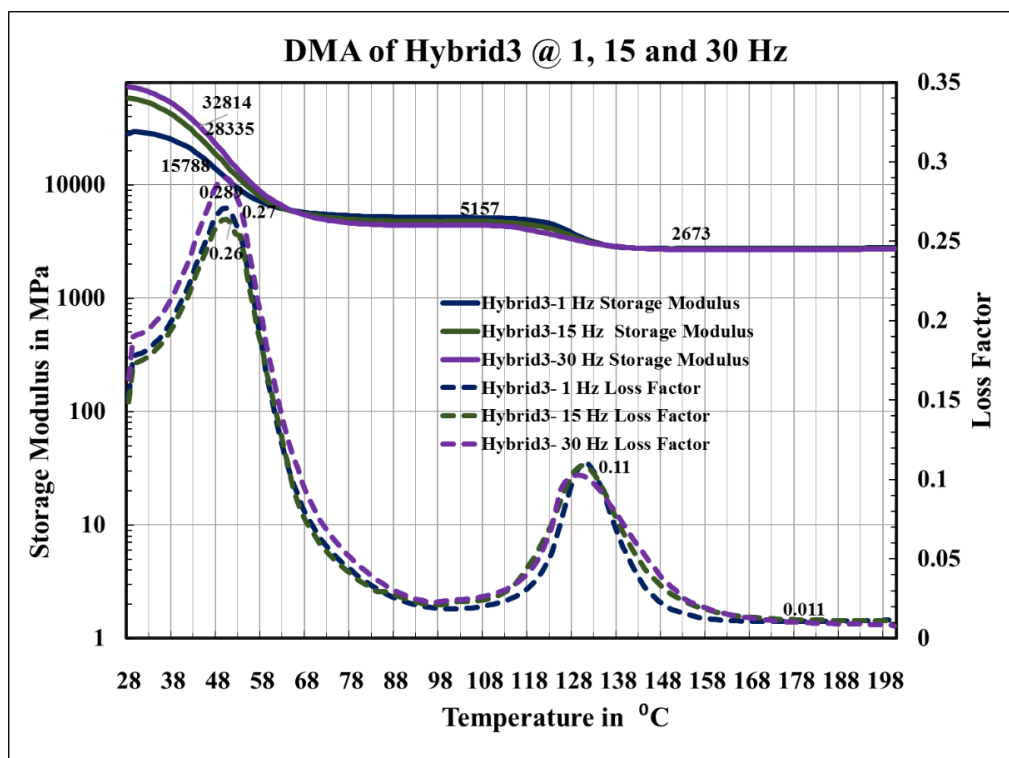

Figure 5.37.   Viscoelastic behavior of Hybrid3 at 1 Hz, 15 Hz & 30 Hz

As shown in Figure 5.37, within the first transition temperature, the increase in the frequency increases both the stiffness (storage modulus) and the loss factor (loss modulus) of Hybrid3. After the first transition temperature till the second transition

temperature reached, the increase in frequency reduces the stiffness and damping of Hybrid3. However, after the second transition temperature, the increase in frequency is not having much of an effect on the dynamic characteristics of the Hybrid3 material as both the stiffness and damping values remain the same. Since at the operating temperature of 75ºC to 120ºC the stiffness and damping remain almost the same for all the three frequencies, the variation of frequency effect on the Hybrid3 may be ignored.

5.4.4 Damping Estimation of Tubular Shaft

Based on the numerical results, mechanical characterization and damping estimation tests of beam samples carried out, for achieving the higher shaft critical speed (natural frequencies) and lower damping values, Hybrid3 material of carbon epoxy composite sandwiched between steel [ST, CE (90, 45, -45, 0_6, 90), ST] was selected for the fabrication of the tubular test specimen. The frequency response and logarithmic decay of the Hybrid tubular specimen excited by the impact hammer are shown in Figure 5.38 and Figure 5.39 respectively. The damping values of the tubular specimens estimated from the free vibration test are presented in Table 5.33.
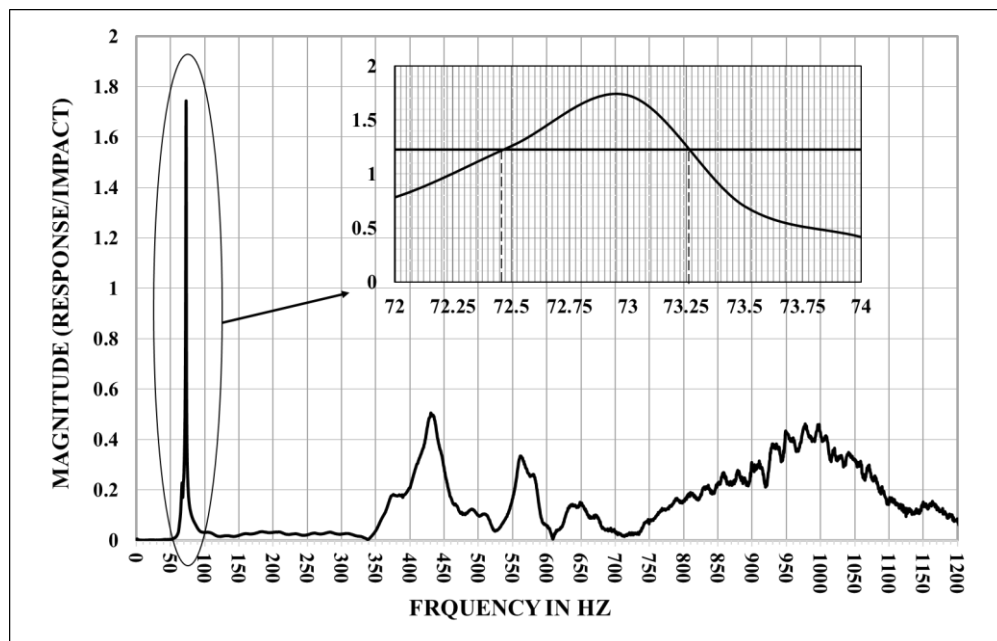

Figure 5.38.   The Impact Frequency response of Hybrid tube
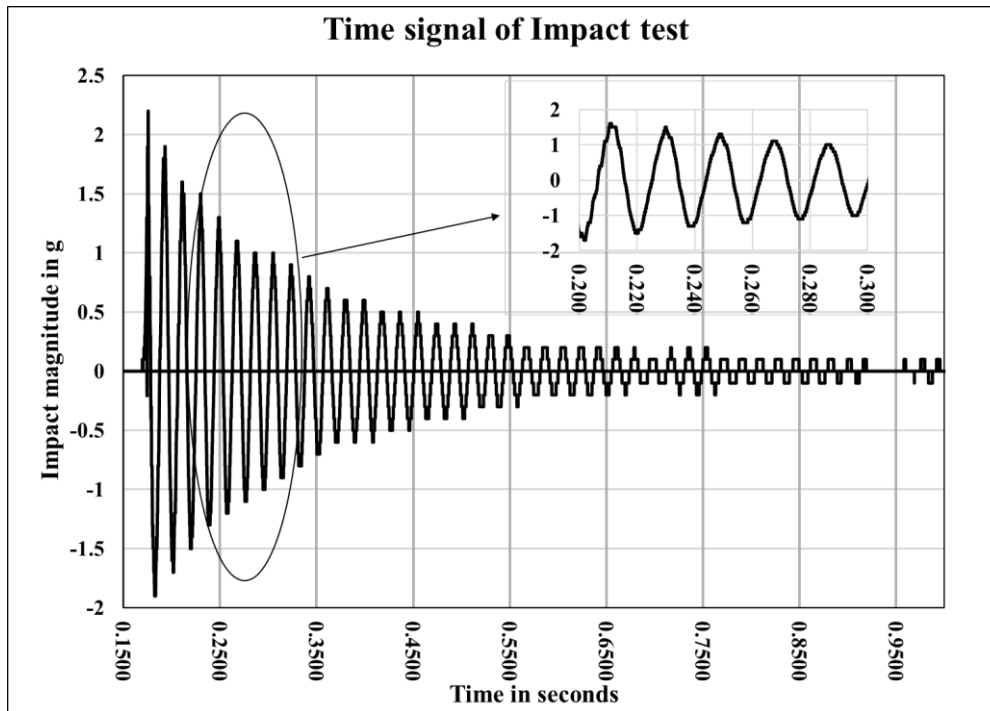
Figure 5.39.   Logarithmic decay (Impact response v/s time) of Hybrid tube

Table 5.33.   Experimental damping values of tube specimen

Specimen	Mode I		Mode II		Damping ratio (LD)
	Freq (Hz)	LF	Freq (Hz)	LF	
Outer Steel tube	75	0.005	490	0.007	0.003
Carbon/epoxy tube	62	0.029	480	0.018	0.015
Hybrid tube	73	0.014	430	0.008	0.009

5.4.5 Model Updating of Damping

A preliminary model updating methodology adopted for updating damping in the cantilever beams is shown in Figure 5.40. Based on this, a more precise modal updating using the component mode synthesis to be implemented for damping updation in the rotating shaft. In this preliminary model, Hybrid6 composite material beam made up of carbon-epoxy composite material laminate sandwiched by aluminum was selected for the model updating. The eigenvalues and eigenvectors were identified by the finite element analysis. An initial damping value was assumed for the evaluation of finite element response followed by the experimental free vibration tests for the FRF data and dynamic mechanical analysis for evaluating the viscoelastic characteristics. The modal testing in the cantilever mode was used to generate the experimental data of logarithmic

110

decrement and frequency response function. Similarly, the viscoelastic material properties of the hybrid6 obtained using TA DMA 800 dynamic mechanical analyzer. The Rayleigh damping constant of stiffness matrix proportional damping constant β was calculated based on the loss factor values extracted from the DMA experimental data.
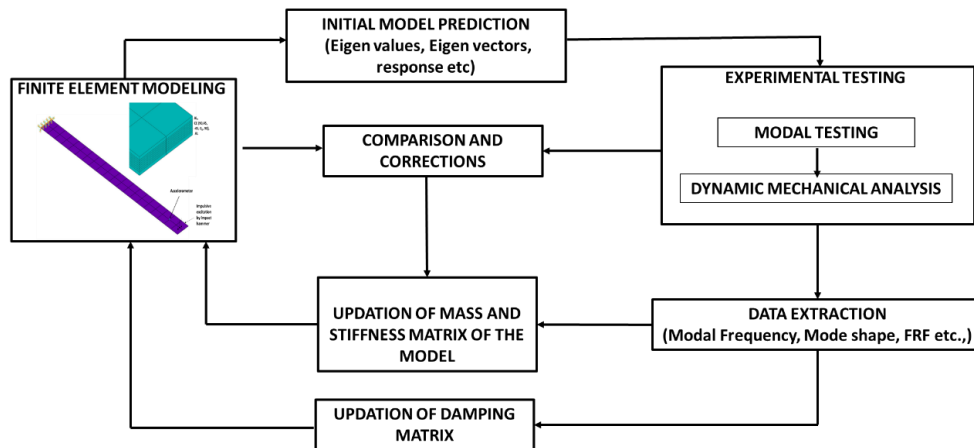
Figure 5.40.   Typical Model updating methodology

The damping updation of the two bending mode shapes of hybrid6 shown in Figure 4.19 and tabulated in Table 5.29 is presented in this section. For the effective updating methodology, QR algorithm of the QR Damped method was used instead of the conventional reduced method to extract and calculate the complex eigenvalues of the resulting quadratic eigenvalue problem in the modal subspace. Using the modes extracted in the modal analysis, the transient logarithmic decrement and harmonic response analysis were carried out by assuming an initial damping ratio of 0.01. The estimated finite element transient and harmonic response plots are shown in Figure 5.41 and Figure 5.42.   The finite element damping model updating was performed using the damping data of Hybrid6 from the free vibration test and viscoelastic material data extracted from the DMA. The experimental storage modulus, loss modulus, and loss factor values were incorporated in the finite element numerical model as an experimental Prony series data. The frequency response of numerical models using damping values from modal testing and the dynamic mechanical analysis were compared for the modal assurance criteria (MAC) and signature assurance criteria (SAC) as shown in Figure 5.43.

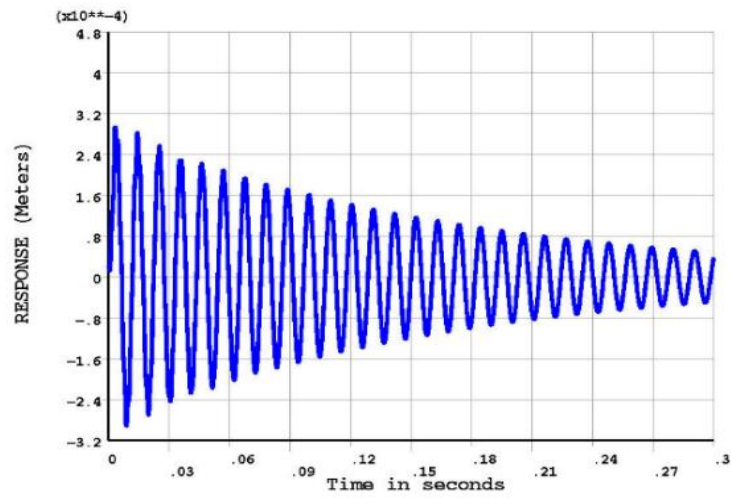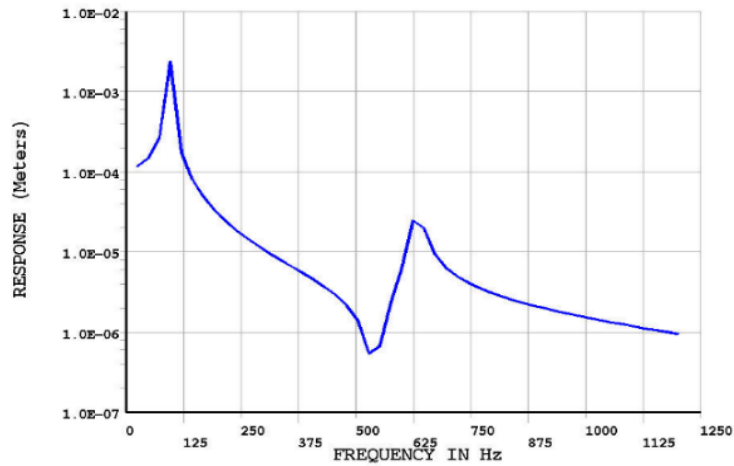Figure 5.41.   Transient response due to impact excitation

Figure 5.42.   Frequency response due to impact excitation
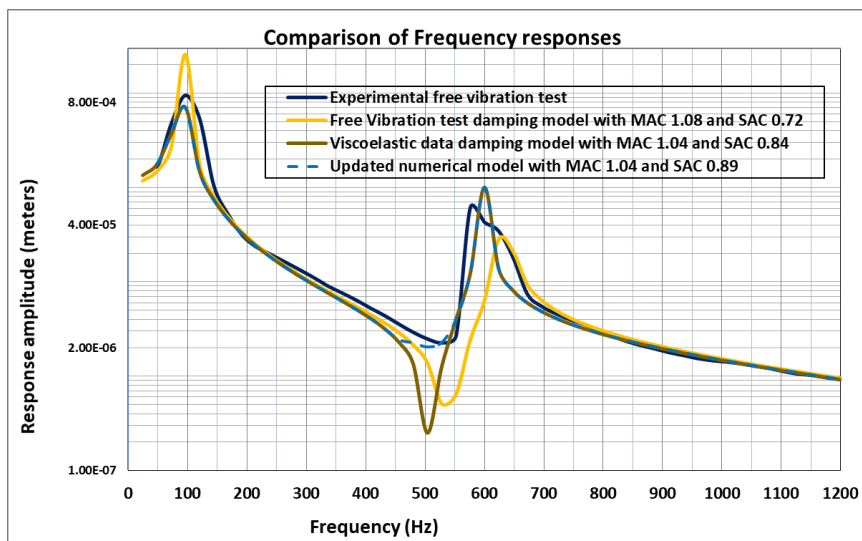
Figure 5.43.   Frequency response comparison

CHAPTER 6

6 HYBRID SHAFT ROTOR-BEARING SYSTEM

In this chapter, the power turbine shaft is remodeled using the numerical and experimental test results carried out in the previous sections. The rotor dynamic stability analysis for a set of combinations of hybrid composite shaft made of hybrid3 material which was evaluated as the most appropriate material is also presented.

The schematic of the power turbine high-speed rotor-bearing system is shown in Figure 6.1. Two pairs of bearings support the rotating system with one end over hanged by two-stage turbine rotors are represented by the Kelvin-Voight spring-damper model.
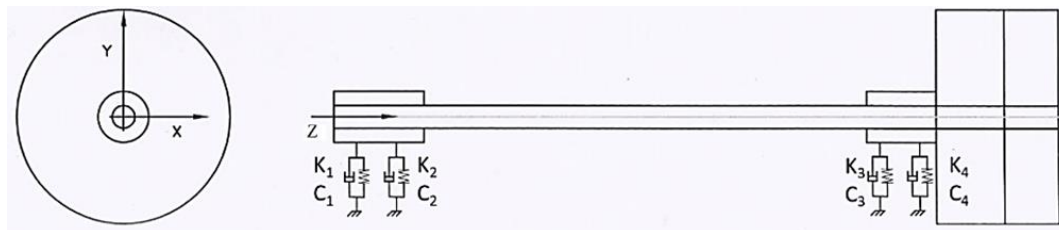
Figure 6.1.   High-speed power turbine rotor-bearing system

Even though the composite material was proposed within the bearing span of 560 mm, the hybrid material tube length may be reduced to 500 mm to provide an additional margin of 60 mm from the hot section. The Tubular hybrid3 material of carbon epoxy laminate sandwiched by the steel tubes made up of 1.5 mm to 1 mm thickness and ten layers of composite layers made of carbon-epoxy of layer sequence $[90, 45, -45, 0_6, 90]$ was considered for the detailed rotor dynamic analysis.

Analysis of four combinations of the hybrid shaft, two carbon-epoxy, and the existing steel shaft as per Table 6.1 is presented in this chapter. The outside diameter of the outer steel tube of the hybrid material is fixed at 25 mm. The 16-layer carbon-epoxy shaft with the layer stacking sequence of $[90, 45, -45, 0_{12}, 90]$ was used considering the actual layer thickness of 0.4 mm as against the 0.5 mm thickness used in the initial numerical analysis.

Table 6.1.   Details of hybrid shaft (all dimensions in mm)

Sl. No.	Type	Composition	Thickness
1	ST	Existing solid steel shaft	-
2	CE-560	16-layer carbon/epoxy laminate in 90, 45, -45, 0_{12}, 90 sequence. (560 and 500 stands for length of hybrid/composite shaft)	5 mm
3	CE-500		
4	HYB1-560	Carbon/epoxy laminate of 10 layers in 90, 45, -45, 0_6, 90 sequence inside steel tubes of each 1 mm thickness	6 mm
5	HYB1-500		
6	HYB2-560	Carbon/epoxy laminate of 10 layers in 90, 45, -45, 0_6, 90 sequence inside steel tubes of each 1.5 mm thickness	7 mm
7	HYB2-500		

6.1 Modal Analysis

The modal analysis was carried out to estimate the natural frequencies of the first three lateral modes of the power turbine rotor-bearing system as shown in Figure 6.2. The associated strain energies of shaft/rotors of the corresponding mode shape were also estimated. The frequency values along with the percentage strain energy in the rotating components for the three lateral modes of rotor-bearing systems of all the combinations are tabulated and compared in Table 6.2.

For all the configurations made of carbon epoxy and hybrid tubes, the frequency values of I mode are almost equal to that of the existing steel shaft rotor-bearing system. For all the configurations there is an increase in frequency values of II and III modes compared to the existing rotor-bearing system. The tabulated results indicate that for all the configurations, the II mode can be pushed beyond the operating speed. Similarly, for all the configurations under evaluation, the frequency values of the III mode increase further beyond the maximum speed.

The percentage stain energy values of both I and II modes of all the six configurations are found to have reduced in comparison to the existing configuration. The reduction in percentage strain energy value in the rotating system is an indication that there will be a reduction in shaft deformation while operating in the proximity of the critical speed. Table 6.2 also indicates the weight reduction that can be achieved by all the six configurations in comparison to the existing steel shaft.

Table 6.2.　　Comparison of modal frequency and associated strain energy values

Shaft Configuration		I, II & III Modes in Hz and strain energy (SE) in %					
Material	mass (kg)	I Mode	SE	II Mode	SE	III Mode	SE
ST	1.767	119	55	288	35	379	50
CE-560	0.277	111	41	338	6	613	85
CE-500	0.248	116	42	334	6	700	82
HYB1-560	0.725	115	46	330	9	470	83
HYB1-500	0.625	116	49	326	8	502	83
HYB2-560	0.96	117	47	324	12	445	78
HYB2-500	0.845	121	51	322	11	477	78

(a)

(b)

(c)
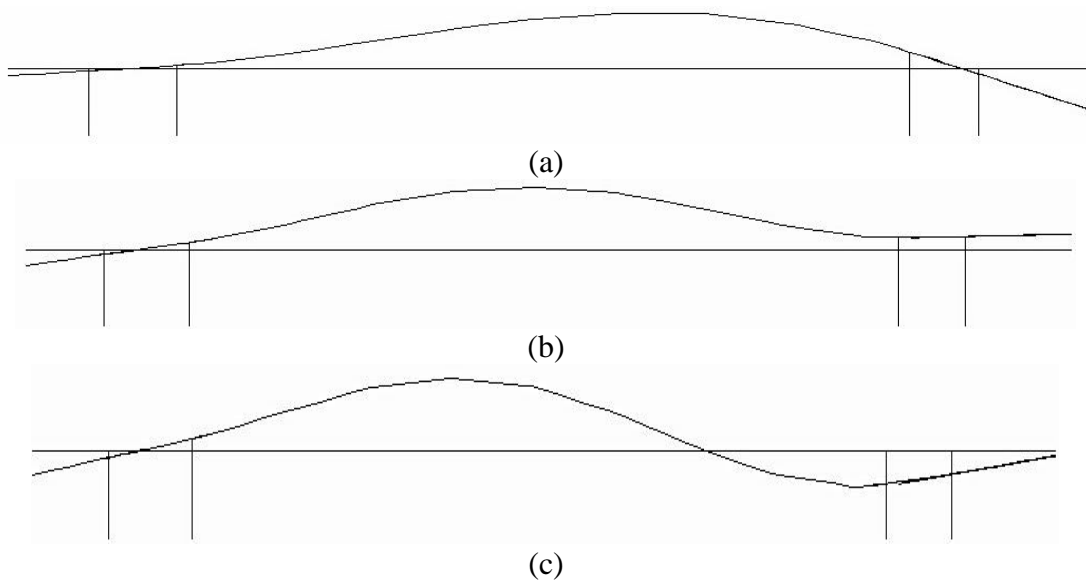
Figure 6.2.　　Lateral Mode shapes (a) I Mode, (b) II Mode (c) III Mode

6.2 Critical Speed Analysis

The critical speed analysis was carried out to estimate the critical speeds of the rotor-bearing system within the operating speed and compared with the existing system. The comparison of all the seven configurations for the first three lateral modes was analyzed using the Campbell diagrams shown in Figure 6.3, Figure 6.4 and Figure 6.5. The critical speeds of all the configurations are tabulated in Table 6.3. I Forward whirl critical speed values of all the configurations are almost the same and just marginally increases compared to the existing rotor-bearing configuration. As already indicated by the modal analysis, for all the configurations, the II forward critical speed is pushed above the operating speed with a higher margin for the CE-560/500 followed by HYB1-

500/560 and HYB2-500/560. For all the configurations the III forward critical speed increases further beyond the operating speed which would effectively reduce the flexural deformation in the shaft.
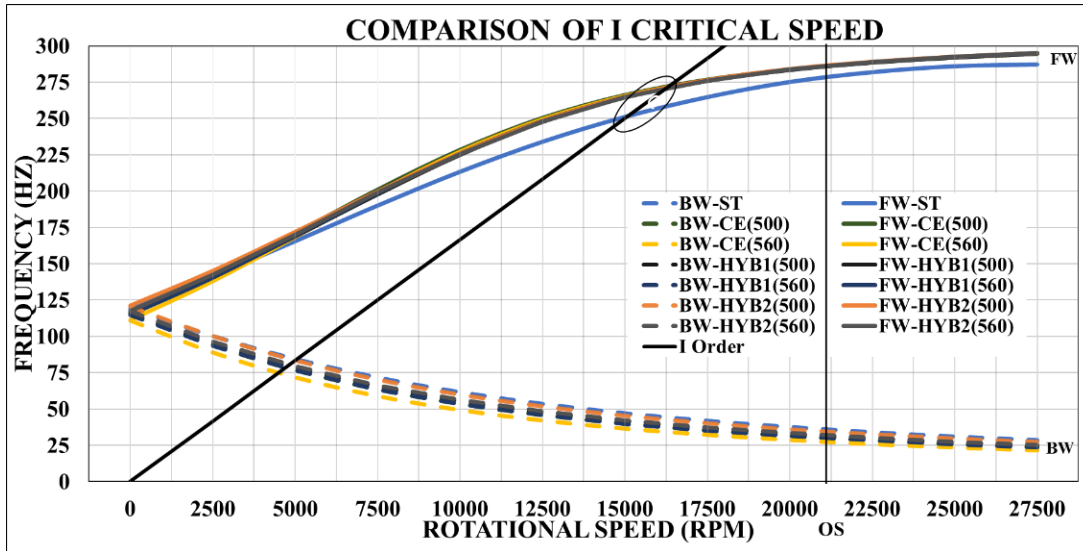
Figure 6.3.   Campbell diagram of I lateral mode
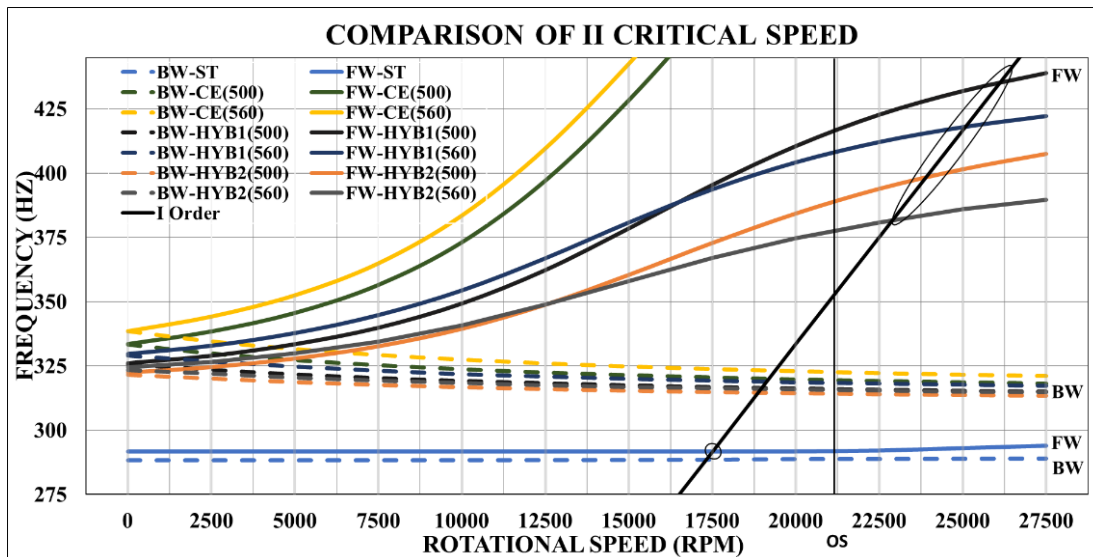
Figure 6.4.   Campbell diagram of II lateral mode
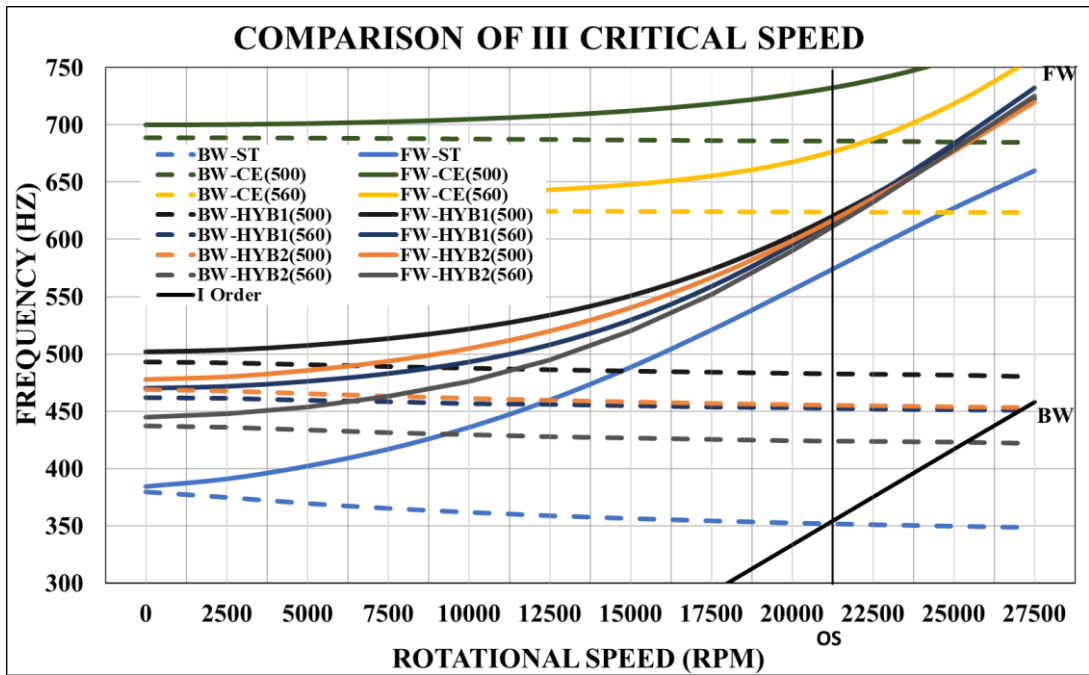
Figure 6.5.   Campbell diagram of III lateral mode

Table 6.3.   Critical speed comparisons

Configuration	BW-Backward whirl, FW-Forward whirl speeds in rpm					
	I BW	I FW	II BW	II FW	III BW	III FW
ST	5054	15025	17308	17497	21132	>27500
CE-560	4050	16156	19411	>27500	>27500	>27500
CE-500	4771	16303	19198	>27500	>27500	>27500
HYB1-560	4704	16230	19128	25079	27062	>27500
HYB1-500	4793	16246	18991	26100	>27500	>27500
HYB2-560	4829	16214	18961	22910	>27500	>27500
HYB2-500	5011	16228	18870	23887	27184	>27500

6.3 Unbalance Response Analysis

The unbalance response analysis of the rotor-bearing system was carried out to compare the responses of all the configurations of rotor-bearing systems given in Table 6.1. The response of the existing steel shaft rotor-bearing system is validated in a high-speed production test facility shown in Figure 6.6 where the deflection at the shaft center is measured using the eddy current proximity sensor. The facility is a regular production facility where the shaft deflection is measured and corrected by material removal process if the deflection is beyond the production acceptable levels. All the rotor-bearing elements such as equivalent rotor disks, bearings, and the bearing supports with

117

damping are used in the test facility to simulate the actual rotor-bearing support conditions. During the test, the operating speed was moved away from the resonance frequencies to avoid high vibrations.
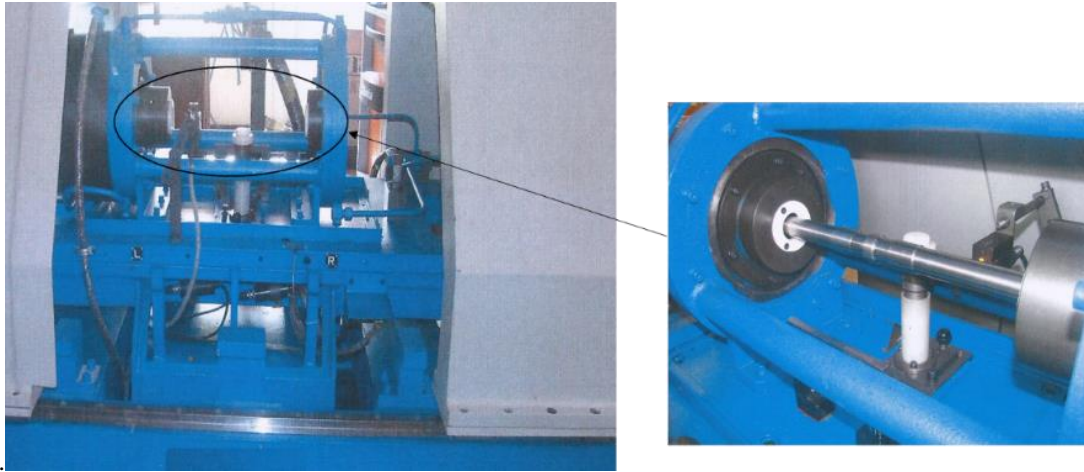
Figure 6.6.   High-speed shaft testing facility

The harmonic response of all the rotor-bearing system configurations at the shaft center due to two equal unbalance forces of 5 cmg per each plane on the two rotor disc planes are plotted in terms of displacement and bending stresses as shown in Figure 6.7 and Figure 6.8. The displacement values measured are closely matching with the numerical results of the existing system. As indicated by both the plots, for all the composite shaft rotor-bearing systems there is a drastic reduction in the displacement and bending stress values at the critical speeds compared to the existing shaft. The critical speeds, the displacement response, and bending stress values of all the configurations are presented in Table 6.4.

As evaluated from the critical speed analysis, the I forward whirl critical speed of all the hybrid composite shaft rotor-bearing systems are slightly increased in comparison to the existing system. The II forward whirl critical speed of all the hybrid composite shaft rotor-bearing systems are moved away from the operating speed. The deflections and bending stress values at the I critical speed are reduced providing additional fatigue life during the operating cycle.

Figure 6.7.   Unbalance response- comparison

Figure 6.8.   Bending stress at the center of the shaft due to unbalance

119

Table 6.4.　　　Unbalance response of deflection (δ) in microns (NM-Not measured)

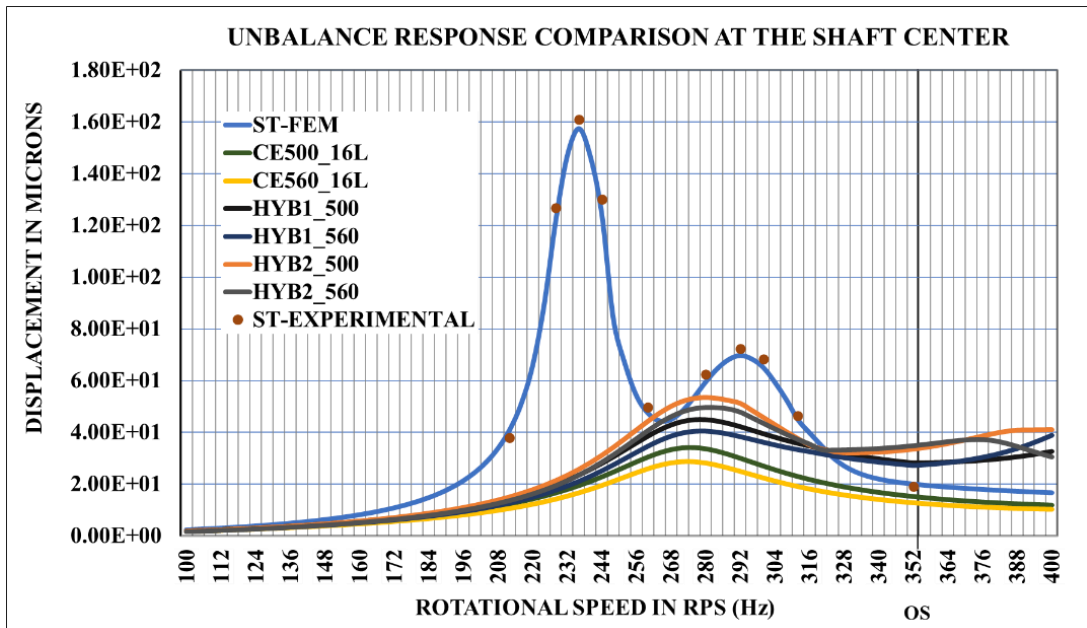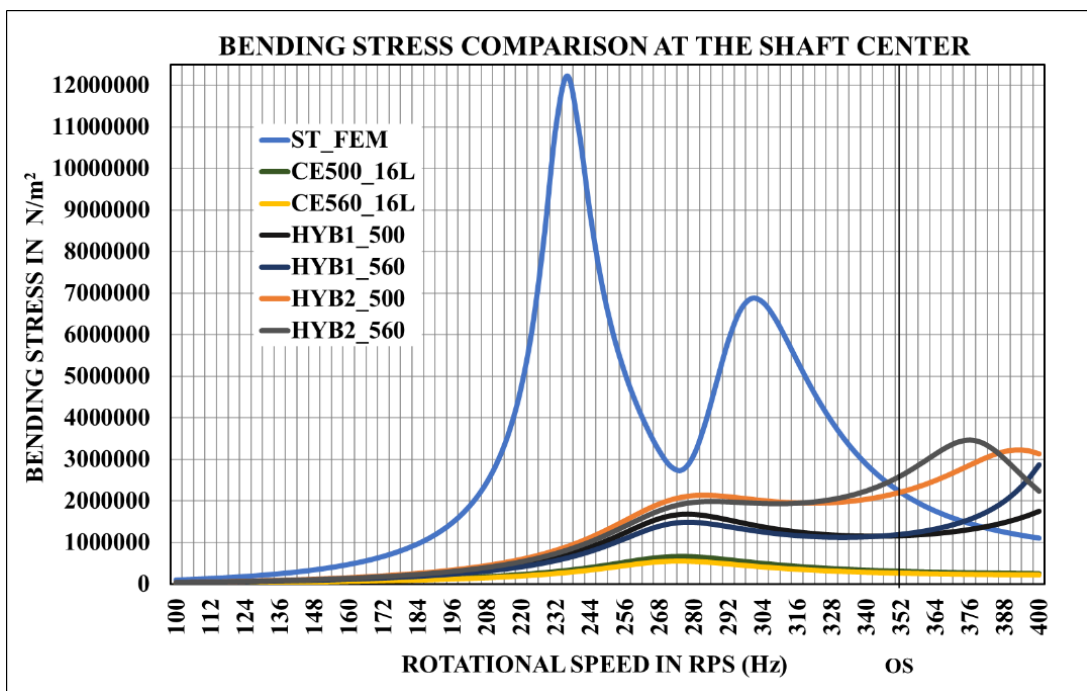| Material	I Critical speed			II critical speed			Operating speed	
	rpm	δ	σ (MPa)	rpm	δ	σ (MPa)	δ	σ (MPa)
ST-FEM	14260	158	12.2	18000	65.1	6.9	20.1	2.2
ST-EXP	14300	161	NM	17800	68.3	NM	19	NM
CE-560	16560	28.6	0.6	>24000	-	-	15.3	0.26
CE-500	16610	34.1	0.55	>24000	-	-	12.8	0.31
HYB1-560	16700	40	1.49	>24000	-	-	28.4	1.16
HYB1-500	16780	45	1.68	>24000	-	-	27.2	1.2
HYB2-560	17280	49.7	1.99	22800	37.3	3.47	34.9	2.2
HYB2-500	17350	53.6	2.14	24000	41.1	3.23	33.6	2.0

6.4 Rotating Internal Damping

The whirl stability analysis was carried out for evaluating the rotor dynamic stability of the rotor-bearing system over the entire operating speed due to the presence of rotating internal damping of the composite material. The material loss factor values obtained by the experimental tests were modeled as an equivalent stiffness proportional damping in the rotor-bearing system. The stability values for only the forward whirl mode are compared as the rotating internal damping has no effect on the backward whirl vibratory motion.

For the mode to be rotor dynamically stable, the logarithmic decrement at all the speeds above and below the critical speed shall be negative. For the unstable modes, the logarithmic decrement (LD) at the critical speed is zero and it changes the sign from negative to positive beyond the critical speed. The stability plots of I mode are shown in Figure 6.9 without the external damping and Figure 6.10 with the external damping. The logarithmic decrement values of all the configurations at the I critical speed are compared in Table 6.5. For all the shaft configurations without the external damping, the I forward whirl mode is unstable and with the external damping included, all the configurations become stable in I mode. Similarly, for the II Mode at the II critical speed, the stability maps shown in Figure 6.11 and Figure 6.12, the logarithmic decrement values are compared in Table 6.6. As evident from the tabulated values the unstable II forward whirl modes of few configurations become stable with the inclusion of external damping
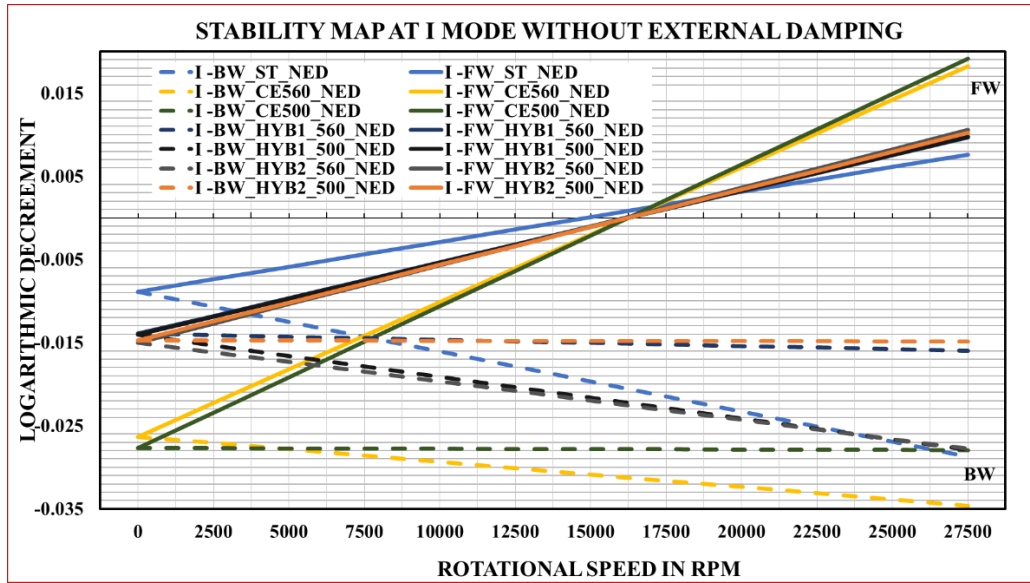
Figure 6.9.   Stability diagram at I lateral mode without external damping
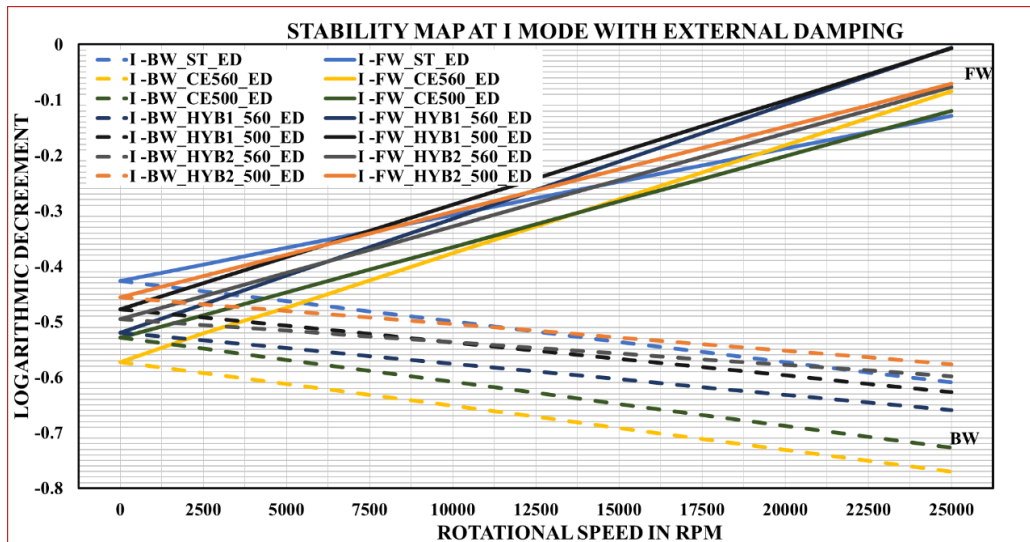
Figure 6.10.   Stability diagram at I lateral mode with external damping

Table 6.5.   Rotor dynamic Stability analysis at I FW mode

Configuration	LF	No External Damping		With External Damping	
		rpm	LD	rpm	LD
ST	0.006	15025	0	14985	-0.248
CE-560	0.03	16156	0	16105	-0.255
CE-500	0.03	16303	0	16280	-0.263
HYB1-560	0.014	16230	0	16220	-0.185
HYB1-500	0.014	16246	0	16230	-0.171
HYB2-560	0.014	16214	0	16205	-0.223
HYB2-500	0.014	16228	0	16218	-0.206

121
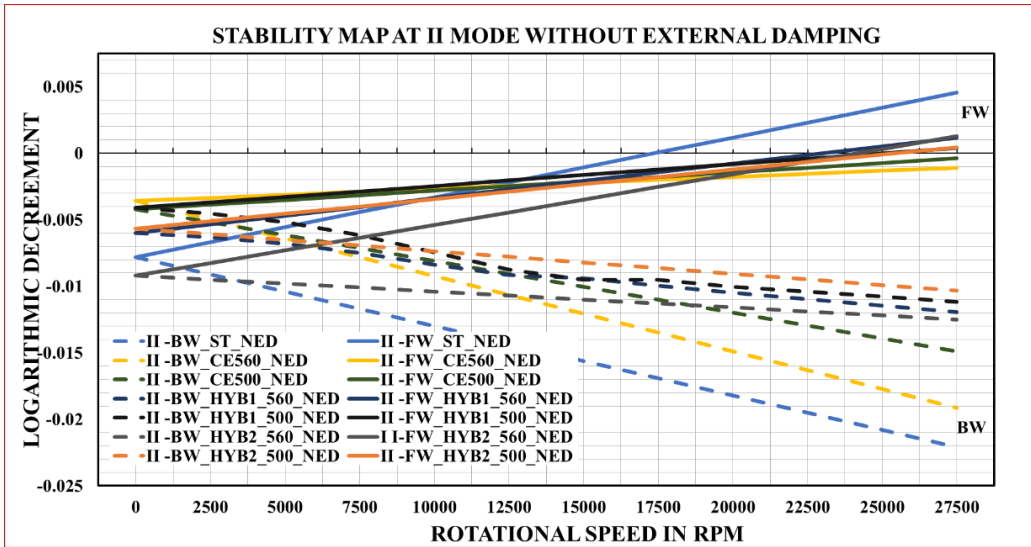
Figure 6.11.   Stability diagram at II lateral modes without external damping
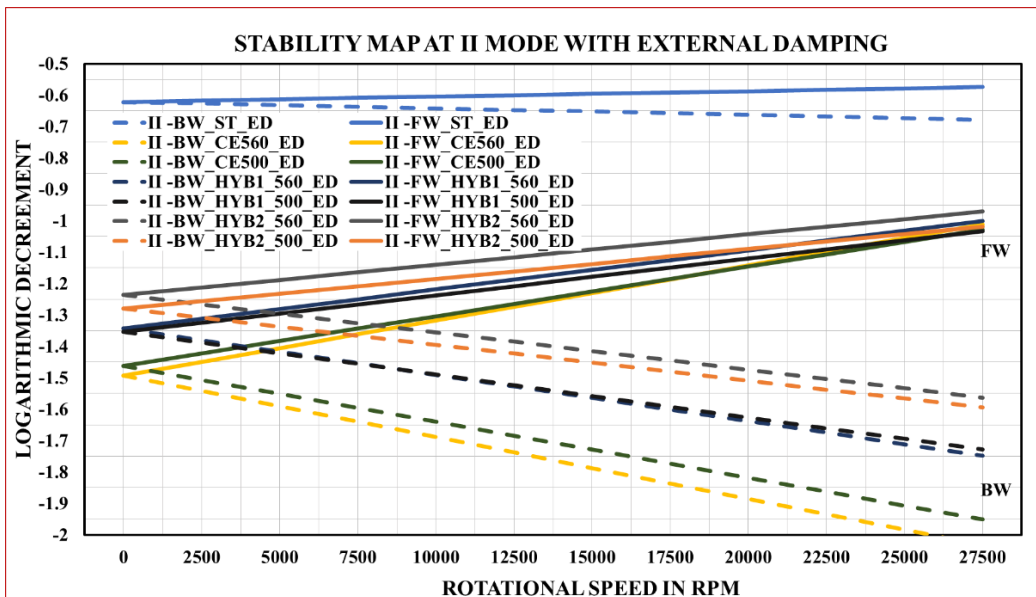
Figure 6.12.   Stability diagram at II lateral modes with external damping

Table 6.6.   Rotor dynamic Stability analysis at II FW mode

Configuration	LF	No External Damping		With External Damping	
		rpm	LD	rpm	LD
ST	0.006	17497	0	17550	-0.595
CE-560	0.03	>27500	-	>27500	-
CE-500	0.03	>27500	-	>27500	-
HYB1-560	0.014	25079	0	26010	-1.2
HYB1-500	0.014	26100	0	26140	-1.1
HYB2-560	0.014	22910	0	23040	-1.1
HYB2-500	0.014	23887	0	23940	-1.1

122

7 CONCLUSIONS

The following conclusions have been made after the thorough evaluation of all the numerical and experimental investigations presented in the previous sections. The future work to be carried to complement this work are also listed.

7.1 Composite/Hybrid Material Shaft Rotor Dynamics

Based on the preliminary and subsequent detailed rotor dynamic and parametric analysis, the composite material shaft becomes an up-and-coming solution for the high-speed power turbine rotor-bearing system.

- The critical speed analysis found that the graphite-epoxy composite material shaft shifts the II forward mode from the existing 17500 rpm to beyond the operating speed range above 23000 rpm, a major advantage from the rotor dynamics point of view. The squeeze film damper provided in the rotor-bearing system is enough to avoid the instability threshold within the operating speed of the composite shaft due to the rotating internal damping.

- The unbalance response analysis carried out clearly illustrates the improvement achieved by the composite shaft in the power turbine rotor-bearing system. The composite shaft reduces the flexural deflection at the canter of the shaft from the existing 157 microns to 22.5 microns. The 700% reduction in the deflection value is substantial as it would effectively eliminate the high-speed balancing being carried out for the existing steel shaft.

- From the rotor dynamic analysis, it was also found that the hybrid tubular composite laminate sandwiched between the steel tubes can be used to leverage the combined strengths of both the materials with the rotor dynamic advantages of the composite shaft intact.

7.2 Experimental Characterization

Based on the experimental characterization tests, the following conclusions are drawn.

- The carbon-epoxy laminate CE1 with the layup orientation of [90, 45, -45, 0_6, 90] and the associated Hybrid1 and Hybrid3 hybrid laminates were found to have the higher tensile and flexural strengths in comparison to CE2, Hybrid2, and Hybrid4 respectively. The same trend was reiterated by the subsequent modal testing and dynamic mechanical analysis as well.

- The dynamic mechanical analysis results of CE1 and Hybrid3 indicated a similar behaviour in terms of the storage and loss modulus in line with the requirement of the intended application. Also, the orthogonal viscoelastic behaviour of Hybrid5 in comparison to the Hybrid3 captured by the dynamic mechanical analysis can be utilized to frame the directional viscoelastic damping characteristics.

- The damping values of both CE1 and Hybrid3 tubular samples estimated by the free vibration tests matched closely with that of the respective beam samples. Hence, based on all the experimental results, Hybrid3 is the best hybrid material for the power turbine shaft.

- To attenuate the excessive vibrations from the rotor-bearing system, the supporting structure shall have an optimum damping and the higher stiffness. Although Hybrid2 exhibits the maximum damping characteristics, Hybrid1 is slightly stiffer than Hybrid2. Hence a suitable hybrid composite material combination for the rotor-bearing supporting structure using the combination of both materials at the appropriate locations can be worked out.

7.3 Remodeled Hybrid Power Turbine Shaft Rotor Dynamics

The following conclusions are made from the rotor dynamic analysis of the remodeled power turbine shaft using the Hybrid3 material.

- The rotor dynamic analysis indicates that, except for the HYB2-560, the other hybrid composite shaft configurations of HYB1-500, HYB1-560, and HYB2-500 eliminate the second critical speed within the operating speed with a comfortable safe margin. Also, as evident from the unbalance response analysis, all the hybrid shaft configurations exhibit the lower bending deformation at the first critical speed compared to the existing steel configuration. The estimated reduction in bending deflection is of the order of 200% to 300%.

- All the configurations of the power turbine shaft analysed with the internal damping estimated from the experiments are found to be rotor dynamically stable for the external damping already available in the existing design. Hence the stability analysis validates the rotor-bearing-support design comprising of the soft bearing support with the existing squeeze film damping from the rotor dynamic stability point of view.

- All the configurations of the hybrid power turbine shaft analysed, a minimum of 45% to the maximum 85% weight saving can be achieved in comparison to the existing steel shaft which is a major advantage in an aero engine application.

- The rotor dynamics of the hybrid shaft design will have a major impact on the total life cycle of several components of the rotating machinery as the reduction in the rotor-bearing system induced vibrations would increase the fatigue life of rotor-bearing-support components. Hence it is concluded that the hybrid composite shaft improves the dynamic behaviour of the high-speed power turbine rotor-bearing system.

7.4 Scope of Future Work:

The present work has successfully illustrated the advantages of hybrid composite shaft in high-speed power turbine rotor-bearing system. However, further in-depth study is required to thoroughly understand the behaviour of hybrid composite material by considering the limitations of composite material such as internal damping, lower interfacial shear strength, propagation of laminate defects etc., The actual application can be possible only if the hybrid composite material overcomes all these limitations using the modern manufacturing methods. Hence, the following future activities are listed to complement the present work.

1. A further improvement in the model updating methodology by adopting a systematic iterative algorithm using the finite element component mode synthesis (CMS) to incorporate the updating of material damping as rotating internal damping in the rotor-bearing system.

2. The experimental investigation of rotor dynamic behaviour of hybrid composite shaft to ascertain the hybrid composite material in the high-speed rotor-bearing system. Static and dynamic experimental investigations by including a known laminate defect to study the propagation of the defect under normal, transient overloading and cyclic loading conditions.

REFERENCES

Adams, D. F. (1998). "Mechanical Test Fixtures." Manual on Experimental Methods for Mechanical Testing of Composites-2nd edition, ed. C.H. Jenkins. *The Fairmount press Inc, Society for Experimental Mechanics*, Chapter 11, 87-100.

Adams, R.D. and Bacon, D.G.C. (1973). "Effect of fiber orientation and laminate geometry on the dynamic properties of CFRP." *Journal of Composite Materials,* 7(1), 402–28.

Adhikari, S. and Phani, A.S. (2009). "Experimental identification of generalized proportional viscous damping matrix." *Journal of Vibration and Acoustics,* 131(1), 011008-1.

Alwan, V., Ankit, G., Sekhar, A.S., and Velmurugan, R. (2010). "Dynamic analysis of shafts of composite materials." *Journal of Reinforced Plastics and Composites,* 29(22), 3364–3379.

Alderliesten, R, C. and Benedictus, R. (2008). "Fiber/Metal Composite Technology for Future Primary Aircraft structures." *Journal of Aircraft,* 45(4), 1182-1189.

Allemang, R.J. and Brown, D.I. (1982). "A correlation coefficient for modal vector analysis." *Ist International Modal Analysis Conference*, Orlando, Florida, 110-116.

ANSYS v12.0. (2010). "Theory Manual." *ANSYS, Inc.,* Southpointe, PA.

Arora, V. (2014). "Structural damping identification method using normal FRFs." *International Journal of Solids and Structures,* 51(1), 133–143.

ASTM D1184-98. (2012). "Standard Test Method for Flexural Strength of Adhesive Bonded Laminated Assemblies." *West Conshohocken, PA: ASTM International*.

ASTM D3039/D3039M – 17. (2017). "Standard Test Method for Tensile Properties of Polymer Matrix Composite Materials." *West Conshohocken, PA: ASTM International*.

ASTM D5448/5448M–16. (2017). "Standard Test Method for In-plane Shear Properties of Hoop Wound Polymer Matrix Composite Cylinders." *West Conshohocken, PA: ASTM International*.

ASTM D756–05. (2017). "Standard Test Method for Measuring Vibration-Damping Properties of Materials." *West Conshohocken, PA: ASTM International*.

ASTM D790 – 17. (2017). "Standard Test Methods for Flexural Properties of Unreinforced and Reinforced Plastics and Electrical Insulating Materials." *West Conshohocken, PA: ASTM International.*

ASTM E8/E8M-16a. (2016). "Standard Test Methods for Tension Testing of Metallic Materials." *West Conshohocken, PA: ASTM International*.

Banks, H.T. and Inman, D.J. (1991). "On damping mechanisms in beams." *Journal of applied mechanic,* 58(3), 716-723.

Bauchau, O.A. (1983). "Optimal design of high speed rotating graphite/epoxy shafts." *Journal of Composite Materials,* 17(3), 170–181.

Benchekchou, B., Coni, M., Howarth, H.V.C. and White, R.G. (1998). "Some aspects of vibration damping improvement in composite materials." *Composites Part B: Engineering,* 29(6), 809–817.

Bert. C.W. (1980). "Composite Materials: A survey of Damping Capacity of Fiber Reinforced Composites." *Damping Applications for Vibration Control,* Ed. P.J. Torvik, ASME, AMD, 38(1), 53-63.

Berthelot, J.M. and Sefrani, Y. (2006). "Damping analysis of unidirectional glass fiber composites with interleaved viscoelastic layers: experimental investigation and discussion." *Journal of Composite Materials,* 40(21), 1911–1932.

Berthelot, J.M., Assarar, M., Sefrani, Y. and Mahi, A.E. (2008). "Damping analysis of composite materials and structures." *Composite Structures,* 85(1), 189–204.

Billups, E.K. and Cavalli, M.N. (2008). "2D damping predictions of fiber composite plates: Layup effects." *Composites Science and Technology,* 68(3/4), 727-733.

Botelho, E.C., Campos, A.N., Barros, E.D., Pardini, L.C. and Rezende, M.C. (2006). "Damping behavior of continuous fiber/metal composite materials by the free vibration method." *Composites Part B: Engineering,* 37(2–3), 255-263.

Boukhalfa, A. and Hadjoui, A. (2010). "Free vibration analysis of an embarked rotating composite shaft using the hp- version of the FEM." Latin American Journal of Solids and Structures, 7(2), 105-141.

Carrera, E., Valvano, S. and Filippi, M. (2018). "Classical, higher-order, zig-zag and variable kinematic shell elements for the analysis of composite multilayered structures." *European Journal of Mechanics/A Solids*, 72(1), 97–110.

Chandra, R., Singh, S.P. and Gupta, K. (1999). "Damping studies in fiber-reinforced composites - a review." *Composite Structures,* 46(1), 41-51.

Chandra, R., Singh, S.P. and Gupta, K. (2003). "A study of damping in fiber-reinforced composites." *Journal of Sound and Vibration,* 262(3), 475–496.

Chang, C.Y., Chang, M.Y. and Huang, J.H. (2004a). "Vibration analysis of rotating composite shafts containing randomly oriented reinforcements." *Composite Structures,* 63(1), 21–32.

Chang, M.Y., Chen, J.K. and Chang, C.Y. (2004b). "A simple spinning laminated composite shaft model." *International Journal of Solids and Structures,* 41(3–4), 637–662.

Chen, W.J. and Gunter, E.J. (2007). "Introduction to Dynamics of Rotor-Bearing Systems." *Eigen Technologies Inc., Trafford Publishing.*

CompositesWorld, (2018). "Hybrid composite struts reducing vehicle weight, improve handling." *Case study post,* 29th Jan 2018.

Craig, R.J. and Bampton, M.C.C. (1968). "Coupling of Substructures for Dynamic Analyses." *AIAA Journal, American Institute of Aeronautics and Astronautics*, 6(7), 1313-1319.

David, I.G. Jones. (2001). "Handbook of Viscoelastic Vibration damping." *John Wiley & Sons Inc.*

de Silva, C. (2005). "Vibration and Shock Handbook." *Boca Raton: CRC Press.*

Devalve, C. and Pitchumani, R. (2013). "Experimental Investigation of the damping enhancement in fiber reinforced composites with carbon nanotubes." *Carbon,* 63(1), 71-83.

Dimentberg, F.M. (1961). "Flexural vibrations of rotating shafts". *Butterworth,* London.

Ege, K., Roozen, N.B., Leclère, Q. and Rinaldi, R.G. (2018). "Assessment of the apparent bending stiffness and damping of multilayer plates; modeling and experiment." *Journal of Sound and Vibration,* 426(1), 129-149.

Ehrich, F.F. (1992). "Handbook of Rotor Dynamics." *Mcgraw-Hill.*

Filippi, M., Carrera, E. and Valvano, S. (2018). "Analysis of multilayered structures embedding viscoelastic layers by higher-order, and zig-zag plate elements." *Composites Part B: Engineering,* 154(1), 77–89.

Filippi, M., Enrico, Z. and Carrera, E. (2019). "A node-dependent kinematic approach for rotordynamics problems." *Journal of Engineering for Gas Turbines and Power*, 141(6), 062501.

Finnegan, I. C. and Gibson, R.F. (1999). "Recent research on enhancement of damping in polymer composites." *Composite Structures,* 44(2-3), 89-98.

Genta, G. and Amati, N. (2010). "Hysteretic damping in rotor dynamics: an equivalent formulation." *Journal of Sound and Vibration,* 329(22), 4772–4884.

Gibson, R.F. (2000). "Modal vibration response measurements for the characterization of composite materials and structures." *Composites Science and Technology,* 60(15), 2769–2780.

Glyn, L., Lin, Y., Yiu-Wing, M. and Chin-The, S. (1997). "The effect of adhesive bonding between aluminum and composite prepreg on the mechanical properties of carbon-fiber-reinforced metal laminates." *Composites Science and Technology,* 57(1), 35-45.

Ghoneam, S. M., Hamada, A. A. and EL-Elamy M. I. (2011). "Dynamic Analysis of a Rotating Composite Shaft." *Aerospace Sciences and Aviation Technology- ASAT – 14*, Article 48, 1-16.

Goodwin, M.J. (1989). "Dynamics of Rotor Bearing system." *Unwin Hyman Ltd,* London.

Gubran, H.B.H., Singh. S.P. and Gupta. K. (2000). "Stresses in composite shafts subjected to unbalance excitation and transmitted torque." *International Journal of rotating machinery,* 6(4), 235-244.

Gubran, H.B.H, and Gupta. K. (2005a). "The effect of stacking sequence and coupling mechanisms on the natural frequencies of composite shafts." *Journal of Sound and Vibration, 282*(1), 231–248.

Gubran, H.B.H. (2005b). "Dynamics of hybrid shafts." *Mechanics Research Communications,* 32(1), 368–374.

Guida, M. Marulo, F. Meo, M. and Russo, S. (2012). "Experimental tests analysis of fiber metal laminate under birdstrike." *Mechanics of Advanced Materials and Structures,* 19(5), 376–395.

Gunter, E.J. Jr. (1966). "Dynamic stability of rotor-bearing systems." *NASA* SP-113.

Gupta, K. (1998). "Some issues relating to design and development of an all-composite aero gas turbine engine Rotors." *Defense Science Journal,* 48(1), 93–98.

Gupta, K. and Singh, S.P. (1998). "Damping measurement in fiber reinforced composite rotors." *Journal of sound and vibrations,* 211(3), 513–520.

Hajianmaleki, M. and Qatu, M.S. (2012). "A rigorous beam model for static and vibration analysis of generally laminated composite thick beams and shafts." *International Journal of Vehicle Noise and Vibration,* 8(2), 166–184.

Henrique, D.R., Goldman, L.M. and Verstrate, P.H. (1987). "Thin walled laminated composite cylindrical Tubes-Part III, critical speed analysis." *ASTM Journal of Composite Technology and Research,* 9(2), 58–62.

Hinton, M.J., Kaddour, A.S. and Soden, P.D. (2004). "Failure Criteria in Fibre Reinforced Polymer Composites: The World-Wide Failure Exercise." *The Netherlands: Elsevier Ltd,* 36-37.

Iqbal, J., Chang, Y. and Qatu, M. (2008). "Optimization of frequencies of a two-span shaft system joined with a hinge." *International Journal of Vehicle Noise and Vibration,* 4(4), 317–338.

Iqbal, J. and Qatu, M.S. (2010). "Transverse vibration of a three-piece shaft system joined with multiple hinges." *International Journal of Vehicle Noise and Vibration,* 6(1), 73–89.

Iriondo, J., Aretxabaleta, L. and Aizpuru, A. (2015). "Characterization of the elastic and damping properties of traditional FML and FML based on a self-reinforced polypropylene." *Composite Structures,* 131(1), 47-54.

Jun, L., Guangwei, R., Jin, P., Xiaobin, L. and Weiguo, W. (2014). "Free vibration analysis of a laminated shallow curved beam based on trigonometric shear deformation theory." *Mechanics Based Design of Structures and Machines: An International Journal*, 42 (1), 111–29.

Kaw, A.K. (2009). "Mechanics of Composite Materials." Second Ed., *Taylor & Francis Group, LLC.*

Kim, C.D. and Bert C.W. (1993). "Critical speed analysis of laminated composite hollow drive shafts." *Composite Engineering,* 3(7–8), 633–643.

Kimball, A.J. (1926). "Internal friction theory of shaft whirling." *General Electric Report,* 27(1), 266.

Koteswara, R. D., Roy, T., Debabrata, G., Prasad, K. and Inamdar. (2013). "Finite Element Analysis of Functionally graded Rotor shaft using Timoshenko Beam." *International Journal of Mechanical and Production Engineering*, 1(2), 10-14.

Koteswara, R. D., Swain, A. and Roy, T. (2020). "Dynamic responses of bidirectional functionally graded rotor shaft." *Mechanics Based Design of Structures and Machines*.

Lalanne, M. and Ferraris, G. (1998). "Rotordynamics Prediction in Engineering." Second Ed., *J. Wiley and Sons.*

Lazan, B.J. (1968). "Material and structural damping for vibration control." *SAE Transactions.* 68(1), 537-547

132

Laszlo, F. (2000). "Instability due to internal damping of symmetrical rotor-bearing systems." *Journal of Computational and Applied Mechanics,* 1(2), 137–147.

Lima, de, A.M.G., Silva, da, A.R., Rade, D.A. and Bouhaddi, V. (2010). "Component mode synthesis combining robust enriched Ritz approach for viscoelastically damped structures." *Engineering Structures,* 32(1), 1479-1488.

Lin, R.M. and Ewins, D.J. (1994). "Analytical model improvement using frequency response functions." *Mechanical Systems and Signal Processing,* 8(4), 437-458.

Maheri, M.R. and Adams, R.D. (1995). "Finite element prediction of modal response of damped layered composite panels." *Composites Science and Technology*, 55(1), 13–23.

Mateen, T., Salman N., Aqueel, S., Sohaib A., Muhammad, A.K. and Sohaib, Z.K. (2018). "Effect of hybrid reinforcement on the performance of filament wound hollow shaft." *Composite Structures*, 184(1), 378–387.

Murugan, R., Ramesh, R. and Padmanabhan, K. (2016). "Investigation on mechanical behaviour and vibration characteristics of thin walled glass/carbon hybrid composite beams under fixed-free boundary condition." *Mechanics of Advanced Materials and Structures*. 23(8), 909–916.

MIL-HDBK-17-2F. (2002). "Department of Defense Handbook: Composite Materials Handbook." *U.S. Army Research Laboratory, Materials Directorate,* Aberdeen Proving Ground, MD. 2(5).

Minas, C. and Inman, D.J. (1991). "Identification of a Nonproportional Damping Matrix from Incomplete Modal Information." *Journal of Vibration and Acoustics,* 113(2), 219-224.

Mohammed, I., Abu Talib, A. R., Hameed Sultan, M. T., Jawaid, M., Ariffin, A. H., and Saadon, S. (2018). "Mechanical properties of fiber-metal laminates made of natural/synthetic fiber composites." *BioRes.* 13(1), 2022-2034.

Montagnier, O. and Hochard, C. (2007). "Dynamic instability of supercritical drive shafts mounted on dissipative supports-effects of viscous and hysteretic internal damping." *Journal of Sound and Vibration,* 305(3), 378–400.

Montagnier, O. and Hochard, C. (2013). "Optimization of hybrid high modulus high strength carbon fiber reinforced plastic composite drive shafts." *Materials and Design,* 46(1), 88-100.

Montagnier, O. and Hochard, C. (2014). "Dynamics of a supercritical composite shaft mounted on viscoelastic supports." *Journal of Sound and Vibration,* 333(2), 470–484.

Mottershead, J.E. and Friswell, M.I. (1993). "Model Updating in Structural Dynamics: A Survey." *Journal of Sound and Vibration,* 167(2), 347-375.

Mutasher, S.A., Sapuan, S.M., Sahari, B.B. and Hamouda, A.M.S. (2005). "Torsion transmission capacity of a hybrid aluminum/composite driveshaft." *Polymers & Polymer Composites*, 14(2), 175-184.

Mutasher, S.A. (2009). "Prediction of torsional strength of hybrid aluminum composite drive shaft." *Material Design,* 30(2), 215-220.

Nejati, M., Asanjarani, A. Dimitri, R. and Tornabene, F. (2017). "Static and free vibration analysis of functionally graded conical shells reinforced by carbon nanotubes." *International Journal of Mechanical Sciences,* 130(1), 383–98.

Newkirk, B.L. (1924). "Shaft whipping." *General Electric Review*, 27(1), 169.

Ni, R.G. and Adams. R.D. (1984). "The damping and dynamic moduli of symmetric laminated composite materials- Theoretical and Experimental Results." *J Compos Mater, 18*(2), 104-121.

Nuno, M. (2009). "Reflections on the hysteretic damping model." *Shock and Vibration,* 16(5), 529–542.

Ozguven, H.N. and Ozkan, Z.L. (1984). "Whirl speeds and unbalance response of multi bearing rotors using finite elements." *ASME Journal of Vibration, Acoustics, Stress and Reliability in Design,* 106(2), 72–76.

Pathan, M.V., Patsias, S., Rongong, J.A. and Tagarielli, V.L. (2017). "Measurements and predictions of the viscoelastic properties of a composite lamina and their sensitivity to temperature and frequency." *Composites Science and Technology,* 149(1), 207-219.

Pradhan, S. and Modak, S.V. (2012). "A method for damping matrix identification using frequency response data." *Mechanical Systems and Signal Processing,* 33(1), 69-82.

Qatu, M.S. and Iqbal, J. (2010). "Transverse vibration of a two-segment cross-ply composite shafts with a lumped mass." *Composite Structures,* 92(1), 1126–1131.

Rao, J.S. (1983). "Rotor dynamics." *John Wiley & Sons.*

Reissner, E. and Tsai, W.T. (1974). "Pure Bending, Stretching, and Twisting of Anisotropic Cylindrical Shells." *Journal of Applied Mechanics,* 39(1), 148-154.

Rayleigh, J.W.S. (1945). "The Theory of sound 1-2." *Dover Publications,* 2nd Edition, New York.

Roger, M.C. and John, W.C.G. Jr. (1991). "Characterization of the vibration damping loss factor of glass and graphite fiber composites." *Composites Science and Technology,* 40(4), 355-375.

Roy, H., Dutt, J.K. and Datta, P.K. (2008). "Dynamics of a viscoelastic rotor shaft using augmenting thermodynamic fields—A finite element approach." *International Journal of Mechanical Sciences*, 50(1), 845–853.

Roy, H., Dutt, J.K. and Datta, P.K. (2009). "Dynamics of multilayered viscoelastic beams." *Structural Engineering and Mechanics*, 33(4), 391-406.

Saravanos, D.A. and Chamis, C.C. (1991). "Computational Simulation of Damping in Composite Structures." *Journal of Reinforced Plastics and Composites*, 10(3), 256-278.

Sarlin, E., Liu, Y., Vippola, M., Zogg, M., Ermanni, P., Vuorinen, J. and Lepistö, T. (2012). "Vibration damping properties of steel/rubber/composite hybrid structures." *Composite Structures,* 94(1), 3327-3335.

Singh, S.P. and Gupta, K. (1993). "Modal testing of tubular composite shafts." *Proceedings of the International Modal Analysis Conference,* Florida, 733–39.

Singh, S.P. and Gupta, K. (1994). "Free damped flexural vibration analysis of composite cylindrical tubes using beam and shell theories." *Journal of Sound and Vibration,* 49(2), 121–132.

Singh, S.P. and Gupta, K. (1996). "Composite shaft rotor dynamic analysis using layerwise theory." *Journal of Sound and Vibration,* 191(5), 739–756.

Sinke, J. (2009). "Manufacturing principles for fiber metal laminates." *Proceeding of seventeenth International Conference on Composite Materials,* 27-31 July 2009, Edinburgh, UK.

Sino, R., Baranger, T.N., Chatelet, E. and Jacquet, G. (2008). "Dynamic analysis of a rotating composite shaft." *Composite Science and Technology,* 68(2), 337–345.

Subhajit, M. and Sushanta, C. (2016). "An inverse approach for the determination of viscous damping model of fiber reinforced plastic beams using finite element model updating." *International Journal of Acoustics and Vibrations,* 21(1), 93-102.

TA Instruments, "DMA Q800 Specifications." *Dynamic Mechanical Analyzer*, www.tainstruments.com.

Talbot, J.P. and Woodhouse, J. (1997). "The vibration damping of laminated plates." *Composites Part A: Applied Science and Manufacturing*, 28(12), 1007-1012.

Tamara, W. K. and Carl, T. H. (1991). "Effect of Fiber Orthotropy on Effective Composite Properties." *Journal of Composite Materials,* 20(6), 732-759.

Tamer, S., Egemen, A., Mustafa, Ö. and Boraa, O.Ç. (2011). "A review: Fibre metal laminates, background, bonding types and applied test methods." *Materials & Design,* 32(7), 3671-3685.

Tornabene, F. (2019). "On the critical speed evaluation of arbitrarily oriented rotating doubly-curved shells made of functionally graded materials." *Thin-Walled Structures,* 140(1), 85–98.

Treviso, A., Van Genechten, B., Mund, D. and Tournour, M. (2015). "Damping in composite materials: Properties and models." *Composites Part B: Engineering,* 78 (1), 144-152.

Tsai, J.L. and Chang, N.R. (2009). "2-D analytical model for characterizing flexural damping responses of composite laminates." *Composite Structures,* 89(3), 443–447.

Udatha, P., Sekhar, A. S. and Velmurugan, R. (2019). "The effect of CNT to enhance the dynamic properties of hybrid composite tube shafts." *Mechanics of Advanced Materials and Structures*, 26(1), 88-92.

Ungar, E.E. and Kerwin, E.M. Jr. (1962). "Loss factor of viscoelastic systems in terms of energy concepts." *Journal of Acoustic Society of America,* 34(1), 954–958.

Vance, J.M. and Lee, J. (1974). "Stability of high-speed rotors with internal friction." *Journal of Engineering for Industry*, TRANS. ASME Series B. Aug.

Vasudevan, A., Senthil Kumaran, S., Naresh, K. and Velmurugan, R. (2018). "Experimental and analytical investigation of thermo-mechanical responses of pure epoxy and carbon/Kevlar/ S-glass/E-glass/epoxy interply hybrid laminated composites for aerospace applications." *International Journal of Polymer Analysis and Characterization*, 23(7), 591–605.

Vance, J.M. (1988). "Rotor Dynamics for Turbomachinery." 1st Edition, *J. Wiley and Sons.*

Vincent, S., Alexander, J., Wilfried, V.L., Luise, K. and Kay, K.W. (2019). "Damping characterization of hybrid carbon fiber elastomer metal laminates using experimental and numerical dynamic mechanical Analysis." *Journal of Composite Science,* 3(1), 3(20).

Wei, C.Y. and Kukureka, S.N. (2000). "Evaluation of damping and elastic properties of composites and composite structures by the resonance technique." *Journal of Materials Science,* 35(15), 3785– 3792.

Wettergren, H.L. (1997). "On the behavior of material damping due to multifrequency excitation." *Journal of Sound and Vibration.* 206(1), 725-735.

Willy, R.D.P.M., Coelho, C.D.M., Artur, L.R.P. and Mauro, H.M. (2017). "The dynamic analysis of rotors mounted on composite shafts with internal damping." *Composite Structures*, 167(1), 50–62.

Yukio, I. and Toshio, Y. (2001). "Linear and Nonlinear Rotor Dynamics." *J. Wiley and Sons*.

Zheng, C., Zhai, Y. and Liang, S. (2020). "Improving damping performance of fiberglass-reinforced resin matrix composites by designing viscoelastic sandwich layer." *Mechanics of Advanced Materials and Structures.*

Zinberg, H. and Symonds, M.F. (1970). "The development of an advanced composite tail rotor drive shaft." *26ᵗʰ Annual National forum of American Helicopter Society*, Washington DC.

Zorzi, E.S. and Giordano, J.C. (1985). "Composite shaft rotor dynamic evaluation." *ASME Design Engg., Conference on Mechanical Vibration and Noise,* 85(114), 1–8.

Zorzi, E.S. and Nelson, H.D. (1977). "Finite element simulation of rotor-bearing systems with internal damping." *ASME Journal of Engineering for Power,* 99(1), 71–76.

LIST OF PUBLICATIONS

Sl. No.	Title of the paper	Authors	Name of the Journal/Conference	Publication Month, Year
1.	Parametric Study of Laminated Composite Material Shaft of High-Speed Rotor-Bearing System.	Thimothy Harold Gonsalves, G.C. Mohan Kumar and M.R. Ramesh	International Conference on Design, Materials and Manufacturing (1st ICDEM), NITK, India. AIP Conference Proceedings (Scopus) https://doi.org/10.1063/1.5029593	Jan 2018
2.	Leveraging Effectiveness of Hybrid Metal-Fiber laminated composite material in High-Speed Rotating machines.	Thimothy Harold Gonsalves, G.C. Mohan Kumar and M.R. Ramesh	International Conference on Polymer Composites (2nd ICPC), NITK, India. AIP Conference Proceedings (Scopus) https://doi.org/10.1063/1.5085580	Dec 2018
3	Dynamic Study of Composite Material Shaft in High-Speed Rotor-Bearing Systems.	Thimothy Harold Gonsalves, G.C. Mohan Kumar and M.R. Ramesh	International Journal of Vehicle Noise and Vibration (IJVNV) Inderscience Publications, Scopus Indexed https://doi.org/10.1504/IJVNV.2019.106371	July 2019

Sl. No.	Title of the paper	Authors	Name of the Journal/Conference	Publication Month, Year
4	Model Updating of Material Damping in Composite Material of Rotor-Bearing Support System.	Thimothy Harold Gonsalves, G.C. Mohan Kumar and M.R. Ramesh	International Conference on Design, Materials and Manufacturing (2nd ICDEM), NITK, India. AIP Conference Proceedings (Scopus) https://doi.org/10.1063/5.0003873	July 2020
5	Hybrid Composite Shaft of High-Speed Rotor-Bearing System - A Rotor Dynamics Preview	Thimothy Harold Gonsalves, G.C. Mohan Kumar and M.R. Ramesh	Mechanics Based Design of Structures and Machines (MBDSM), An International Journal (Taylor and Francis, Scopus/SCIE), https://doi.org/10.1080/15397734.2020.184100	Nov 2020
6	Dynamic Characterization of Hybrid Composite Material used in Rotor-Bearing Support System	Thimothy Harold Gonsalves, G.C. Mohan Kumar, M.R. Ramesh and Sharnappa Joladarashi	Mechanics of Advanced Materials and Structures (MAMS) - Journal (Taylor & Francis, Scopus/SCIE) https://doi.org/10.1080/15376494.2020.186166	Dec 2020

BIO-DATA

Name	:	Thimothy Harold Gonsalves
Father's Name	:	Late Gregory Gonsalves
Mother's Name	:	Magdalene Gonsalves
Date of Birth	:	06th April 1974
Email Id	:	thgon@yahoo.com
Telephone (Office)	:	080-22326656
Telephone (Residence)	:	080-41626418
Mobile	:	9036011056/9845018488

Educational Qualifications:

Sl. No.	Degree	Institution	Year of Passing	Class
1	Ph.D. (Mechanical Engineering)	NITK, Surathkal	December 2020	-
2	M.E. (Machine Design)	UVCE, Bengaluru,	March 2000	Distinction 80.95%
3	B.E. (Mechanical Engineering)	MCE, Hassan	November 1995	Distinction 72.2%

Professional Experience:

Sl. No.	Organization (M/s)	Designation	From	To
1	HAL, Bengaluru	Senior Manager (Design)	13.12.2001	Till date
2	Kennametal, Bengaluru	Assistant Engineer (Design)	04.10.2000	08.12.2001
3	VIT, Bengaluru	Lecturer Engineering	06.10.1999	03.10.2000
4	Disa (India) ltd., Tumkur	Graduate Engineer	15.04.1996	28.02.1998